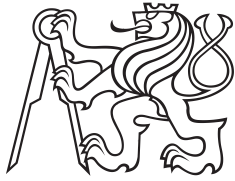


Dissertation Thesis



**Czech
Technical
University
in Prague**

F4

**Faculty of Nuclear Sciences and Physical Engineering
Department of Physics**

Study of turbulence on the COMPASS tokamak using different diagnostic systems

Ing. Jaroslav Krbec

Supervisor: Ing. Martin Hron, Ph.D.

Consultant: Dr. Miklós Berta

Field of study: Nuclear Engineering

Subfield: Physics and Technology of Thermonuclear Fusion

March 2020

Acknowledgements

I would like to thank my supervisor Ing. Martin Hron, Ph.D. and to the director of the Institute of the Plasma Physics of the Czech Academy of Sciences doc. RNDr. Radomír Pánek, Ph.D. for giving me the opportunity to deal with plasma fluctuations and turbulence. Many thanks belongs to Dr. Miklós Berta for his invaluable help during my work and studies.

I would like to offer my special thanks to Mgr. Jakub Seidl, Ph.D., who always helped me with the problems I came across, for his drive in turbulence research on the COMPASS tokamak.

Last but not least, I would like to say a special thank to my family and wife Kristýna for supporting me in everything I do.

Declaration

I hereby declare that I have written this thesis independently and I have cited all sources I have used in the bibliography.

Prague, March 3, 2020

Prohlašuji, že jsem předloženou práci vypracoval samostatně, a že jsem uvedl veškerou použitou literaturu.

V Praze, 3. března 2020

Jaroslav Krbec

Abstract

This thesis reports the results on the Geodesic Acoustic Mode (GAM) measurement using data from a broad set of diagnostics available on the COMPASS tokamak, e.g. reciprocating probes, magnetic coils, Thomson scattering diagnostics, Neutral Particle Analyzer (NPA). All measured data was merged into the database on which numerical simulations, regression analysis and statistical methods were applied. The output from analysis was the agreement of measured and theoretically predicted GAM frequency scaling with plasma temperature and also evaluation of damping rate and NBI heating on GAM amplitude. This thesis also reports capabilities of Lithium Beam Emission Spectroscopy (Li-BES) diagnostics relating to plasma density fluctuation measurement.

Keywords: COMPASS, tokamak, plasma, fluctuation, turbulence, GAM

Supervisor: Ing. Martin Hron, Ph.D.
Ústav fyziky plazmatu AV ČR, v. v. i.,
Za Slovankou 1782/3,
182 00 Praha 8

Abstrakt

Předkládaná práce popisuje výsledky měření Geodetických akustických módů (GAM) na tokamaku COMPASS za použití celé řady dostupných diagnostických nástrojů, např. reciprokových sond, magnetických cívek, diagnostiky Thomsonova rozptylu, analyzátoru neutrálních částic (NPA) a dalších. Všechna naměřená data byla sloučena do databáze, na které byly použity numerické simulace, regresní analýza a statistické metody. Výsledkem bylo získání shody mezi teorií a experimentem při měření škálování frekvence GAMů s teplotou plazmatu a dále vyhodnocení vlivu útlumu a ohřevu NBI na amplitudu GAMů. Tato práce rovněž zahrnuje výsledky analýzy emisní spektroskopie na lithiovém svazku z pohledu měření fluktuací hustoty.

Klíčová slova: COMPASS, tokamak, plazma, fluktuace, turbulence, GAM

Překlad názvu: Studium turbulence na tokamaku Compass za použití různých diagnostických systémů

Contents

1 Introduction	1	5.3 Measurement of ELMs	46
		5.4 Summary	47
Part I		6 Geodesic Acoustic Modes	49
Theoretical background		6.1 GAM frequency scaling	49
2 Plasma confinement	7	6.2 GAM damping	51
2.1 Tokamak device	7	6.3 GAM amplitude scaling	51
2.2 Particle and heat transport	8	6.4 Summary	53
2.3 Plasma instabilities	9	7 Conclusions and outlook	55
2.3.1 Macro-instabilities	10		
2.3.2 Micro-instabilities	10	Appendices	
2.4 SOL turbulence	11	A Selected author's publications	59
2.5 Shear flows	15	A.1 Fast density reconstruction of	
2.5.1 Zonal flows	15	Li-BES signal on the COMPASS	
2.5.2 Geodesic Acoustic Modes	16	tokamak	60
2.6 Confinement modes	19	A.2	68
2.6.1 Edge Localized Modes	19	A.3	84
2.6.2 I-mode and advanced modes	20	B Bibliography	91
2.7 Density fluctuations	20	C List of author's publications	103
		C.1 Publications related to the thesis	103
Part II		C.2 Other publications	104
Experimental setup and methodology		C.3 Conference proceedings	105
3 COMPASS tokamak and used	25	C.4 Conference posters	107
diagnostics			
3.1 Tokamak COMPASS	26		
3.2 Diagnostics	26		
3.2.1 Lithium Beam Emission			
Spectroscopy	26		
3.2.2 Magnetics	32		
3.2.3 Reciprocating probes	33		
3.2.4 Spectrometry and optical			
diagnostics	34		
3.2.5 Other diagnostics	35		
3.3 Diagnostics summary	36		
4 Statistical tools and data	37		
preprocessing			
4.1 Preprocessing	37		
4.2 Signal analysis	39		
4.3 Statistical tools	41		
4.4 Optimization	42		
Part III			
Results			
5 Plasma fluctuations	45		
5.1 Reconstruction algorithm	45		
5.2 Comparison with other			
diagnostics	45		

Figures

<p>1.1 The Starry Night painting. 1</p> <p>2.1 Schematic representation of the tokamak. 8</p> <p>2.2 Gyro-kinetic simulation. 11</p> <p>2.3 Physical mechanism of drift waves. 12</p> <p>2.4 Simulated and measured blob structures. 12</p> <p>2.5 Kolmogorov (3D) and Kraichnan (2D) energy spectrum. 13</p> <p>2.6 Scrape-off layer stability diagram. 15</p> <p>2.7 Poloidal structure of GAM components. 17</p> <p>2.8 Collisional and collisionless damping of GAM. 18</p> <p>2.9 Peeling-Ballooning mode stability diagram. 19</p> <p>3.1 COMPASS tokamak. 25</p> <p>3.2 COMPASS tokamak diagnostic systems. 27</p> <p>3.3 Li-beam experimental setup. 28</p> <p>3.4 Penetration depth of Li-beam. 28</p> <p>3.5 Reconstructed density profile for different beam diameters. 29</p> <p>3.6 Noise to signal ratio of Li-beam signal. 30</p> <p>3.7 Effect of density perturbation on Li-BES light profile. 30</p> <p>3.8 Simulation of density fluctuations propagation to light fluctuations. 31</p> <p>3.9 Density reconstruction removes anti-correlation in the signals. 32</p> <p>3.10 Location of magnetic diagnostics on the COMPASS tokamak. 33</p> <p>3.11 Probe head position and various shapes and probe placement on the head. 34</p> <p>3.12 Line of sight (LOS) for different optical diagnostics. 35</p> <p>4.1 Types of spectral filters. 38</p> <p>4.2 Spectrogram and spectrum of a signal. 40</p> <p>4.3 Envelope of up-chirp signal estimated using Hilbert transform. 41</p>	<p>5.1 Comparison of electron density profiles from Li-BES and Thomson scattering diagnostics. 46</p> <p>5.2 Density profile from Li-BES, Reflectometry and Thomson scattering diagnostics. 46</p> <p>5.3 Temporal evolution of averaged ELM. 47</p> <p>5.4 Temporal evolution of density at the top of the pedestal. 47</p> <p>5.5 ELM precursor oscillation. 48</p> <p>6.1 Slice in the GAM database. 50</p> <p>6.2 Radial profile of GAM damping rate. 52</p> <p>6.3 Impact of NBI on GAM amplitude. 52</p>
---	--

Tables

3.1 Main parameters of the COMPASS tokamak.	26
3.2 Basic parameters of diagnostics on the COMPASS tokamak with measured quantities used in presented work.....	36
6.1 Plasma parameters stored in GAMDB.	51

Abbreviations

APD	Avalanche photodiode	PPD	Photoconductive photodiode
BPP	Ball-pen probe	PSD	Power spectral density
CCD	Charge-coupled device	RMP	Resonant magnetic perturbation
CDB	COMPASS database	SND	Single-null-divertor
CDF	Cumulative distribution function	SNR	Signal to noise ratio
CPSD	Cross power spectral density	SOL	Scrape-off-layer
CR	Collisional-radiative	SXR	Soft X-Ray
CTEM	Collisionless trapped electron mode	TLS	Total least squares
DFT	Discrete Fourier transform	TIM	Trapped ion modes
DT	Deuterium-Tritium	TF	Toroidal field
EDW	Electron drift waves	TS	Thomson scattering
EFIT	Equilibrium Fitting	VRCP	Vertical reciprocating probe
ELM	Edge localized mode	WCM	Weakly coherent mode
ESEL	Electrostatic edge-SOL	WTLS	Weighted total least squares
ETB	Edge transport barrier		
ETG	Electron temperature gradient		
FFT	Fast Fourier transform		
GAM	Geodesic acoustic mode		
GAMDB	GAM database		
HFS	High field side		
HRCP	Horizontal reciprocating probe		
HV	High voltage		
IDL	Interactive data language		
ITB	Internal transport barrier		
ITER	International Thermonuclear Experimental Reactor		
ITG	Ion temperature gradient		
LCFS	Last closed flux surface		
LFS	Low field side		
Li-BES	Lithium beam emission spectroscopy		
LP	Langmuir probe		
MHD	Magnetohydrodynamics		
MST	Medium Size Tokamak		
NBI	Neutral beam injection		
NSR	Noise to signal ratio		
NSTX	National Spherical Torus Experiment		
NPA	Neutral particle analyzer		
PDF	Probability density function		
PF	Poloidal field		
PMT	Photomultiplier tube		

Nomenclature

Letters representing vectors are printed in bold italic type, e.g. \mathbf{B} for magnetic field vector. Letters without sub- or superscript in the list may appear in the text with them. In that case, letters denotes the same physical quantity but their meaning is more specified by sub- or superscript, e.g. B_ϕ for toroidal magnetic field. Attached publications do not follow this nomenclature.

Roman letters

a	Minor radius
B	Magnetic field
c_s	Sound speed
C_{coil}	Coil capacitance
C_{xy}	Coherence
D	Particle diffusion coefficient
D_b	Penetration length
E	Electric field
\mathcal{E}	Energy
$f(x, v)$	Distribution function
$F(x)$	Discrete Fourier transform
$H(z)$	Transfer function
$\mathcal{H}(x)$	Hilbert transformation
i	Imaginary unit
j	Index
J	Current
k	Wavenumber
l, L	Characteristic length
L_{coil}	Coil inductance
Li	Light signal
m	Poloidal mode number
m	Mass
M	Number of samples
n	Toroidal mode number
n	Plasma density
N	Number of samples
p	Pressure
$p(x)$	Probability density function
P_L	Power losses
P_{xx}	Power spectral density
P_{xy}	Cross power spectral density
q	Safety factor
Q	Fusion energy gain factor
r	Radial distance from R_0

r_L	Larmor radius
r_{xx}	Auto-correlation
r_{xy}	Cross-correlation
R	Radial coordinate
R_0	Major radius
R_{coil}	Coil resistance
s	Index
S	Surface
t	Time
T	Temperature
T_{eddy}	Eddy turnover time
u, v	Velocity
x, y	General functions
X, Y	Z-transformed functions
X_f, Y_f	Fourier transformed functions
U, V	Voltage or potential
W	Plasma energy
Z	Vertical coordinate
$Z(\zeta)$	Plasma dispersion function

Greek letters

γ	Growth or damping rate
γ_i	Ion specific heat ratio
δ	Perturbation
Δ	Shafranov shift
Δ'	Shafranov shift gradient
ϵ	Energy dissipation rate
ϵ_0	Inverse aspect ratio
η	Kinematic viscosity
θ	Poloidal coordinate
κ	Plasma elongation
λ	Characteristic step length
μ	Mean value
μ_n	n-th moment of PDF
ν	Collisional rate
ρ	Density
τ	Electron/Ion temperature ratio
τ_E	Energy confinement time
ϕ	Toroidal coordinate
χ	Heat diffusion coefficient
ω	Frequency
ω_{corr}	Decorrelation rate
ω_{shear}	Shearing rate

Chapter 1

Introduction

Turbulence in general is a challenge in many branches of mankind activities, e.g. fluid research, aerospace, mathematics (Navier-Stokes equation solution is one of the Clay's institute Millennium problems [Clay Mathematics Institute, 2000]). It is also very popular topic in between artists (Fig. 1.1) and public especially if appears with term "chaos".



Figure 1.1: The Starry Night painting by Vincent van Gogh: luminance statistic follows the Kolmogorov theory [Aragón et al., 2008].

In plasma physics, the turbulence strongly influences the transport across the magnetic field and produces so called "anomalous" diffusion (see section 2.2). Therefore, a research of plasma turbulence can effect the size of future fusion power plant through the energy confinement time (see section 2.1).

Plasma turbulence can be studied from several aspects, e.g. energy cascades [Kolmogorov, 1941], drift waves [Horton, 1999], quasi-particle models [Diamond et al., 2010], stochastic model of fluctuations [Garcia, 2012]. This thesis focuses on detection of Zonal flows, namely Geodesic Acoustic Modes (GAM), using various diagnostic systems and density fluctuation measurement using Lithium Beam Emission Spectroscopy (Li-BES).

in Appendix A.2). Author's contributions to this article are as follows: analysis of GAM frequency scaling with temperature (Fig. 6 in the article); analysis of GAM amplitude scaling with plasma elongation and safety factor (Fig. 5 in the article); and calculation of collisional and Landau damping of GAM at the edge (Fig. 2 in the article). The author also processed data for foreign colleagues and contributed to [3] with Figures 2. and 3 in the article to support their theoretical model with experimental data (article also attached in Appendix A.3).

- **Chapter 7** concludes the thesis and presents future plans.



Part I

Theoretical background

Chapter 2

Plasma confinement

Abundance of matter in plasma state is very low on the Earth. The reason for this is the fact that plasma natural temperature is much higher than the average temperature on the Earth. Several types of machines, which serve as Dewar bottles for the plasma, were developed since the 50s of the 19th century. Development of such a device is driven by desire to handle fusion reaction and provide "clean" and almost unlimited source of energy for the mankind. General requirement for all these devices to maintain self-sustained deuterium-tritium (DT) plasma is Lawson criterion [Lawson, 1957]

$$n\tau_E \gtrsim 1.5 \cdot 10^{20} \text{ m}^{-3}\text{s}, (\text{for DT}) \quad (2.1)$$

where n is the plasma density and τ_E is the energy confinement time. Energy confinement time is a characteristic time scale at which the plasma energy W decreases if cooled down by power losses P_L , i.e. $\tau_E = W/P_L$ [Wesson and Campbell, 2011]. The value on the right-hand side changes with the type of fusion reaction (minimal value is for DT reaction) and is a function of plasma temperature [Wesson and Campbell, 2011]. Tokamak is the most promising device over the decades for fulfilling eq. (2.1). The most successful experiment so far has been Joint European Torus (JET) which produced 16 MW of peak fusion power [Gibson and team, 1998] with 23 MW of deposited power into plasma giving fusion energy gain factor $Q \approx 0.7$. The aim of the next step devices such as ITER is to reach the higher values of Q , i.e. 'break-even' ($Q = 1$), and also the possibility of controlled 'ignition' ($Q > 1$) should not be precluded [Green et al., 2003].

2.1 Tokamak device

Tokamaks have strong toroidal magnetic field \mathbf{B}_ϕ produced by external coils complemented with weaker poloidal magnetic field \mathbf{B}_θ generated by plasma current. Indexes denote direction in the toroidal coordinate system as can be seen in Fig. (1). This helical structure of magnetic field confines charged particles in the tokamak vessel. Each virtual particle follows the magnetic field line in a region of closed flux surfaces, i.e. inside the separatrix and starting from a point in a given poloidal plane travels in poloidal and

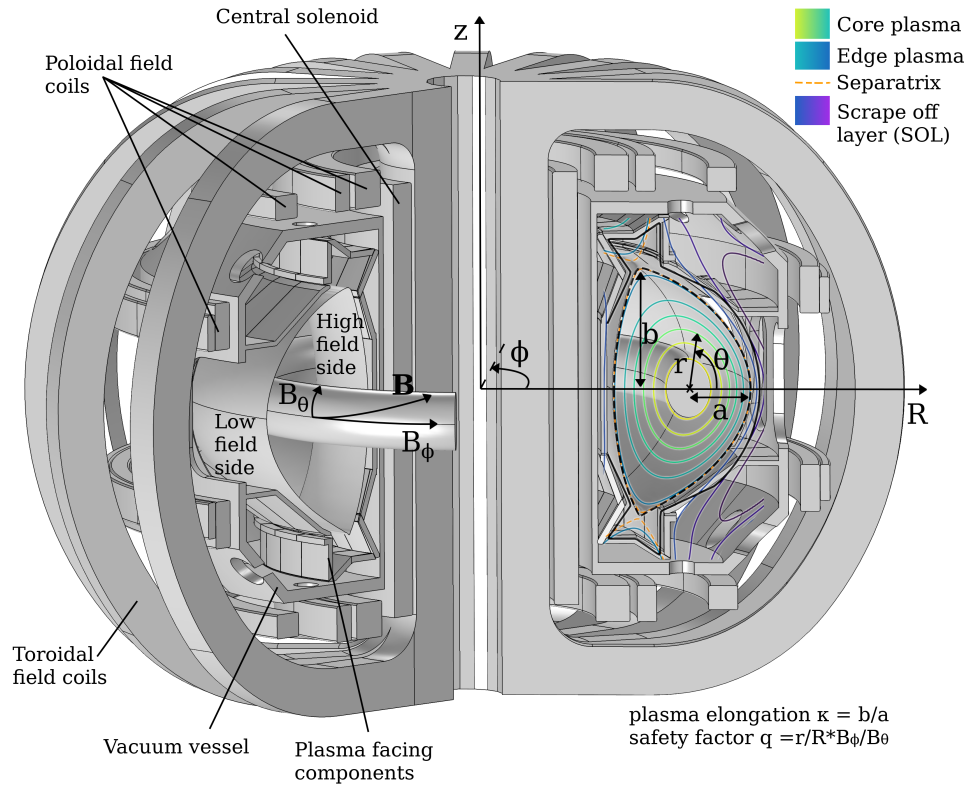


Figure 2.1: Schematic representation of the tokamak.

n toroidal cycles before it enters the same point, and therefore m and n are called poloidal and toroidal mode numbers, respectively.

Cross-field heat transport driven by binary collisions between particles has major influence on energy confinement time, which can be expressed as [Wesson and Campbell, 2011]

$$\tau_E = \frac{a^2}{\chi}, \quad (2.2)$$

where a is the minor radius of the tokamak and χ is the heat diffusion coefficient. The indicator τ_E represents how well is the plasma insulated from the surroundings, thus the higher τ_E means more effective fusion reactor and lower cost of produced fusion energy. From equation (2.2) follows that τ_E can be increased by increasing the size of the machine or by lowering the diffusion coefficient. The former leads to building large devices, the latter requires better understanding of the cross-field particle and heat transport.

2.2 Particle and heat transport

During the history of fusion research, several theories were developed with the aim to quantify the particle and the heat transport across the magnetic

field and estimate the diffusion coefficient for particle (D) and heat (χ) transport

$$D, \chi \propto \frac{\lambda^2}{\tau}, \quad (2.3)$$

where τ is the characteristic time between collisions and λ is characteristic step length. Exact definition of the variables on the right-hand side of eq. (2.3) depends on the chosen transport theory.

Classical theory of transport based on the idea of random walk model with λ as Larmor radius r_L was very optimistic and was responsible for the failure of the first designs on tokamak working as fusion reactor [Sakharov and Tamm, 1958].

Considering the toroidal geometry of magnetic fields of advanced fusion devices the theory of neoclassical transport has been worked out [Galeev and Sagdeev, 1968]. It takes into account contribution of particles trapped on banana trajectories to transport, but still the experimentally measured transport coefficient was an order of magnitude higher than the theoretical value ($\chi^{\text{exp}} \gg \chi^{\text{theory}}$) [Hawryluk et al., 1998]. The reason for that are micro-instabilities in plasma which drive turbulent transport of particles denoted as "anomalous" transport. "Anomalous" transport is non-local, thus neither diffusive nor convective [Garcia et al., 2007b]. Neoclassical transport is the upper theoretical limit for confinement in toroidal devices.

2.3 Plasma instabilities

Instabilities in general are driven by free energy stored in fluid density or temperature gradients $\nabla n, \nabla T$ (macro-instabilities) or by kinetic gradients $\nabla f(x, v)$ (micro-instabilities). Inherent feature of toroidal magnetic field \mathbf{B}_ϕ is its non-uniformity along R axis which produces $\mathbf{B}_\phi \times \nabla B_\phi$ drift [Freidberg, 1987]. Consequent charge separation initiates $\mathbf{E} \times \mathbf{B}$ drift towards the plasma on the high-field side (HFS) and towards the tokamak wall on the low-field side, and therefore causes loss of particles on the LFS of the tokamak (Fig. 2.1). Fortunately, twisted geometry of \mathbf{B} connects LFS and HFS and allows compensation of the drift. LFS is also called bad curvature side since interchange instability can evolve and many other ballooning type modes can grow in this area [Miyamoto, 1997]. Therefore, helical magnetic field stabilizes plasma via particle interaction and sound waves unless instability growth rate γ in the bad curvature region is greater than the propagation rate from the bad curvature to the good curvature regions and via sound waves.

A LFS predisposition for growth of instabilities makes it an ideal area for instability measurement. Moreover, accessibility to the LFS by diagnostics is considerably better than to the HFS, where central solenoid is located and TF coils are close to each other. Part III of this theses present results related to both types of instabilities with respect to the drive mechanism. Following

sections will mention only few representatives of the instabilities related to the results in part III.

■ 2.3.1 Macro-instabilities

Representative of fluid gradient driven instability is the peeling-ballooning instability which is a candidate for mechanism of Edge Localized Modes (ELM) [Connor et al., 1998] (more in section 2.6.1). Macro-instabilities are derived from magnetohydrodynamic (MHD) energy principle. A stable energetic condition requires that a change of a plasma potential energy W is positive when perturbation is applied

$$\delta W > 0. \quad (2.4)$$

Therefore, the force acting on the perturbation is positive and prevents plasma to displace.

Investigation of stability of toroidal MHD equilibrium with free boundary, i.e. the plasma boundary can move, gives more restricted condition on stability than Mercier's criterion [Lortz, 1975, Mercier, 1962]. If this peeling stability criterion is not fulfilled the current-driven peeling mode develops. Mode is destabilized by parallel edge current thus, the higher bootstrap current [Galeev and Sagdeev, 1971, Bickerton et al., 1971] leads to occurrence of this mode. Whereas the Pfirsch-Schlütter current [Pfirsch and Schlüter, 1962] has stabilizing effect because of its anti-parallel component on the HFS. Modification of peeling stability criterion with pressure driven ballooning mode leads to combined peeling-ballooning instability [Connor et al., 1998].

■ 2.3.2 Micro-instabilities

Micro-instabilities have characteristic length scale across the magnetic field comparable to the ion Larmor radius r_{Lion} . Each of the instability is an individual result of solution of non-linear electromagnetic toroidal gyrokinetic equation [Frieman and Chen, 1982]. There is a wide variety of instabilities derived from this equation [Cap, 2013], however, the diffusion coefficients for anomalous transport are obtained from gyro-kinetic simulations (see Fig. 2.2) rather than analytic calculations [Pueschel et al., 2012].

Representative of kinetic driven instability is a group of micro-instabilities responsible for plasma anomalous transport [Horton, 1999]. The most promising candidates for generation of the anomalous transport from this group are the following mechanisms: Ion Temperature Gradient (ITG) [Rudakov and Sagdeev, 1961, Cowley et al., 1991], Electron Temperature Gradient (ETG) [Jenko et al., 2000], Trapped Ion Modes (TIM) [Dominguez, 1991], Collisionless Trapped Electron Modes (CTEM) [Horton, 1999] and Electron Drift Waves (EDW) [Wesson and Campbell, 2011]

EDW are a basic mechanism of generation of radial transport in inhomogeneous plasma. Consider a slab geometry with density gradient ∇n and magnetic field B as on Fig. 2.3. A small density perturbation δn will

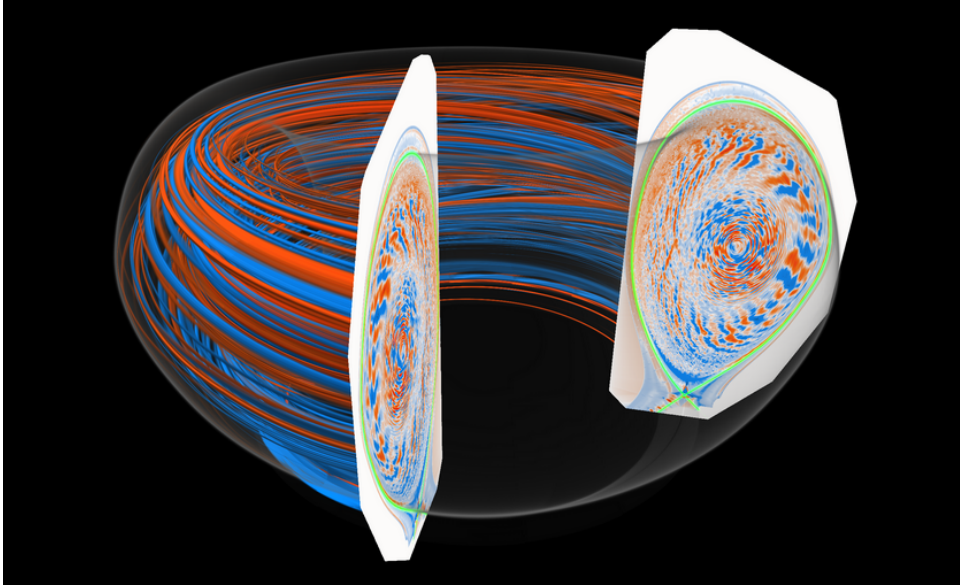


Figure 2.2: 3D visualization of gyro-kinetic simulation result from XGC1 code [Chang et al., 2009, Ku et al., 2009]. Red-blue scale represents plasma density fluctuations caused by turbulence driven by ion temperature gradient. The green line shows LCFS. Image: C.S. Chang, Princeton Plasma Physics Laboratory [Lawrence Berkeley National Laboratory, 2017]

be compensated along the field line by Boltzmann response of electrons which creates 90 degree phase shifted $E \times B$ force. There is no net radial transport if the electrons are not slowed down by dissipation processes thus the wave propagates perpendicularly to ∇n and B with diamagnetic drift velocity (this is the origin of the word "drift" in its name). Although the magnetic shear can stabilize the instability, EDW is called "Universal instability" [Galeev et al., 1963] because a finite electron mass and energy dissipation will result in radial transport in almost every tokamak plasma.

2.4 SOL turbulence

Turbulence is a feature of a fluid flow. Turbulent denotes unpredictable (chaotic) but deterministic behavior of the system.

Example of such a system in tokamak plasmas is motion of plasma particles in the Scrape-off-layer (SOL), that is region in between the Last Close Flux Surface (LCFS) and limiter (see Fig. 2.1). Plasma physicist observed intermittent events of large transport of energy and particles in this area [Zweben and Gould, 1985, Endler et al., 1995]. As the diagnostic techniques developed, these burst of particles got different names such as filaments (1D parallel structure)[Katz et al., 2008], streamers, avalanches (1D radial structures)[Manfredi et al., 2001, Carreras et al., 1998]. When finally observed this area with high speed cameras the eddy (2D vortex) structure was seen (see Fig. 2.4) [Zweben et al., 2003]. A 2D simulations also

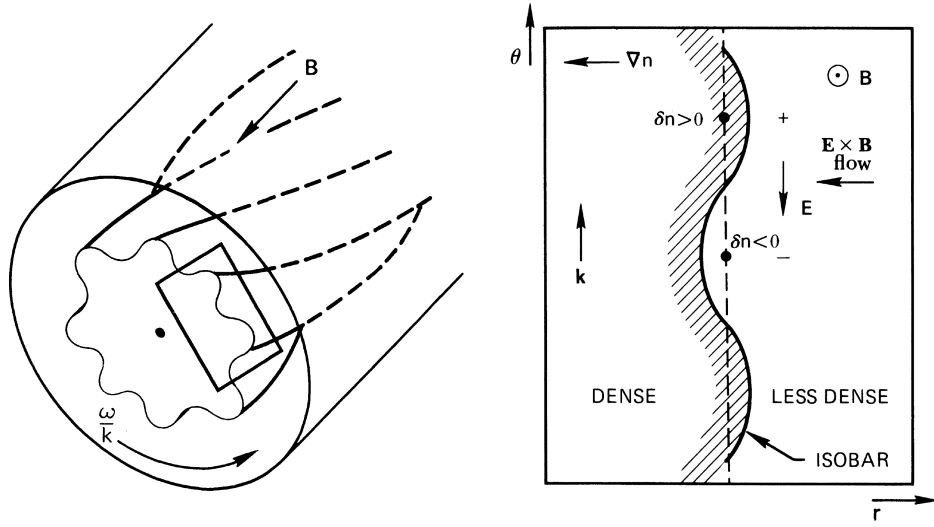


Figure 2.3: The region in the rectangle of cylindrical geometry is representing slab geometry for description of physical mechanism of drift waves. Taken from [Chen, 1984].

predicted generation of structure called "blob" which is shown in Fig. 2.4 [Garcia et al., 2005].

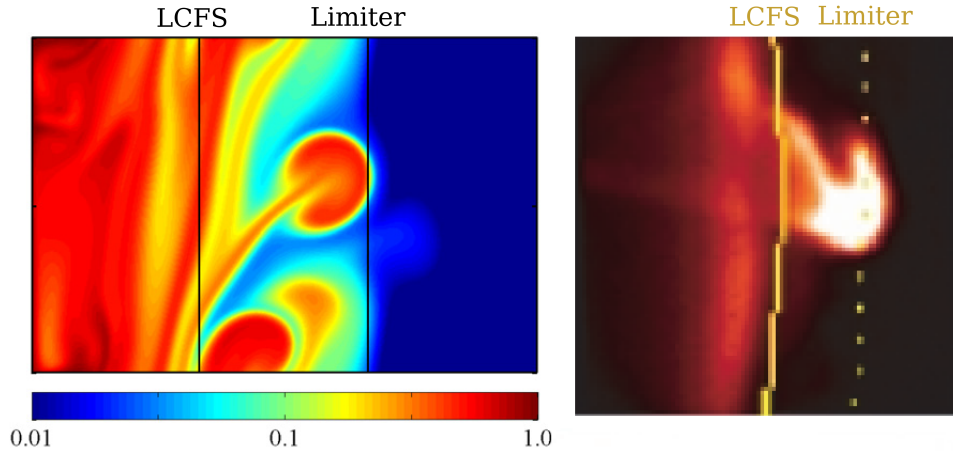


Figure 2.4: Left: Spatial structure of particle density modelled by Electrostatic Edge-SOL (ESEL) code [Garcia et al., 2007a]. Right: Gas puff image (GPI) acquired by 120kS/s camera at NSTX spherical tokamak [Boedo et al., 2006].

Transport in the SOL is neither convective nor diffusive because of turbulent behavior [Garcia et al., 2007b]. Therefore, it is not easy task to create physically correct description of the area. Flow of viscous incompressible fluids is described by Navier-Stokes equation [Navier, 1821]

$$\frac{\partial \mathbf{v}}{\partial t} + (\mathbf{v} \cdot \nabla) \mathbf{v} = -\frac{\nabla}{\rho} p + \eta \nabla^2 \mathbf{v} \quad (2.5)$$

where \mathbf{v} is the fluid velocity, p is the pressure, ρ is the density and η is the

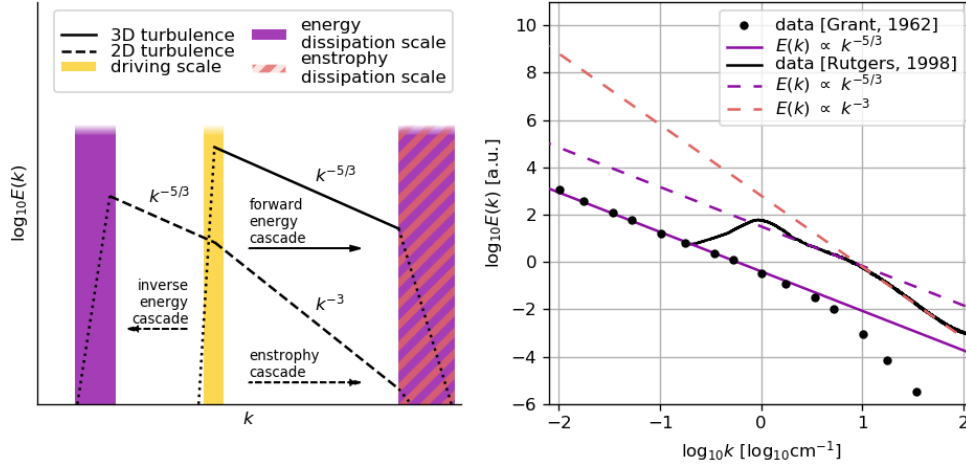


Figure 2.5: Left: Turbulence energy spectrum predicted by Kolmogorov (3D) and Kraichnan (2D). Right: Turbulence spectra from a tidal channel fits Kolmogorov 5/3 law [Grant et al., 1962]. Turbulence spectra of soap films fit Kraichnan’s theory [Rutgers, 1998]

kinematic viscosity. Equation (2.5) can be normalized with respect to the mean velocity of the flow V and the characteristic length of the system L by substitution of normalized variables

$$\mathbf{v}^* = \frac{\mathbf{v}}{V}, \quad p^* = \frac{p}{\rho V^2}, \quad \frac{\partial}{\partial t^*} = \frac{L}{V} \frac{\partial}{\partial t}, \quad \text{and} \quad \nabla^* = L \nabla$$

into eq. (2.5) which results in

$$\frac{\partial \mathbf{v}^*}{\partial t^*} + (\mathbf{v}^* \nabla^*) \mathbf{v}^* = -\nabla^* p^* + \frac{1}{\text{Re}} \nabla^{*2} \mathbf{v}^* \quad (2.6)$$

where $\text{Re} = LV/\eta$ is Reynolds number. Reynolds number is a ratio of inertial and viscous forces in the system. At present an analytic solution of eq. (2.6) is unknown. One of the most celebrated theories in history of turbulence is based on statistics and dimensional analysis done by Kolmogorov.

In 1941, Kolmogorov published his theory (K41 theory) [Kolmogorov, 1941] about turbulence which analyzes the problem from statistical point of view and predicts distribution of energy with scale length (wavenumber) and provides derivation of turbulent energy spectrum. Let us assume source of energy at wavenumber k , e.g. drift waves in tokamak plasma (see Fig. 2.5). These waves will create large scale eddies with energy $\mathcal{E}_{large} \approx u^2$ where u is the velocity of eddies. As the large scale eddy rotates, it will lose energy to smaller scales with dissipation rate per unit of mass $\varepsilon \approx u^2/T_{eddy}$ where $T_{eddy} \approx L_{eddy}/u$ is a turnover time and L_{eddy} scale of the large eddy.

Dissipation of energy will appear at small scales where viscosity of the fluid plays a role, i.e. Reynolds number $\text{Re} = v l_{eddy}/\eta \approx 1$ where v and l_{eddy} is the velocity and scale, respectively, of the smaller eddies. Assumption of this theory is that smaller eddies will not distort much larger eddies because they do not act coherently, thus energy dissipation rate per unit of mass of small

eddies $\epsilon \approx \eta(v/l_{eddy}^2)$ (see last term in eq. (2.6)) is equal to ϵ in statistically steady state. Putting these all together gives us the ratios of driving and dissipation scales

$$\frac{l_{eddy}}{L_{eddy}} \approx \text{Re}^{-3/4}, \quad \frac{v}{u} \approx \text{Re}^{-1/4}. \quad (2.7)$$

K41 theory provides turbulent energy spectrum with the assumption that the small eddies are too small to affect large eddies and feel boundary conditions but not enough small to "feel" the viscosity, thus in the case of time independent solution their energy can depend only on the dissipation rate of the small eddies and wavenumber $\mathcal{E} = \epsilon^\alpha k^\beta$. Dimensional analysis gives us the famous Kolmogorov two-third law

$$\mathcal{E} \approx \epsilon^{2/3} k^{-2/3} \quad (2.8)$$

and the five-thirds law for the energy per wavenumber $\mathcal{E}_k(k) = d\mathcal{E}/k \approx \epsilon^{2/3} k^{-5/3}$ (see Fig. 2.5) which was confirmed in the experiment [Grant et al., 1962]. A transfer of energy from large to small structures is called a forward energy cascade. In two spatial dimensions, however, both the energy and enstrophy is conserved, and therefore the energy can also move from smaller scales to larger scales (inverse energy cascade) and energy in the form of enstrophy which represents rotationality of the flow transfers from larger to smaller scales with $\mathcal{E}_k(k) \sim k^{-3}$ [Kraichnan, 1967]. This is the case of magnetized plasma with strong guide B-field which suppress eddy stretching and vorticity remains conserved. Therefore, processes in this quasi-2D environment comprise both the forward and inverse energy cascade as illustrated in Fig. 2.5.

A mechanism of flow generation by turbulence can be seen from time averaged eq. (2.5) with velocity divided to mean $\langle \mathbf{v} \rangle$ and fluctuating \mathbf{v}' component $\mathbf{v} = \langle \mathbf{v} \rangle + \mathbf{v}'$

$$\langle \langle \mathbf{v} \rangle \nabla \rangle \langle \mathbf{v} \rangle = -\frac{\nabla}{\rho} \langle p \rangle + \eta \nabla^2 \langle \mathbf{v} \rangle - \nabla \langle \mathbf{v}' \mathbf{v}' \rangle. \quad (2.9)$$

The second order term $\langle \mathbf{v}' \mathbf{v}' \rangle$ is called Reynolds stress and represents frictional viscous stress which acts as channel for transport of momentum between turbulence and mean flows. The equation for evolution of Reynolds stress depends on the third order terms $\langle \mathbf{v}' \mathbf{v}' \mathbf{v}' \rangle$ thus leads to a closure problem.

The overview of processes in SOL are shown in Fig. 2.6. The horizontal axis represents amplitude of density δn and temperature δT fluctuations and vertical axis shear of poloidal velocity ∇v_θ . Turbulence in left bottom corner generates blobs with the help of velocity shear and pressure gradient. Blobs grows up and they either fly away and reaches the vacuum chamber or generates shear flows via Reynolds stress. At some point the maximal velocity shear level is reached and the blobs are sheared off by velocity shear [Alonso et al., 2006]. Blobs break up and their energy is dissipated via friction forces. When the blobs are small enough the whole cycle will start again.

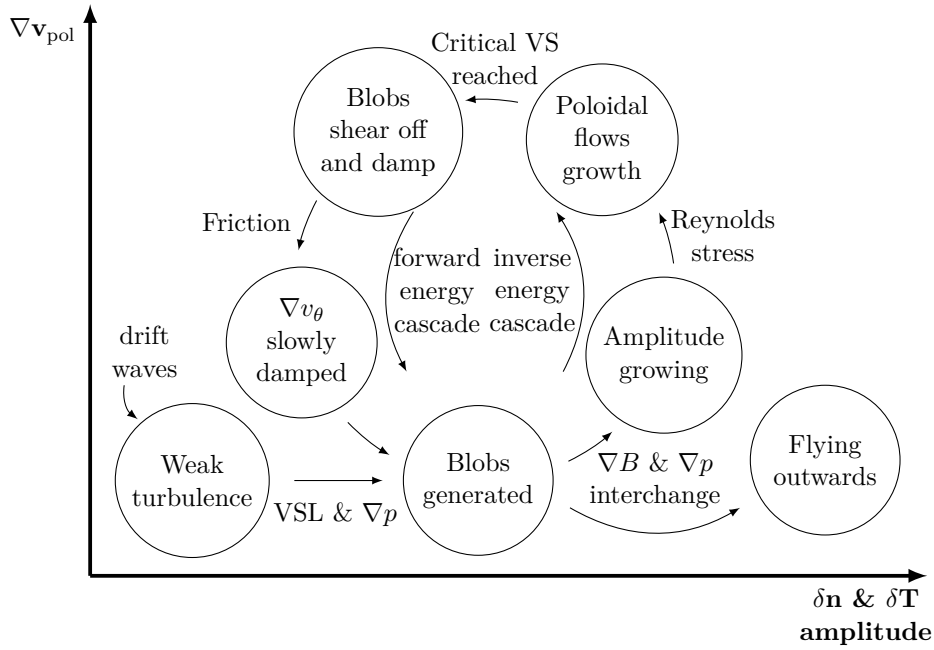


Figure 2.6: Scrape-off layer stability diagram (taken and modified from [Horacek et al., 2010]).

This process can be modeled with predator-prey model [Berionni and Gürcan, 2011]. Interesting part of this cycle from the turbulence suppression point of view is the effect of shear flows.

2.5 Shear flows

Sheared flows can suppress and reduce turbulence via vortex stretching [Terry, 2000]. If the eddy is stretched enough to lose coherence, it will break up to smaller eddies. The fundamental poloidal plasma flow is $\mathbf{E} \times \mathbf{B}$ flow which gives particles drift velocity $\mathbf{u}_{E \times B} = (\mathbf{E} \times \mathbf{B})/B^2$ and is independent of particle charge. Turbulence is suppressed when the shearing rate $\omega_{\text{shear}} \approx \frac{d u_{E \times B}}{dr}$ (concentric circular flux surfaces) exceeds decorrelation rate of the ambient turbulence ω_{corr} [Hahm and Burrell, 1995]. The theory of turbulence suppression by shear flows was supported by experiments with changing sheared flows [Burrell et al., 1992] and with reversed (negative) magnetic shear [Mazzucato et al., 1996] which is perspective for advanced tokamak regimes with internal transport barrier (ITB) [Wolf, 2002]. Special attention is given to poloidal flows called zonal flows because of its role in self-regulation of turbulence.

2.5.1 Zonal flows

Zonal flows are low-frequency (\approx kHz) oscillating poloidal shear flows [Diamond et al., 2005]. Flows get its name because of similarity with lat-

itudal atmospheric and oceanic flows which has also quasi two dimensional nature. Zonal flows are axisymmetrical with mode numbers $m=0$ and $n=0$. Inverse energy cascade transfers energy from turbulence to zonal flow. This self-organization process ends when zonal flows are strong enough to suppress turbulence, i.e. its own source of energy. Predator-prey model is used for time evolution of zonal flows (predator) and turbulence (prey) amplitude [Malkov and Diamond, 2009]. It was shown that the zonal flows can generate transport barrier and trigger H-mode transition [Schmitz et al., 2014]. Triggering of L-H transition by Geodesic Acoustic Modes (GAM; see Section 2.5.2) was also studied but no clear evidence appeared [Bulanin et al., 2016]. Nevertheless, GAMs behavior become target of interest of COMPASS research program.

2.5.2 Geodesic Acoustic Modes

Geodesic Acoustic Mode (GAM) is high frequency (≈ 10 kHz) oscillating branch of zonal flows [Winsor et al., 1968]. Oscillating plasma potential ϕ_E and poloidal flow $v_\theta = ((\partial\phi_E/\partial r) \times B)/B^2$ are toroidally ($n = 0$) and poloidally ($m = 0$) symmetric (see Fig. 2.7).

Non-homogeneity of toroidal magnetic field $\nabla B_\phi \neq 0$ and $E_r \times B_\phi$ compressibility causes cummulation of density. Therefore, density component of GAM has standing wave pattern with $m/n = 1/0$ structure with maximum density oscillation amplitude on the top and the bottom of the plasma column and with a node on the midplane

$$\delta n_{\text{GAM}} = \delta n_0 \sin \theta. \quad (2.10)$$

Generated density gradient drives diamagnetic current $J_d = (B \times \nabla n)B^2$ and quasineutrality condition $\nabla \cdot J = 0$ gives rise to the parallel component of current J_{\parallel} which produces $m/n = 2/0$ (circular plasma) magnetic component of GAM.

Characteristic feature of the GAM, as the word "acoustic" in the name says, is that the frequency of the GAM scales with sound speed c_s

$$\omega_{\text{GAM}} = G \frac{c_s}{R_0} = G \frac{\sqrt{(T_e + \gamma_i T_i)/m_i}}{R_0} \approx \sqrt{T}, \quad (2.11)$$

where R_0 is the major radius of the tokamak, T_i and T_e is the electron and the ion temperature, respectively, m_i is the ion mass, γ_i is the ion specific heat ratio and G is a geometrical factor which depends on the plasma shape:

1. Circular plasma [Winsor et al., 1968]:

$$G = \frac{1}{2\pi} \frac{1}{\sqrt{2 + q^{-2}}} \quad (2.12)$$

2. Elongated plasma (heuristic model) [Conway et al., 2008]:

$$G = 2 \left(\frac{1}{1 + \kappa_b - \epsilon_0} \right) \quad (2.13)$$

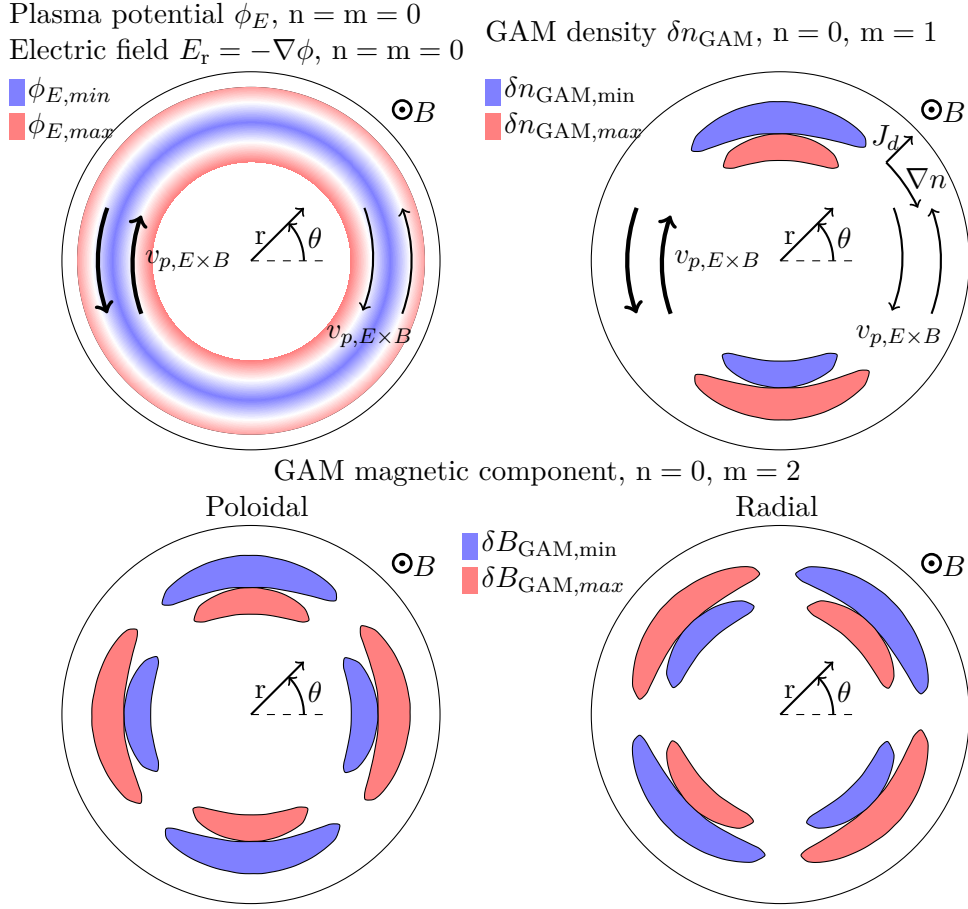


Figure 2.7: Poloidal structure of GAM components for circular plasma.

where κ_b is boundary elongation of plasma and $\epsilon_0 = r/R_0$ is inverse aspect ratio.

3. Elongated plasma (fluid model) [Angelino et al., 2008]. It is easier to define the whole frequency dependence than G coefficient:

$$\omega_{\text{GAM}} = \frac{1}{2\pi} \frac{v_{T_i}}{R_0} \sqrt{(\tau + \gamma_i) \left[\frac{8}{3 - 2\kappa + 3\kappa^2} + \frac{1}{q^2} \right]} \quad (2.14)$$

where κ is local plasma elongation, $v_{T_i} = \sqrt{T_i/m_i}$ is ion thermal velocity, $\gamma_i = 1$ and $\tau = T_e/T_i$

4. Elongated plasma (gyrokinetic model) [Gao, 2010]:

$$\omega_{\text{GAM}} = \frac{1}{2\pi} \frac{v_{T_i}}{R_0} \sqrt{\left(\frac{7}{4} + \tau \right) \left(\frac{2}{\kappa^2 + 1} \right) \left(1 - \frac{s_\kappa}{2} \frac{7 + 2\tau}{7 + 4\tau} \right) \left[1 - \epsilon_0^2 \frac{9\kappa^2 + 3}{8\kappa^2 + 8} - \Delta'^2 \frac{\kappa^2}{4\kappa^2 + 4} + \epsilon_0 \Delta' \frac{4\kappa^2 + 1}{4\kappa^2 + 4} + \frac{(23 + 16\tau + 4\tau^2)(\kappa^2 + 1)}{2q^2(7 + 4\tau)^2} \right]} \quad (2.15)$$

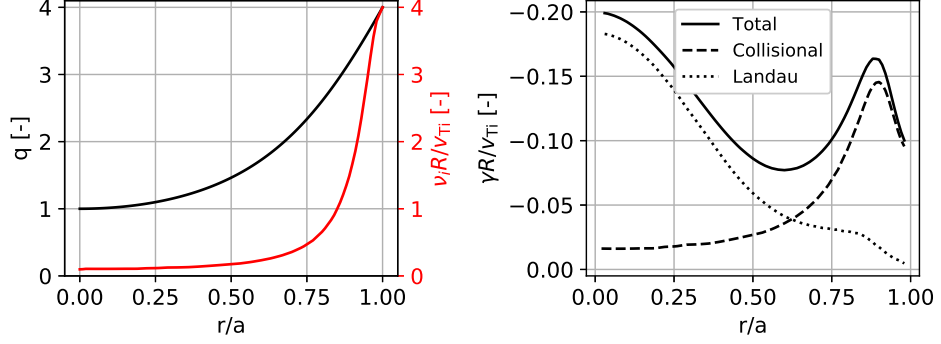


Figure 2.8: Collisional and collisionless (Landau) component of damping rate calculated from (2.16) for combination of q and collisionality profile which produces two minima of damping rate where GAM can appear. Collisionality and q profile taken from [Gao, 2013]

where Δ' is Shafranov shift gradient and $s_\kappa \approx (\kappa - 1)/\kappa$ is radial derivative of the elongation.

Comprehensive comparison of models mentioned above with experimental data was done on ASDEX Upgrade tokamak [Simon et al., 2016]. GAM amplitude and its radial localization depends on the drive and damping of the GAM. GAMs are driven by a non-linear three-wave coupling with ambient turbulent oscillations [Diamond et al., 2005]. GAM is damped by collisionless Landau damping which is usually approximated as $\gamma_L \approx \omega_{GAM} \exp(-q^2)$ and collisional damping which depends on the temperature $\gamma_c \approx \sqrt{T}$. Collisionless Landau damping dominates in the center of the plasma column with low safety factor q and collisional damping dominates at the plasma edge with low temperature T see Fig. 2.8.

Somewhere between those two regions is an area with appearance of GAM if the driving force is sufficiently strong. Damping rate γ and frequency ω , which comprises both damping effect, is given by complex equation [Gao, 2013]

$$\frac{\zeta - i\nu_i}{\zeta} \frac{1}{q^2} + \left[\frac{1}{2} - \frac{1}{2\zeta^2} + \left(\zeta^2 + 1 + \frac{1}{2\zeta^2} \right) (1 + \zeta Z) \right] - \frac{\tau}{4\zeta^3} \left(\zeta + \frac{i\nu_i}{\tau} \right) \frac{[1 - (2\zeta^2 + 1)(1 + \zeta Z)]^2}{1 + i\hat{\nu}_i Z + \tau[1 + \zeta Z]} = 0, \quad (2.16)$$

where $\zeta = \hat{\omega} + i\hat{\gamma} + i\hat{\nu}_i$, $Z(\zeta)$ is plasma dispersion function [Fried and Conte, 2015] and symbols for frequency $\hat{\omega}$, damping rate $\hat{\gamma}$ and collisional rate $\hat{\nu}_i$ with roof are normalized by v_{Ti}/R where v_{Ti} is the thermal ion velocity. Numerical solution of (2.16) for arbitrary normalized collisional rate $\nu_i R / v_{Ti}$ and safety factor q is shown in Fig. 2.8. GAM importance is related to the sheared flows as mechanism of turbulence suppression. Therefore, GAMs (and zonal flows in general) can play a role in transition to enhanced confinement modes.

2.6 Confinement modes

In 1982, the new plasma operation regime with almost 2 times higher confinement time τ_E than usual was discovered [Wagner et al., 1982]. This high confinement state was denoted as the H-mode and the standard regime was denoted as the L-mode. During the H-mode, the edge transition barrier (ETB) creates steep density and temperature gradients region at the plasma edge called as pedestal [ASDEX Team, 1989]. In this region, the poloidal shear flow breaks the turbulence and suppress the cross-field transport (see Section 2.5). New type of instability appeared with H-mode discovery located at the plasma edge called Edge Localised Mode (ELM) [Zohm, 1996].

2.6.1 Edge Localized Modes

ELM causes relaxation of the edge n and T gradients and releases particles out of the pedestal to the tokamak chamber causing high heat energy fluxes to the first wall of tokamak. According to models, these fluxes would melt tiles at first wall of the ITER tokamak [Gunn et al., 2017]. Such a high energy flux is very dangerous and can harm the tokamak first wall. The ELM suppression, high heat flux first wall and the understanding of ELM mechanism are the critical research topics for high performance fusion devices [Wade, 2009].

Most promising description of ELM mechanism is Peeling-Ballooning instability [Snyder et al., 2002]. High pressure gradient (∇p) is driving force for ballooning instability but it also drives large bootstrap current [Miyamoto, 2006] which can cause peeling instability. The combination of high pressure gradient p'_{ped} and high current in pedestal region J_{ped} limits the operation space without ELMs. (see Fig. 2.9)

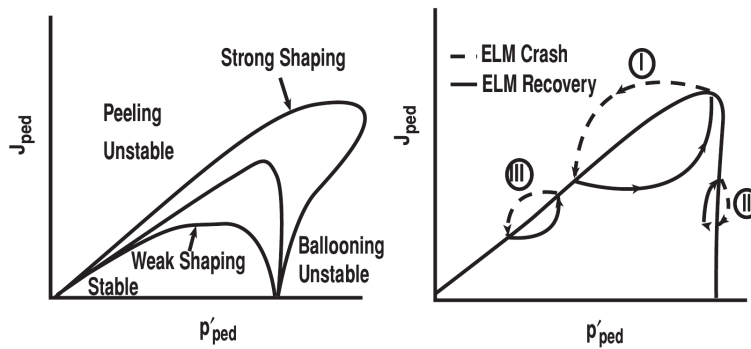


Figure 2.9: Stability boundary of Peeling-Ballooning mode limits the pedestal operational space without ELMs. Present classification of ELMs is as follows: Type I - peeling-ballooning mode, Type II - pure ballooning mode, Type III - pure peeling mode. Taken from [Snyder et al., 2004]

Crossing the stability boundary in the diagram triggers ELM which can have a form of several types depending on the position in diagram. The ELM

physics is also extensively studied on the COMPASS tokamak using both simulation [Dejarnac et al., 2009] and experimental data [Adamek et al., 2016].

■ 2.6.2 I-mode and advanced modes

High confinement regime of plasma is a must for future fusion reactors but at the same time ELMs can carry up to 10% of plasma energy and thus they can damage plasma facing components of tokamaks [Eich et al., 2017]. The H-mode without ELMs (ELM-free H-mode) is a regime with high energy and high particle confinement and can be reached at present tokamaks but this mode is not stable. Low particle transport results in uncontrollable increase of density and impurity accumulation and consequent radiative collapse. This regime usually ends with disruption. Fortunately, several other advanced modes with high confinement time and no ELMs have been discovered:

- **Enhanced D_α (EDA) H-mode** regime has higher particle transport produced by continuous fluctuations called Quasicoherent (QC) mode. This QC mode produced higher particle recycling, and therefore higher D_α radiation which gives the name to this regime [Snipes et al., 1998].
- **I-mode** is H-mode energy confinement time regime with L-mode particle transport which was observed on the ASDEX Upgrade¹ [Ryter et al., 1998] and on the Alcator C-Mod tokamak [Whyte et al., 2010]. Weakly Coherent Mode (WCM) and GAM develop in this regime and are strongly coupled [Cziegler et al., 2013].
- **Quiescent Super H-mode (QSH-mode)** is theoretically predicted mode by the EPED model and first experimental results from DIII-D tokamak fits the theoretical data [Snyder et al., 2015]. The EPED model predicts parameters of the pedestal density and temperature and the aim of the devices is to reach the parameters while remaining in the stable area. The term quiescent describes a steady quiescent edge condition with no ELMs.

It was shown that GAMs are ubiquitous part of I-mode regime and can play a key role in the dynamics and accessibility of the I-mode [Cziegler et al., 2013]. Studies of advanced modes will be a part of research program of the COMPASS Upgrade tokamak [16].

■ 2.7 Density fluctuations

Previous sections mentioned many processes which regulate the particle transport at various timescales. Mixture of these mechanisms presented in the plasma determines behaviour of plasma density at specified location and gives to the density its fluctuating character. The character of fluctuation can be described theoretically (e.g. stochastic behaviour of SOL plasma

¹called "improved L-mode"



Part II

Experimental setup and methodology

Chapter 3

COMPASS tokamak and used diagnostics

High temperature plasma in toroidal geometry is studied at the COMPASS tokamak [Pánek et al., 2006] located at Institute of Plasma Physics (IPP) of the Czech Academy of Sciences. Tokamak COMPASS (COMPact ASSEMBly) (Fig. 3.1) was designed as a flexible tokamak in the 1980s by UKAEA at Culham, UK to explore MHD physics. Therefore, it has very homogeneous toroidal field within the vacuum chamber and a set of magnetic perturbation coils located at both LFS and HFS for creating resonant helical field. Machine with D-shaped vessel started its operation in 1992 and was renamed to COMPASS-D. The device was offered to IPP in 2004 and after installation at IPP it was renamed back to COMPASS.

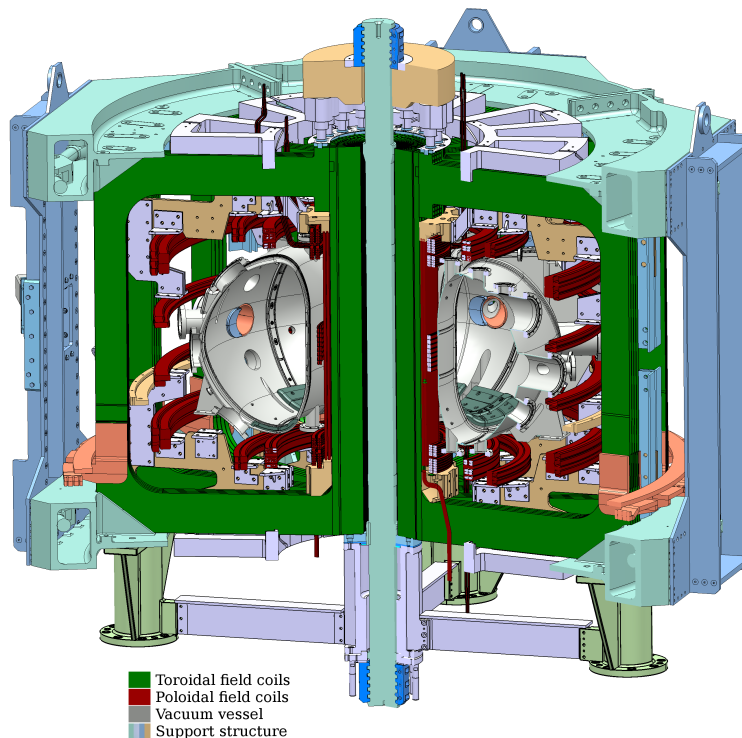


Figure 3.1: COMPASS tokamak without diagnostics and additional heating systems.

3.1 Tokamak COMPASS

Tokamak COMPASS started its operation at IPP in 2008 with research focused on edge plasma physics, e.g. transport in the edge and Scrape-off-Layer (SOL), turbulence structures and intermittent events in edge plasma [Pánek et al., 2006]. The first H-mode discharge was achieved in 2012 [13]. The machine has ITER-like geometry with a single-null-divertor (SND) and clear high confinement mode (H-mode) in ohmic regime and its research contributes to understanding of plasma behavior in next-step devices like ITER. Also configuration with higher triangularity (SNT) can be achieved. COMPASS is equipped with 2×300 kW Neutral Beam Injection (NBI) heating systems which are injected tangentially. NBI can be injected in co- or counter-current direction. Main tokamak parameters are listed in Table 3.1.

Parameter	Value
Major radius R_0	0.556 m
Minor radius a	0.23 m
Number of TF coils	16
Toroidal magnetic field	0.9 - 2.1 T
Plasma current J_{max}	400 kA
Pulse length	~ 300 ms
Elongation κ	1.8
Upper triangularity	0.3
Lower triangularity	0.5

Table 3.1: Main parameters of the COMPASS tokamak.

Thanks to its flexibility, the COMPASS tokamak is well established in the EUROfusion research activities and contributes to (Medium Size Tokamaks) MST tasks and provides ITER relevant experiments [Panek et al., 2018].

3.2 Diagnostics

The COMPASS tokamak is well equipped with diagnostics focused on the edge plasma [7, Weinzettl et al., 2011]. Positions of the diagnostics relevant for the thesis are shown in Fig. 3.2.

Diagnostics used for analysis are described in particular subsections. Li-beam injector used for Beam Emission Spectroscopy (BES) measurement was maintained by the author. Therefore, special attention was devoted for description of this diagnostics in following section which comprises also results achieved during testing and maintenance of the device.

3.2.1 Lithium Beam Emission Spectroscopy

Li-BES is an active spectroscopic method suitable for edge electron density measurement using the line radiation detection of the injected

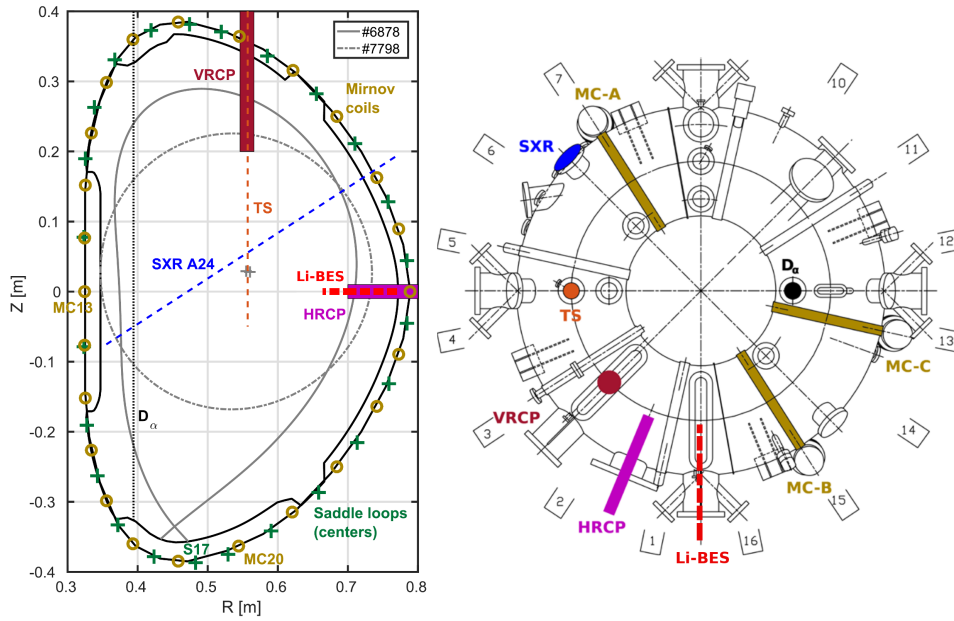


Figure 3.2: Location of diagnostics which are relevant to the thesis. Taken from [2]

lithium atoms. In the past, this technique was used for radial density profile measurement at the TEXTOR [Pusztai et al., 2009, Wolfrum et al., 1993] and DIII-D [Thomas, 1995] tokamaks and nowadays it is used at ASDEX Upgrade [Willensdorfer et al., 2014], JET [Réfy et al., 2018], KSTAR [Lampert et al., 2015] and EAST [Anda et al., 2018, Zoletnik et al., 2018] tokamaks. The method was also successfully used for a 2D plasma density fluctuations measurement at the Wendelstein 7-AS stellarator [Zoletnik et al., 2005].

■ Experimental setup

Experimental setup of the Li-beam on COMPASS is shown in Fig. 3.3. Beam consists of 4 main parts:

1. **Emitter + ion optics:** Emitter contains the ion source which is made of porous ceramic material containing Li atoms. During operation is heated up to 1400 °C to allow emission of Li atoms. Emitter itself is high voltage part of ion optics. It is charged to main acceleration voltage which can reach +120 kV in this case. Extractor electrode is located in front of the emitter and can also handle voltage up to +120 kV but is usually by few kV lower (max $\Delta U \approx 10$ kV) than on emitter to extract the ions from the emitter. Third electrode of ion optics is grounded and with emitter provides voltage for acceleration of ions. The higher energy of the beam the higher penetration depth of the beam (see Fig. 3.4). Ratio of emitter/extractor and extractor/ground voltages influence beam focustion. Last electrode is suppression ring,

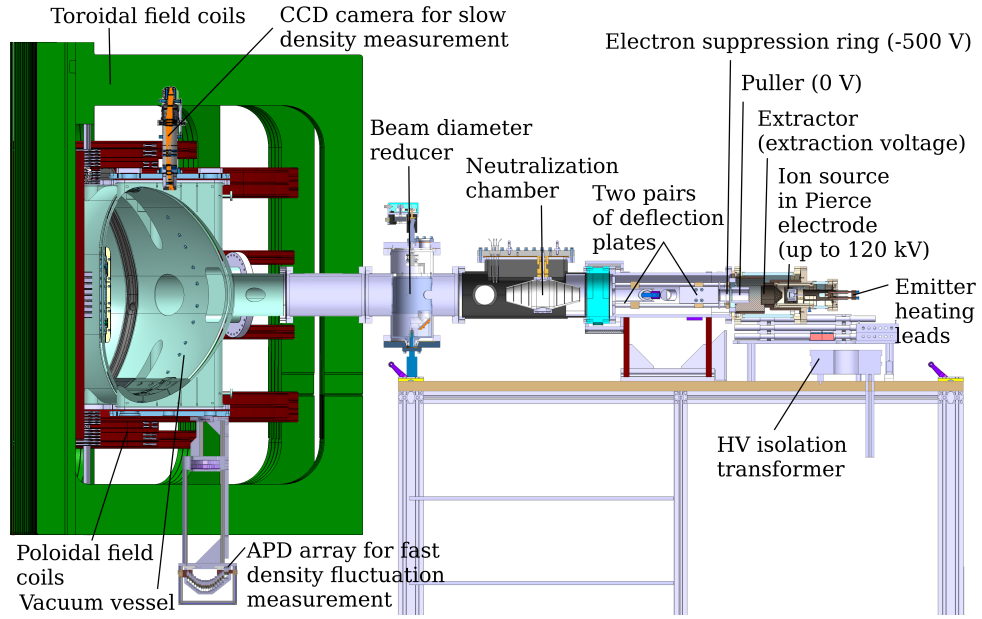


Figure 3.3: Poloidal cross-section of Li-beam experimental setup.

which is charged to -500 V and suppresses electron flux to ion optics.

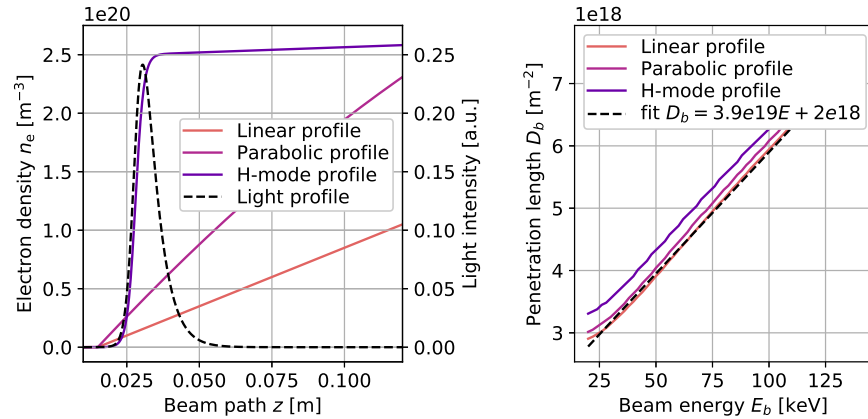


Figure 3.4: Left: Electron density profiles (extreme cases for the COMPASS-U tokamak) used for D_b calculations. Right: Dependence of penetration depth D_b on beam energy E_b for various density profiles.

2. **Reducer:** Reducer is a cylinder with circular holes which serves as diaphragm for reduced beam diameter. Holes are in sizes 20, 10, 5, 3, and 1 mm. Smaller diameter of the beam helps to increase spatial resolution of the beam in poloidal direction but the signal from the beam is lower. Results of the density reconstruction test with reduced beam are shown in Fig. 3.5

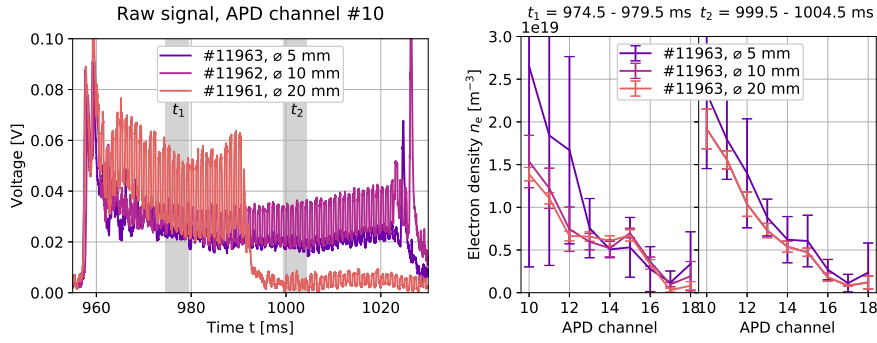


Figure 3.5: Comparison of reconstructed density profile for three different beam diameters in identical plasma shots. Error bars were estimated as a standard deviation of the mean in given time interval.

3. **Deflection plates:** Two pairs of deflection plates deflects the beam with voltage up to 1 kV in toroidal and poloidal direction. Deflection in poloidal direction can be done with frequency up to 400 kHz. Full deflection in toroidal direction, which removes the beam from plasma, is called chopping. Maximal chopping frequency is 250 kHz and limits temporal resolution for density reconstruction because it serves for background signal subtraction.
4. **Neutralization chamber:** Lithium ions are neutralized by charge exchange collisions with sodium atoms in neutralization chamber. Oven at the bottom of neutralization chamber is heated up to 300 °C and creates sodium vapours which condensates at the edges of neutralization chamber and flows back to oven.

■ Detection system

In general, BES is an active spectroscopic method based on injection of neutral atoms into the plasma. These atoms undergo collisional processes due to interactions with plasma particles. A subsequent spontaneous emission of the excited atoms produces photons which are detected by an observation system. Plasma parameters can be estimated from the detected light spectrum. The light radiation is detected both by a CCD camera and by an Avalanche Photo-Diode (APD) system with a high temporal resolution of $0.5 \mu\text{s}$ on the COMPASS tokamak [4, 6]. APD detection system on the COMPASS tokamak is design to collect high amount of photons, and therefore is able to measure interesting density related phenomena (see Fig. 3.6).

The interaction of the beam with plasma can be described by the collisional-radiative (CR) model. The reconstruction of the electron density profile is based on a CR model which is extended by the absolute calibration method described by Schweinzer [Schweinzer et al., 1992]. This self-calibration method allows reconstruct absolute values of density profiles from relatively calibrated light profiles.

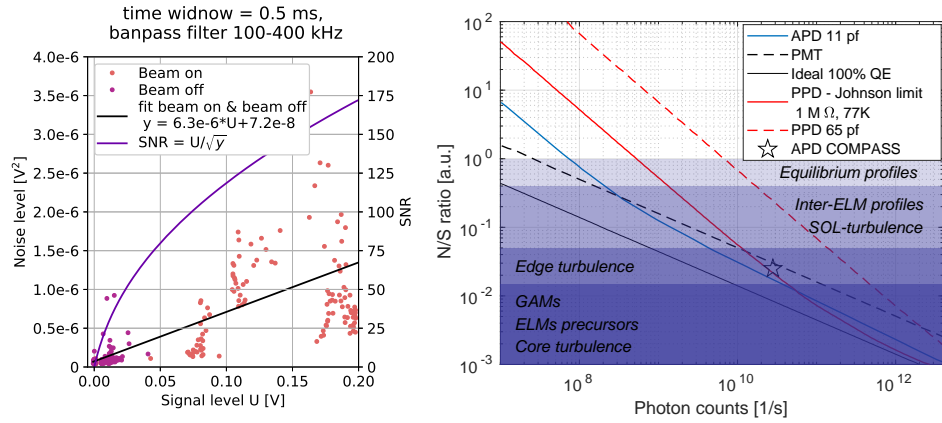


Figure 3.6: Left: Signal to noise ratio (SNR) calculation for the APD channel 11 in the shot #12441. Right: Dependence of Noise to signal ratio (NSR) to photon level for different detector types Taken from [Dunai et al., 2010].

Light signal

The light signals at different positions along the beam path are correlated which is a drawback of BES. The finite decay time of the spontaneous emission together with a fast motion of the beam atoms smears the information about plasma density in the light profile. The beam attenuation along the beam path also causes propagation of the information about the plasma density from the beginning of the beam path to its end via number of neutral lithium atoms which results in anti-correlation of the light signal at the beginning and the end of the light profile. These effects are shown in author's simulation in Fig. 3.7.

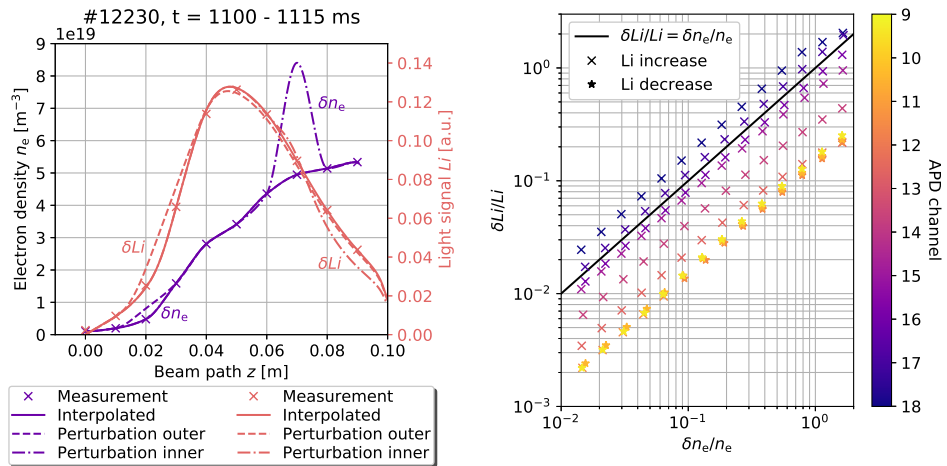


Figure 3.7: Left: Effect of density perturbation δn_e on light response δLi . Right: Dependence of a relative light response on a relative density perturbation for APD channels 18-9.

Time averaged ($t = 1100-1115$) density profile from the plasma shot #12230

and CR model was used for simulation. Density perturbation δn_e with various amplitude was introduced to each APD channel and the response of light profile δLi was calculated (Fig. 3.7 left). It is clear from (Fig. 3.7 left) that the change in light profile is non-local function of electron density $Li(z) = f(n_e(x))$ where $x < z$.

It is shown in Fig. 3.7 that dependence of light response on density perturbation is linear in all channels and decreases towards plasma center because of low amount of unionized lithium atoms in ground state. It can be also seen from Fig. 3.7 that light response is positive in channels close to beginning of the light profile (rising edge) and negative in channels at the end of the light profile (decreasing edge). Therefore, somewhere in between has to be a point which is not sensitive to density perturbation and corresponds to situation when ionization of Li2p state and $2p \rightarrow 2s$ spontaneous emission is in balance with $2s \rightarrow 2p$ excitation. Results of this simulation study was

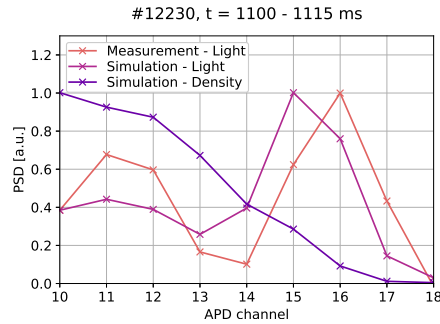


Figure 3.8: Simulation of density fluctuations propagation to light fluctuations revealed the reason for unexpected drop in amplitude in channels 13 and 14. Difference in amplitude between simulation and measurement is given by source of density fluctuations (simulation - SNR = 10 for all channels, measurement - physics)

confirmed in experiment (see Fig. 3.8). Time evolution of electron density profile with Gaussian noise (SNR = 10) proportional to the electron density was transformed to time evolution of light profiles using CR model. Then the integral of band-pass filtered (10-500 kHz) light signal was calculated and compared with light signal from shot #12230 which was processed the same way (Fig. 3.8). The simulation confirmed that drop in light fluctuation level is of artificial origin and not of physical one.

■ Density reconstruction

Artificial phenomena mentioned above must be removed from the light signal by a deconvolution process which results in the reconstructed density [Pietrzyk et al., 1993]. The effect of density reconstruction and comparison of density and light spectrum was presented by the author on Fusetnet PhD event in Prague 2015 poster session [32]. The comparison of light and density cross-correlation function is shown in Fig. 3.9.

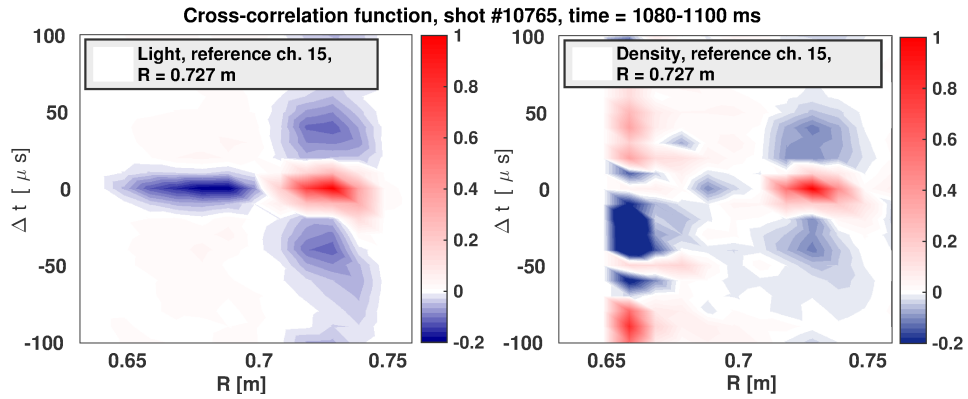


Figure 3.9: Density reconstruction removes strong artificial anti-correlation in the light signals.

The significant anti-correlation in the light signals disappears from reconstructed electron density signals.

A method used on the COMPASS tokamak which is based on Schweinzer's algorithm [Schweinzer et al., 1992] is described in the attached author's article A.1. The advantage of this method is that absolutely calibrated light profile is not needed for the reconstruction. It means that a information about transmittance of optical elements, étendue and beam current in plasma is not required. Compared to the RENATE code [Guszejnov et al., 2012] which is written in IDL and performs forward calculation of the light profile, the reconstruction code in Python was developed to make a forward calculation and a reconstruction without using time consuming optimization methods.

3.2.2 Magnetics

More than 400 coils are mounted on the COMPASS tokamak. They are collected to several groups, e.g. flux loops, saddle loops, Rogowski coils and Mirnov coils (labeled as Discrete coil in Fig. 3.10). Mirnov coils are installed in 3 toroidally separated poloidal rings in number of 24 pieces (Fig 3.2) for each of the following direction: radial, poloidal and toroidal. Magnetic field of GAMs was detected by two toroidally separated poloidal rings of 24 poloidal Mirnov coils and by set of saddle loops. Voltage on a coil U is induced by a change of magnetic flux flowing through the surface S closed by coil's turns. Therefore, coil is impractical for measurement of steady state magnetic field but is useful for measurement of changing field especially for periodically changing field which is the case of GAMs. Maximum of measurable frequency is limited by two phenomena:

1. Coil with its connectors and shielding represent RLC circuit with finite inductance L_{coil} , resistance R_{coil} and capacitance C_{coil} which works as low-pass filter with cut-off frequency. Cut-off frequency of coils are usually measured by fitting of frequency spectrum of coils.
2. Signal from coils is connected to data acquisition system with sampling

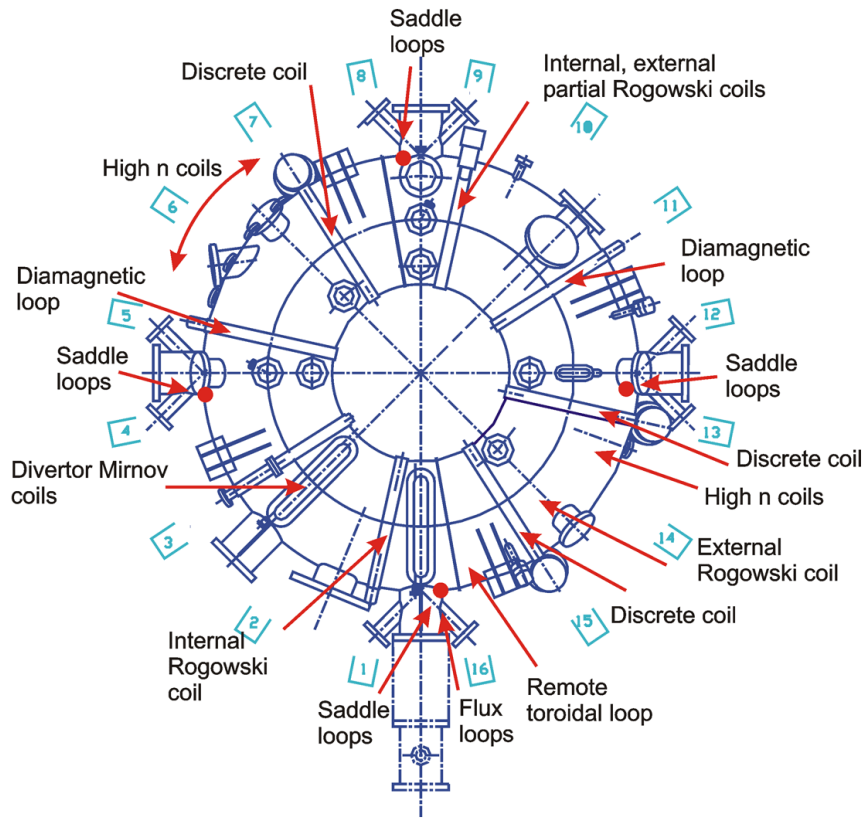


Figure 3.10: Location of magnetic diagnostics on the COMPASS tokamak. Taken from [Havlicek et al., 2009]

frequency of 2 MS/s thus maximum frequency of resolved signal is equal to Nyquist frequency 1 MHz.

The equilibrium reconstruction code called Equilibrium FITing (EFIT) [Appel et al., 2006] takes an input signal from several set of coils to provide position of magnetic flux surfaces, and therefore allows comparison of measurement from diagnostics at different poloidal locations. This is a must in case of comparison Thomson scattering diagnostics Sec. 3.2.4 located vertically and horizontal reciprocating probe Sec. 3.2.3 located on the midplane.

3.2.3 Reciprocating probes

There are vertical reciprocating probe (VRCP) and horizontal reciprocating probe (HRCP) on the COMPASS tokamak, see Fig. 3.11. Reciprocating probe is perturbing diagnostics for measurement of plasma edge parameters. Reciprocating probe consists of reciprocating manipulator and the probe head (Fig. 3.11). Manipulator construction limits the acceleration and position-time waveform of the probe head. Set of the probes on the probe head

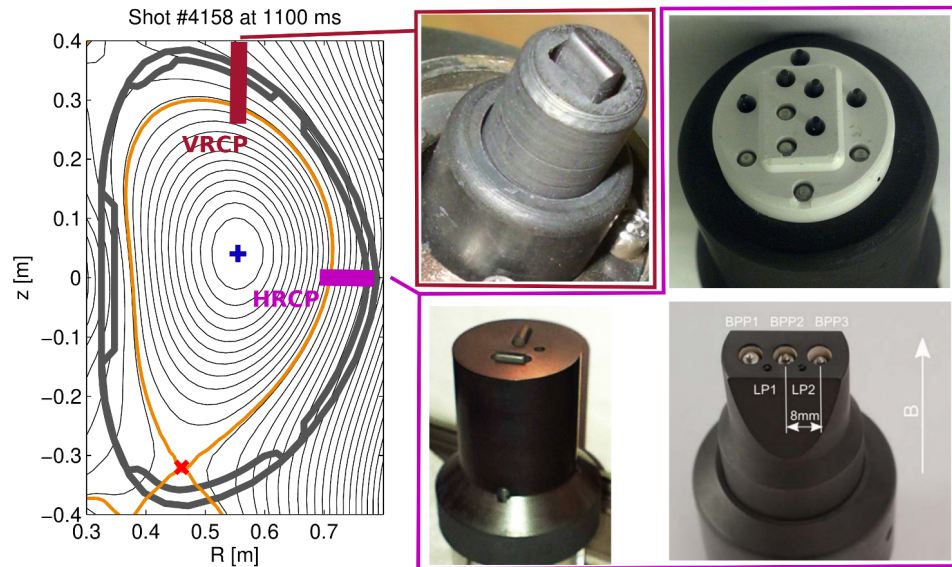


Figure 3.11: Probe head position and various shapes and probe placement on the head. Figures taken from [Vondráček, 2012, Adamek et al., 2014, Dimitrova et al., 2017, Grover et al., 2017]

defines measurable plasma parameters. Probes on the COMPASS tokamak are usually equipped with two kind of probes:

1. **Langmuir probe (LP)** is an electrode inserted into the plasma and charged to time-varying electric potential with respect to wall. Plasma potential, electron density and temperature are estimated from I-V characteristic of the plasma.
2. **Ball-pen probe (BPP)** [Adamek et al., 2010] is modified Langmuir probe with balanced electron and ion saturation currents, and therefore floating potential of the probe is equal to the plasma potential.

Combination of Langmuir and Ball-pen probes at one probe head allows fast simultaneous measurement of floating and plasma potential and thus electron temperature [Adamek et al., 2016].

3.2.4 Spectrometry and optical diagnostics

Optical diagnostics provide unperturbing methods of plasma parameters measurement in whole plasma column. Optical diagnostic used in presented work were

- **Thomson scattering** diagnostic provides electron temperature and density profiles [Bilkova et al., 2018, Bohm et al., 2010].
- **Soft X-Ray (SXR)** detectors [Imrisek et al., 2014] were used for measurement of relative change of temperature at different radial location.

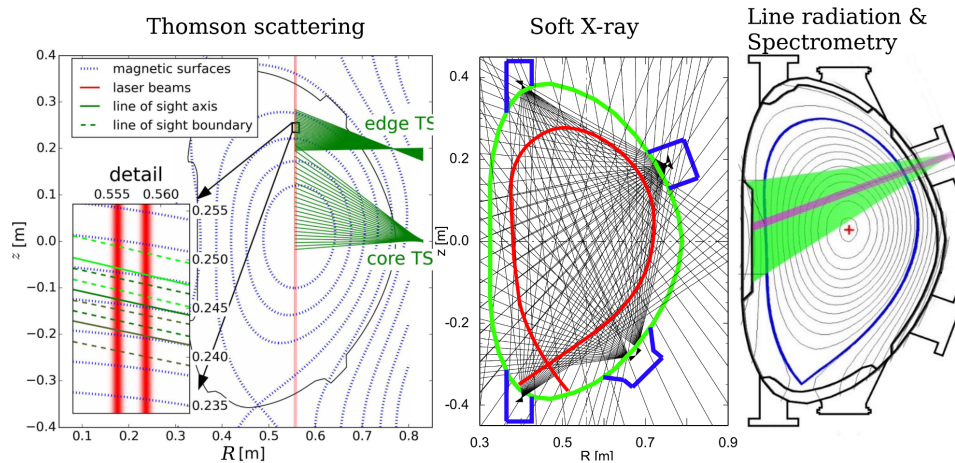


Figure 3.12: Line of sight (LOS) for different optical diagnostics. These diagnostics are at different toroidal locations. Images taken from [Stefanikova et al., 2016, Weinzettl et al., 2010, Naydenkova, 2017]

- **Spectroscopic** measurement provide temporal evolution of selected spectral lines on the COMPASS tokamak [Naydenkova et al., 2009, Naydenkova et al., 2012]. The D_{α} , He I and C III spectral lines were chosen for relative comparison of element abundances in the plasma.

■ 3.2.5 Other diagnostics

The diagnostics which did not fit to the previous sections but were used in presented results are mentioned below:

- **Neutral Particle Analyzer (NPA)** simultaneously measures energy spectra of deuterium and hydrogen atoms escaping the plasma with temporal resolution 50 - 1000 μs . If localization of neutral particle source in the plasma is known, the temperature of corresponding ions is obtained by fitting of energy spectrum [Mitosinkova et al., 2016].

Diagnostics	Measured quantity	Measurement area	Spatial resolution	Temporal resolution
Li-BES	n_e	SOL & Edge	cm	250 kHz
Mirnov coils	B_θ	SOL & Edge & Core	non localized	2 MHz
Rec. probes	n_e, T_e, V_{fl}, V_{pl}	SOL	mm	2 MHz
Thomson scattering	n_e, T_e	Edge & Core	mm	40 Hz ¹
D $_\alpha$, HeI, CIII	radiation	Edge	non localized	2 MHz
SXR	radiation	Core	\sim cm	2 MHz
NPA	T_i	Core	\sim cm	1 kHz

¹ Compared to other diagnostics, the signal is not averaged over 1/40 s time windows but it is 7 ns pulse

Table 3.2: Basic parameters of diagnostics on the COMPASS tokamak with measured quantities used in presented work.

3.3 Diagnostics summary

Overall set of diagnostic tools determines the ability of diagnostics to study individual physical topic in tokamak research program. Each diagnostics provide information from different plasma region at different temporal and spatial scale. The characteristic features of diagnostic systems used in this theses is summarized in Table 3.2. There are some limitations which results also from location of the diagnostics, e.g. Li-BES on midplane ($\theta = 0$) cannot directly measure GAM density fluctuations see (2.10). Therefore, proper combination of measurement techniques is a must to acquire enough information for description of phenomena in the plasma.

Chapter 4

Statistical tools and data preprocessing

This chapter provides basic information about commonly used methods for signal analysis on the COMPASS tokamak. Most of the methods are implemented in the standard numerical libraries of numerical computing environment as Python or MATLAB, and therefore no effort in code development is required in this sense. Detailed information about used algorithms can be found in manual page of each library e.g. SciPy [SciPy, 2019].

Statistical tools are only briefly mentioned in this chapter. Details of statistical data analysis can be found in [Cowan, 1998, Sivia and Skilling, 2006].

Signals from diagnostics stored in COMPASS database (CDB) are preprocessed before using in equations. The main reasons are to remove parasitic signal or to unify spatial and temporal axis of different signals. Then the signals can be used in equations or statistically analyzed. Signal can be processed in time or frequency domain. The frequency analysis of signals is preferable for harmonic signals. Functions based on Fourier transformation have to be used in this case. Let $x[\cdot]$, $y[\cdot]$ denote discrete signals and $x(\cdot)$, $y(\cdot)$ represent continuous signal for the following sections.

4.1 Preprocessing

Preprocessing consists of any process applied on signal which precede the main analysis of the signal.

Raw signal usually contains parasitic signal or noise. If the noise occupies different part of frequency spectra than useful signal, spectral filters can be used to suppress noise. High-pass filters are also used if the trend of the signal has to be zero e.g. for cross-correlation function. Signals preprocessing can include some of the following processes:

- **Filtering** [Smith et al., 1997, Taylor and Williams, 1995] is a process of removing specific frequency component from a signal. Different types of filters exist for this purpose see Fig. 4.1. Filters are characterized by their transfer function

$$H(z) = Y(z)/X(z) \quad (4.1)$$

where $Y(z)$ and $X(z)$ are Z-transformed input and output signals [Jury et al., 1964]. Since a plenty of filters are implemented in SciPy or

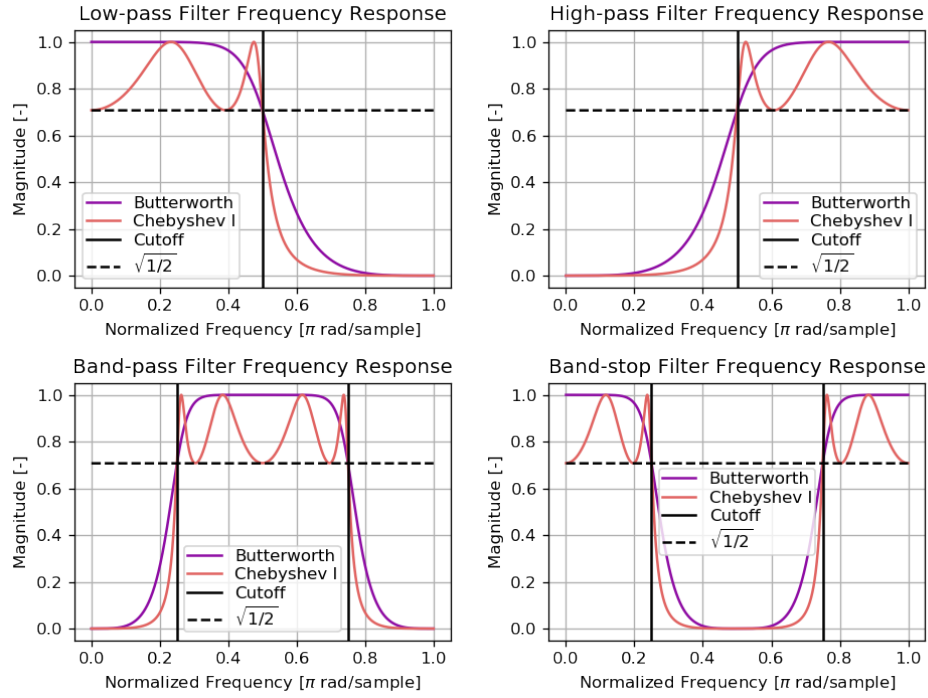


Figure 4.1: Different types of filters of 4th order with cut-off frequencies matching the attenuation of amplitude by $\sqrt{1/2}$ i.e. -3 dB.

MATLAB library, users do not need to construct own filters but only specifies cut-off frequencies and order of filters. A filter type overview from the construction and pass-band point of view for Butterworth [Butterworth et al., 1930] and Chebyshev [Weinberg, 1957] filter is shown in Fig. 4.1.

To prevent phase shift of different frequency component of a signal, a two pass filtering is used. First pass removes required frequencies from the signal and introduces frequency dependent phase shift into the signal. Second pass is applied to the time reversed signal thus the frequency dependent phase shift is introduced with reversed time thus the resulted phase shift is zero. In a the case of median filter of length M_f , the filtered signal is delayed by $(M_f - 1)/2$ samples.

- **Downsampling** is a process of decreasing sampling frequency of the signal. It is done in two steps. First the low-pass filter is used on the signal to prevent aliasing of high-frequency component of signal. Second the signal decimated by integer factor M_d as $x_d[j] = x[M_d j]$.
- **Upsampling** is a process of increasing sampling frequency of the signal. It can be done either by method similar to downsampling (fill the $M_u - 1$ points between sampling points by zeros and then use low-pass filter to smooth discontinuities) or by interpolation. Linear and cubic spline methods was used in this work. Cubic spline method was used when

continuous first derivative of the signal was required. It is worthwhile to mention that any of these methods do not add new information to the signal. In the case of known theoretical prediction on spatial or temporal shape of signal, the interpolation can be done by fitting of analytic function see Section 4.4.

Upsampling or downsampling has to be used when two signals have different sampling of temporal or spatial axis and has to be compared. This is a usual case for signals from different diagnostics.

4.2 Signal analysis

Waves in plasma are usually analyzed in their frequency domain. Frequency spectrum is obtained by Discrete Fourier Transform (DFT) [Press et al., 2007].

- **Discrete Fourier transform** converts signal with N samples from time domain $x[j]$ to frequency domain $X_f[s]$ and is defined as

$$F(x)[s] = X_f[s] = \sum_{j=0}^{N-1} x[j] \exp\left(-i\frac{2\pi}{N}js\right), \text{ for } s = 0, 1, \dots, N-1. \quad (4.2)$$

Inverse DFT for conversion of signal back to time domain is defined as

$$F^{-1}(X_f)[j] = x[j] = \sum_{s=0}^{N-1} X_f[s] \exp\left(i\frac{2\pi}{N}js\right), \text{ for } j = 0, 1, \dots, N-1. \quad (4.3)$$

Spectral resolution $\Delta\omega$ is given by

$$\Delta\omega = \frac{\omega_s}{N}, \quad (4.4)$$

where ω_s is sampling frequency. Consequently, the lower frequency has to be resolved the longer time series is required for fixed ω_s . This is limiting factor in the situation when frequency of the wave evolves during time. Trade-off between temporal resolution of frequency evolution and spectral resolution has to be done. Visual representation of time evolution of spectrum is called spectrogram and is shown in Fig. 4.2. DFT is implemented as fast Fourier transform (FFT) algorithm in standard numerical libraries [Press et al., 2007].

Let us assume two periodic signals (waves in plasma) with the same sampling frequency. A level of similarity of these signals can be expressed by cross-correlation function or coherence.

- **Cross-correlation** function of two discrete signal $x[\cdot]$ and $y[\cdot]$ is defined as

$$r_{xy}[j_2] = (x \star y)[j_2] = \frac{1}{N} \sum_{j_1=0}^{N-1} x[j_1]^* x[j_1 + j_2], \quad (4.5)$$

where $x[\cdot]^*$ denotes complex conjugate of $x[\cdot]$.

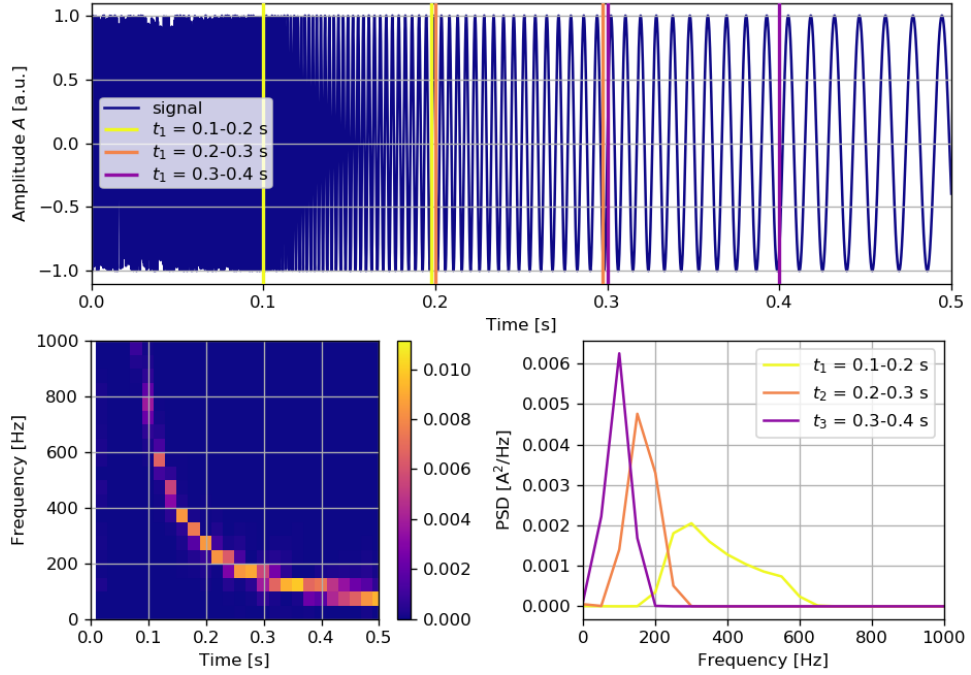


Figure 4.2: Spectrogram (bottom left) and spectrum (bottom right) of exponential down-chirp signal (top).

- **Auto-correlation** function is a special case of cross-correlation $r_{xx}[j_2]$.

Total energy content in the signal E can be defined via auto-correlation as

$$E = \sum_{j=0}^{N-1} |x[j]|^2 = r_{xx}[0]. \quad (4.6)$$

Therefore, applying Parseval's [Parseval des Chênes, 1806] and convolution theorem [Daniell, 1920] we get

$$E = \sum_{j_2=0}^{N-1} |x[j_2]|^2 = \sum_{s=0}^{N-1} |F(x)[s]|^2 = \sum_{s=0}^{N-1} F((x \star x)[j_2])[s] = \sum_{s=0}^{N-1} P_{xx}[s], \quad (4.7)$$

where P_{xx} is power spectral density (PSD). Consequently, P_{xx} is related to auto-correlation function via Fourier transformation as

$$P_{xx}[s] = F(r_{xx})[s]. \quad (4.8)$$

Analogously, cross power spectral density (CPSD) P_{xy} is defined as

$$P_{xy}[s] = F(r_{xy})[s]. \quad (4.9)$$

Cross-correlation extract information about similarity of the signal in time domain. Method for estimate of similarity in spectral domain is called coherence.

- **Coherence** of two signal is defined as

$$C_{xy}[s] = \frac{|P_{xy}[s]|^2}{P_{xx}[s]P_{yy}[s]}. \quad (4.10)$$

Advantage of C_{xy} compared to the r_{xy} is that C_{xy} is from the interval $(0, 1)$. This allows to set a fixed threshold level of coherence for signals with different amplitudes for further processing.

If the periodic signal has periodically modulated amplitude then the envelope of the signal can be obtained using Hilbert transform of the signal [Ulrich, 2006]. Envelope of arbitrary up-chirp signal and Hilbert transform of the signal is shown in figure 4.3. Envelope corresponds to absolute value of analytic signal [Cohen, 1995].

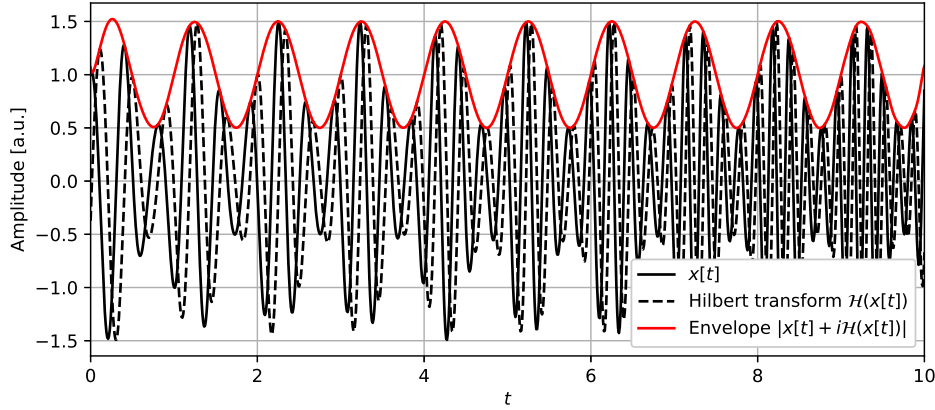


Figure 4.3: Envelope of up-chirp signal estimated using Hilbert transform.

4.3 Statistical tools

Stochastic processes in the plasma can be evaluated by statistical tools. Data series can be represented by probability density function (PDF) $p(x) \geq 0, \forall x$ which satisfy

$$\int_{-\infty}^{\infty} p(x) dx = 1. \quad (4.11)$$

Then the data series can be characterized with n-th moment of PDF

$$\mu_n = \int_{-\infty}^{\infty} x^n p(x) dx. \quad (4.12)$$

The first moment is mean value μ and the second moment is variance σ^2 if $\mu = 0$. In the case that data did not follow Gaussian distribution, the cumulative distribution function (CDF) has to be calculated. For this case, median and percentile represents the scatter of the data.

4.4 Optimization

When there is more equations than unknown variables we speak about overdetermined system. In the case that any set of equations gives the same result than unnecessary (linearly dependent) equations can be thrown out. More likely, any set of equations will provide different results. Typical situation is a physical measurement where different kind of noises contribute to a useful signal and measurements are imprecise. Therefore, optimization methods has to be used to find approximate solution for overdetermined system [Snyman and Wilke, 2018, Nocedal and Wright, 2006]. The most commonly used optimization methods are:

- **Least squares** method was first published by Adrien-Marie Legendre when solving overdetermined system of equation for movement of comets [Legendre, 1805]. This method minimizes the sum of squared difference between an observed value y_i and the fitted value provided by a model $f(x[j], \alpha)$

$$\min \left(\sum_{j=1}^N (y[j] - f(x[j], \alpha))^2 \right) \quad (4.13)$$

where α is vector of fitted parameters and N is a number of samples. This method considers only errors in dependent variable. More general method of total least squares can handle errors in both variables.

- **Total least squares** (TLS) method [Golub and Van Loan, 1980] is used if measured data has uncertainty in both independent and dependent variable. Moreover if the errorbars are not same for all measured points the weighted TLS (WTLS) method is used. TLS methods are not a part of MATLAB libraries, and therefore MATLAB toolbox for weighted total least squares approximation [Markovsky and Huffel, 2004] was used in presented results.



Part III

Results

Chapter 5

Plasma fluctuations

This chapter focuses on author's results related to plasma edge density measurement using Li-BES.

5.1 Reconstruction algorithm

The author developed fast reconstruction algorithm for transformation of Li-BES light profile to electron density profile. The developed algorithm allows routinely reconstruct signals with $2 \mu s$ temporal resolution. Moreover, the author derived and implemented method for estimation of electron density measurement uncertainty. This achievement was published in [1] (see article attached in Appendix A.1). The article consist of three key parts:

1. description of the reconstruction process and error estimation method in detail,
2. presentation of reconstructed profile with estimated error and reconstructed signal with $2 \mu s$ temporal resolution,
3. results on reconstruction execution time.

Detailed information can be found in article attached in Appendix A.1).

5.2 Comparison with other diagnostics

The method is in routine operation when experiment on COMPASS requires density profiles from Li-BES diagnostics. Comparison of reconstructed density with other diagnostics is the essential act of all diagnostics, which has been already done in previous work [4] with slow reconstruction algorithm Fig. 5.1, and therefore the article [1] does not contain this comparison.

Although the reconstruction algorithm was different, the core of the algorithm (CR model) was the same because it is not influenced by reconstruction method. Moreover, the comparison is also presented in the diagnostics overview article [7] where the author also contributed with temporal electron density evolution during the ELM event (Fig. 5.2).

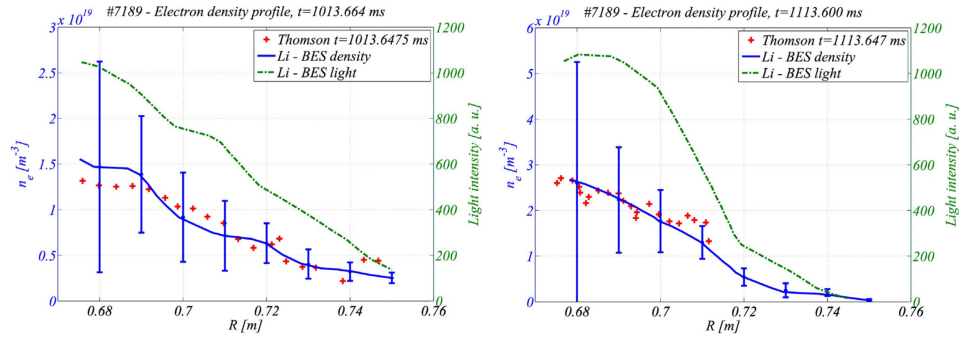


Figure 5.1: Comparison of electron density profiles from Li-BES and Thomson scattering diagnostics. Taken from [4]

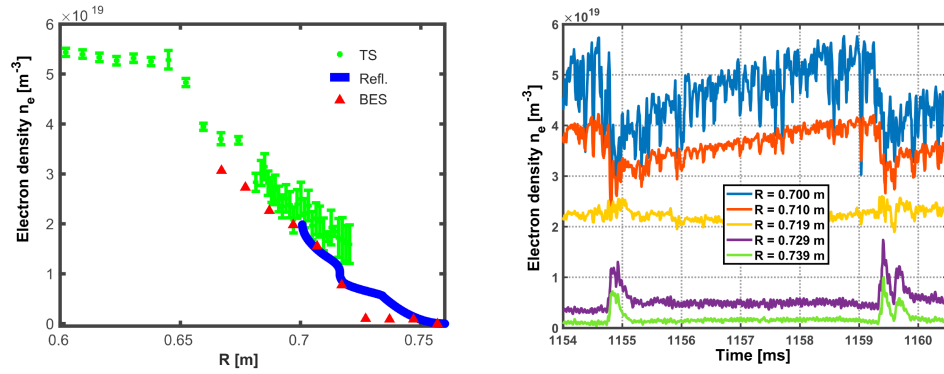


Figure 5.2: Left: Comparison of electron density profiles from Li-BES, Reflectometry and Thomson scattering diagnostics. Right: Temporal evolution of electron density during ELM measured by Li-BES. Taken from [7]

5.3 Measurement of ELMs

The author continued in fast measurements of ELMs during campaign of shots with nearly constant ELM frequency and estimated density evolution of the average¹ ELM (see Fig. 5.3).

This effort resulted in publication of ELM averaged density at the top of the pedestal in [5] to support the statement that only fully developed pedestals are included in the analysis if measurements performed during the last 30% of ELM cycle are used, see Fig. 5.4.

¹There was two methods used for average ELM density calculation: The first, the beginning of each ELM is detected and averaging is done over given time window defined from start of the ELM. The second, the end of the ELM is represented by the beginning of the next ELM; therefore, time axis was converted to ELM cycle percentage defined by the beginning and the end of the ELM. Averaging is done over ELM cycle percentage window. The second method was used for calculation of average pedestal density.

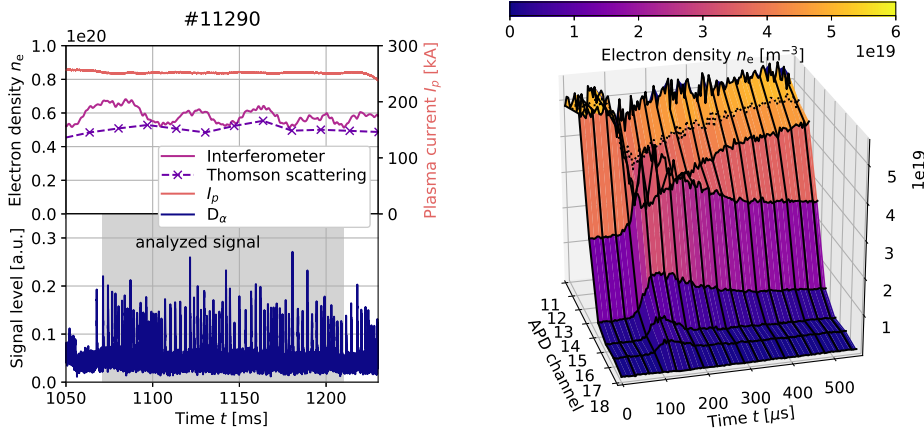


Figure 5.3: Temporal evolution of electron density during average ELM. Data are averaged over interval with constant plasma current and line averaged electron density (gray area on left). Density in channel 12 (dotted line) is linearly interpolated using channels 11 and 13 because of high measurement error in channel 12.

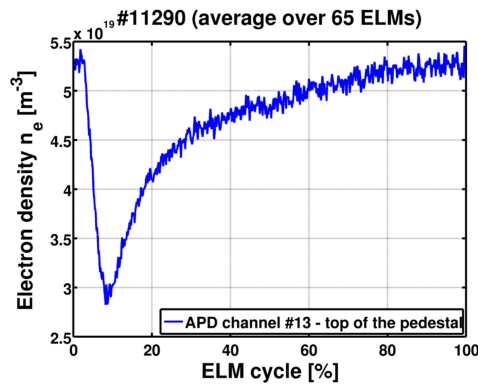


Figure 5.4: Evolution of electron density on top of the pedestal during the ELM cycle measured by Li-BES. Taken from [5]

It is necessary to mention that Li-BES diagnostic is capable of ELM precursor measurement even on light signal; however, the anti-correlated signal is present as it is shown in Fig. 5.5. It is also seen in Fig. 5.5 that ELM precursor oscillation are not present in D_α signal, and therefore contribution of background radiation to signal is negligible.

5.4 Summary

The author developed code for a density reconstruction of the Li-BES signal and derived method for estimation of density measurement error, which allows to study plasma density fluctuations, especially in the field of ELM physics. The developed code allows to the author contribute to several articles [4, 5, 7]. Fast implementation of this code and overall reconstruction process

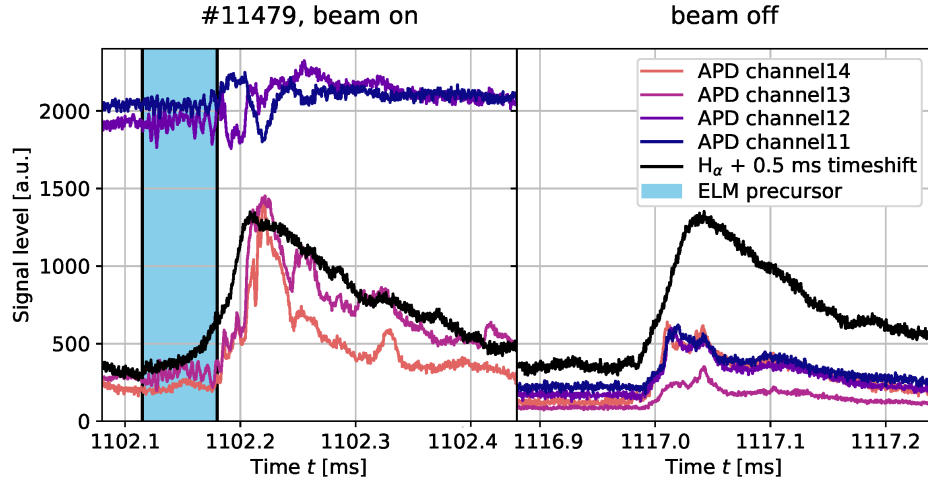


Figure 5.5: Small fluctuations on the Li-BES signal preceding main ELM event can serve as a precursor of this event. Right image shows the background signal level during ELM event.

from raw Li-BES $2 \mu\text{s}$ data to plasma density together with uncertainty error estimation was published in his first-author publication [1]. Author's expertise and reconstruction code will be used in the design and research phase of Li-BES on COMPASS Upgrade tokamak, although significantly higher densities will allow only measurement in the SOL region [12].

Chapter 6

Geodesic Acoustic Modes

Lithium beam on the COMPASS tokamak is injected on the midplane where a node of GAM density fluctuations exists as described in eq. (2.10), and therefore direct measurement of density oscillations is not possible. Key diagnostics in measurement of GAMs were reciprocating probes and magnetic diagnostics. Probes can measure fluctuations of plasma potential and radial electric field and also provide electron density and temperature profile. Signal in saddle loops and Mirnov coils is generated by magnetic component of GAM. Results of GAM exploration on COMPASS tokamak were published in the overview article [2] (see article in Appendix A.2) where the author of the theses is listed as a second author. Author's contribution to the article was:

1. analysis of GAM frequency scaling with temperature (Fig. 6 in the article),
2. calculation of collisional and Landau damping of GAM at the edge (Fig. 2 in the article),
3. analysis of GAM amplitude scaling with plasma elongation and safety factor (Fig. 5 in the article).

The first item is closely related to author's contribution in [3] with Figures 2. and 3. in the article. The author analyzed GAM amplitude and frequency evolution during NBI heated plasmas and obtained results was used to support the theoretical model on GAM driven by electron and ion fluxes.

Following sections describe previously mentioned contributions in more detail but comprehensive explanation of selected topics is described in the attached articles (Appendices A.1,A.2,A.3).

6.1 GAM frequency scaling

The existence of GAM in the tokamak device is verified by measurement of its fundamental features, i.e. plasma potential oscillations are $m=n=0$ symmetric and the oscillation frequency scales with ion sound velocity as in eq. (2.11). NBI heated shots were analyzed because of high change of the ion temperature during the shot. During the analysis the author had to solve few challenges:

- NPA diagnostics provides the ion temperature only in the center of the plasma column,
- the GAM frequency was measured by Mirnov coils, which is a non local measurement, and therefore the GAM radial localization was unknown,
- GAM frequency also depends on the isotopic composition of the plasma which may slightly change during the shot or in between shots. This can happen due to plasma-wall interaction,
- since measured GAM frequency deviates from the Winsor's theoretical predictions in elongated plasma [Simon et al., 2016]. Several GAM frequency scaling laws exist (see eq. (2.12),(2.13),(2.14),(2.15)) with varying success rate for frequency predictions.

To resolve these challenges, the author collected all available signals, which are necessary for GAM frequency estimation, and put them to one file called GAM database (GAMDB). Within GAMDB all signals were resampled to have the same temporal and spatial resolution, e.g. electron temperature profile from TS diagnostics was fitted by analytic function [Stefanikova et al., 2016] to obtain electron temperature in the points of GAMDB spatial grid. The ion temperature profile was obtained by scaling of electron temperature fit to match the central ion temperature measured by NPA (it was assumed that T_i and T_e has the same shape of the profile).

Plasma parameters, which are not measured on the COMPASS tokamak, were obtained by minimization of difference between measured and estimated parameters from predictive code METIS [Artaud et al., 2018] with inputs from GAMDB. The author also tried this technique for T_i profile estimation but due to relatively large degree of freedom of METIS tuning parameters, high computational demands and similar results as the previous method, the previous method was used in this case.

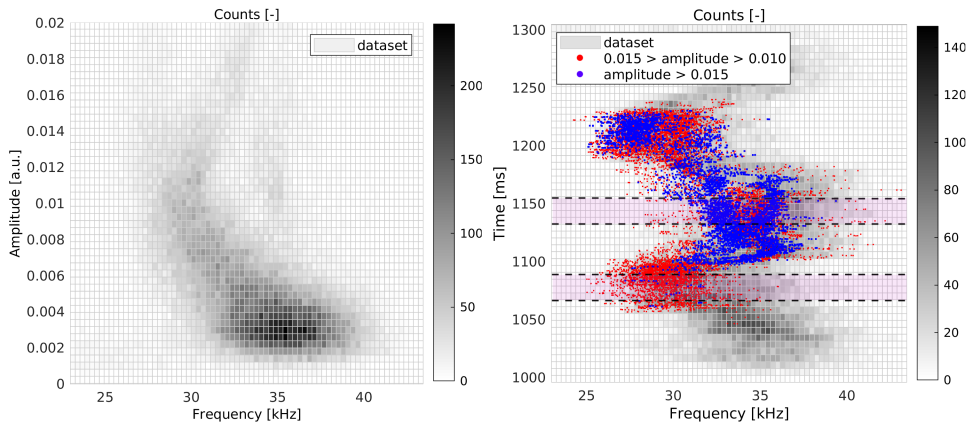


Figure 6.1: Two slices in the GAM database (amplitude-frequency and time-frequency-amplitude space) with aggregation over the rest of the dimensions (density, plasma current etc.). Black dashed lines border two shot phases (ohmic and CO-NBI) used for the analysis.

Plasma current	X-point coordinates	n_e profile
Line averaged n_e	Magnetic axis coordinates	T_e profile
q profile	Poloidal cross-section area	Central T_i
κ profile	NBI current	HeI radiation
Δ profile	RMP current	CIII radiation
Upper, lower triangularity		H_α radiation

Table 6.1: List of plasma parameters stored in GAMDB (including temporal evolution).

GAMDB can be seen as a multi-dimensional space of measured and computed plasma parameters and GAM frequency and amplitude. Hyper-plane cuts in this space are beneficial for selecting GAM frequencies which meet defined criterion, e.g. select only data where HeI/ H_α ratio is lower than a defined value to control isotopic composition of the analyzed plasmas. Fig. 6.1 illustrates data selection of signals with high enough amplitude (> 0.01 a.u.) and drop out of signal acquired during shaping phase of the plasma. The rest of counts in the right graph corresponds to amplitude lower than 0.01 a.u. All plasma parameters stored in GAMDB are listed in Table. 6.1.

Finally, WTLS fit of theoretical and measured data was calculated at different radial locations and for different scaling laws. The case with the lowest misfit given by the WTLS estimate was found and is plotted in Fig. 6 [2] (Appendix A.2) showing a linear scaling of GAM frequency with the edge ion sound speed.

6.2 GAM damping

The author numerically solved equation (2.16) for T_e and n_e measured by reciprocating probe and q obtained from EFIT. This equation quantifies total damping of GAM which consists of collisional and collisionless (Landau) damping. Obtained results explained why GAMs edge appears at given radial position. Radial extent of the GAM is limited by increase of damping rate at the plasma edge as shown in Fig. 6.2.

It was observed that GAM is located deeper inside plasma column in circular plasmas than in the diverted. The reason is that damping rate in the circular plasma starts to increase deeper in the plasma column, and therefore suppress the GAM as is shown in Fig. 2 [2] (Appendix A.2).

6.3 GAM amplitude scaling

As the Landau damping increases with q , the GAM amplitude is expected to scale with q as well. The author verified this assumption using data collected during campaign dedicated to GAM measurement with a scan over edge safety factor q_{95} and boundary elongation κ_b . The result was published in Fig. 5 [2] (Appendix A.2).

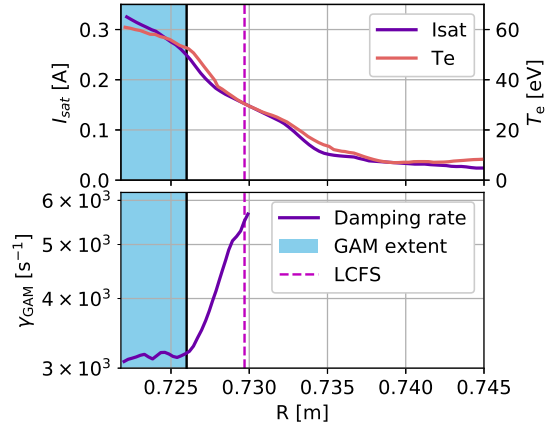


Figure 6.2: Top: Radial profile of ion saturation current $I_{sat} \sim n_e$ and electron temperature T_e are input data for calculation of GAM damping rate. Bottom: Radial profile of GAM damping rate with position of LCFS and measured radial extent of the GAM (blue area).

The author continued with the analysis of GAM amplitude during NBI heated plasmas with co- and counter-current injection. Despite the fact that only a limited set of shots with counter current NBI injection was available, there was an indication that the GAM amplitude changes in the opposite way for co- and counter-injection as shown in Fig. 6.3.

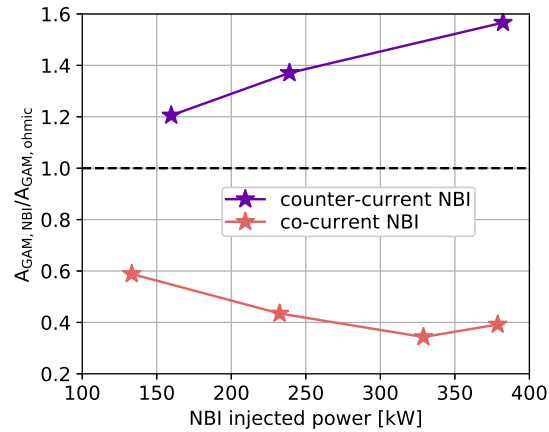


Figure 6.3: Impact of NBI injected power and direction on GAM amplitude. Absorbed power in the plasma is different from injected power, but in this measurement was not evaluated.

This behavior was theoretically described in [3], where the author contributed with measurement and data post-processing represented by Figs 2 and 3 to support the theoretical model (Appendix A.3).

■ 6.4 Summary

The author compiled signals from different diagnostic systems on the COMPASS tokamak into a GAM database to evaluate various scaling laws for the GAM amplitude and frequency. The obtained results together with the calculated GAM damping rate were published in [2]. During international collaboration on the topic of NBI impact on GAM, the author processed the experimental data to support the proposed theoretical model. Obtained results were published in article [3].

Chapter 7

Conclusions and outlook

The author devoted his effort to fast measurement of plasma edge density and research of GAMs. Part I of the thesis clarify the importance of these topics to plasma confinement and its relation to plasma turbulence.

The author processed data from various diagnostic systems available on the COMPASS tokamak as described in Part II of the thesis. Fast edge density measurement was realized by Li-BES diagnostics. The author has spent many days doing a technical work on Li-beam device and doing analysis of Li-BES signal thus the detail description of the Li-BES diagnostics is also presented in Section 3.2.1. In the case of GAM analysis, the author puts together signals from several diagnostic systems into GAMDB which forms a basis for evaluation of GAM scaling. The author evaluated a damping rate for GAM providing explanation of radial extent of GAM and also cooperated with foreign colleagues in the field of NBI impact on GAM.

Part III of the thesis briefly describes results achieved by the author in attached articles (Appendices A.1, A.2, A.3) and describes in more detail results achieved by the author in articles listed in the list of author's publications related to the thesis (Appendix C.1). All presented results was published in impacted journals, namely,

1. Fast density reconstruction algorithm with error estimation for signal from Li-BES diagnostics published in [1] (Appendix A.1).
2. Temporal evolution of electron density published in [7] and ELM averaged electron density at the top of the pedestal published in [5].
3. Extensive study of GAM amplitude and frequency with respect to various plasma parameters and GAM damping rate estimation published in [2] (Appendix A.2).
4. Temporal evolution of GAM amplitude and frequency during NBI heated discharges supporting theoretical predictions published in [3] (Appendix A.3).

There will be a campaign with the aim to reach I-mode on the COMPASS tokamak this year. Both the plasma current and the toroidal magnetic field will be in reversed direction compared to the standard operation. This will

have two consequences: First, NBI will be in counter-current configuration, and therefore a GAM activity should be stronger as can be seen from Fig. 6.3; Second, a grad-B drift of ions will be in direction away from the X-point (unfavorable ∇B configuration), and therefore a chance to reach H-mode will be suppressed. The author will contribute to this experiment with a measurement of plasma edge density profiles and characteristic of density fluctuations as it was done in recently published paper [8]. Moreover GAM signals will be stored to the GAMDB and analysed.

GAMDB can be further developed in the future and may overcome the non-experimental phase of tokamak department during installation of the COMPASS-U tokamak.

COMPASS-U will offer a unique opportunity to study advanced confinement modes, and therefore the author can apply knowledge about GAMs and diagnostic methods of the SOL and edge plasma during research on COMPASS-U tokamak. The author has already analysed possibility of measurement with alkali beam diagnostics on the COMPASS-U tokamak showing that penetration of the beam to the plasma will be in the range of 1-3 cm [12]. Therefore, alkali beam diagnostics will become mostly SOL diagnostics but measurement up to position of maximal density gradient in "low" density regime as I-mode is not precluded.



Appendices



Appendix A

Selected author's publications

■ **A.1 Fast density reconstruction of Li-BES signal on the COMPASS tokamak**

Fast density reconstruction of Li-BES signal on the COMPASS tokamak

J. Krbec,^{1,2,a)} P. Háček,^{1,3} M. Berta,⁴ J. Seidl,¹ M. Hron,¹ and R. Pánek¹

¹*Institute of Plasma Physics of the CAS, Prague, Czech Republic*

²*Faculty of Nuclear Sciences and Physical Engineering, Czech Technical University in Prague, Prague, Czech Republic*

³*Faculty of Mathematics and Physics, Charles University, Prague, Czech Republic*

⁴*Department of Physics and Chemistry, Széchenyi István University, Győr, Hungary*

(Received 26 July 2018; accepted 23 October 2018; published online 9 November 2018)

This article describes a fast and automatic reconstruction of the edge plasma electron density from the radiation of energetic Li atoms of the diagnostic beam on the COMPASS tokamak. Radiation is detected by using a CCD camera and by using an avalanche photo-diode system with a temporal resolution of 20 ms and 2 μ s, respectively. Both systems are equipped with a 670.8 nm optical filter which corresponds to the lithium $1s^2 2s^1 - 1s^2 2p^1$ transition. A theoretical model and a data processing procedure of a raw signal to obtain the density profile are described. The reconstruction algorithm provides the absolutely calibrated electron density profiles together with the measurement error estimated from relatively calibrated light profiles; the implementation is performed in Python. Time demanding operations of the code were optimized to provide reconstruction of a single profile within less than 10 ms which makes the code applicable for processing of a large amount of data. Thanks to this calculation speed, it is possible to reconstruct electron density profiles between two consecutive shots on the COMPASS tokamak with 2 μ s time resolution. *Published by AIP Publishing.* <https://doi.org/10.1063/1.5049894>

I. INTRODUCTION

Understanding of the edge plasma density behavior plays a crucial role in the edge particle transport and Edge Localized Mode (ELM) physics, and it is one of the key research topics of the COMPASS tokamak (Pánek *et al.*, 2006). The machine has ITER-like geometry with a single-null-divertor and clear high confinement mode (H-mode) in the ohmic regime, and its research contributes to the understanding of plasma behavior also on next-step devices like ITER (Pánek *et al.*, 2015). The COMPASS is well equipped with diagnostics focused on the edge plasma (Weinzettl *et al.*, 2011). One of such diagnostics is a Li-beam injector used for Beam Emission Spectroscopy (BES) measurements.

Li-BES is an active spectroscopic method suitable for edge electron density measurement using the line radiation detection of the injected lithium atoms. In the past, this technique was used for radial density profile measurement at the TEXTOR (Pusztai *et al.*, 2009 and Wolfrum *et al.*, 1993) and DIII-D (Thomas, 1995) tokamaks, and nowadays it is used at ASDEX Upgrade (Willensdorfer *et al.*, 2014), JET (Réfy *et al.*, 2018), KSTAR (Lampert *et al.*, 2015), and EAST (Anda *et al.*, 2018 and Zoletnik *et al.*, 2018) tokamaks. The method was also successfully used for a 2D plasma density fluctuation measurement at the Wendelstein 7-AS stellarator (Zoletnik *et al.*, 2005).

The light radiation is detected both by using a CCD camera and by using an Avalanche Photo-Diode (APD) system with a high temporal resolution of 2 μ s on the COMPASS tokamak (Anda *et al.*, 2016 and Berta *et al.*, 2015). The reconstruction of the electron density profile is based on a collisional-radiative

(CR) model which is extended by the absolute calibration method described by Schweinzer (Schweinzer *et al.*, 1992).

A brief overview of BES and the experimental setup of Li-BES diagnostics on the COMPASS tokamak is listed in Secs. IA and IB. Information about the CR model, equation for density reconstruction, and error estimation is summarized in the theoretical part of this article (Sec. II). The reconstruction algorithm implemented in Python is described in Sec. III. In the last section, experimental results from the APD system and execution time of the code are shown. It is important to note that the target of this work was to develop an automatic and fast density reconstruction algorithm for the edge region of the COMPASS tokamak.

A. Description of BES

In general, BES is an active spectroscopic method based on injection of neutral atoms into the plasma. These atoms undergo collisional processes due to interactions with plasma particles. A subsequent spontaneous emission of the excited atoms produces photons which are detected by using an observation system. Plasma parameters can be estimated from the detected light spectrum. The interaction of the beam with plasma can be described by the CR model.

The light signal at different positions along the beam path is correlated, which is a drawback of BES. The finite decay time of the spontaneous emission together with a fast motion of the beam atoms smears the information about plasma density in the light profile. The beam attenuation along the beam path also causes propagation of the information about the plasma density from the beginning of the beam path to its end via the number of neutral lithium atoms which results in anti-correlation of the light signal at the beginning and the end of the light profile.

^{a)}Electronic mail: krbec@ipp.cas.cz

These artificial phenomena must be removed from the light signal by a deconvolution process which results in the reconstructed density (Pietrzyk *et al.*, 1993). A method used on the COMPASS tokamak which is based on Schweinzer algorithm (Schweinzer *et al.*, 1992) is described in Sec. III. The advantage of this method is that an absolutely calibrated light profile is not needed for the reconstruction. It means that information about the transmittance of optical elements, étendue, and beam current in plasma is not required. Compared to the RENATE code (Guszejnov *et al.*, 2012) which is written in an Interactive Data Language (IDL) and performs forward calculation of the light profile, the reconstruction code in Python was developed to make a forward calculation and a reconstruction without using time consuming optimization methods.

B. Experimental setup

An experimental setup is shown in Fig. 1. The detection system is located at the same poloidal cross section as the Li-beam, and it observes the beam injected at the midplane. Lithium atoms are accelerated up to 120 keV and used for BES on the COMPASS tokamak (Anda *et al.*, 2016).

The detection system consists of the CCD camera (640×480 at 50 frames/s) located on the top of the tokamak vessel and the APD system (1×18 at 2 MS/s) suitable for density fluctuation measurement (Berta *et al.*, 2015) located on the bottom of the vessel. Both systems are equipped with optical filters with the central wavelength 670.8 nm, corresponding to a lithium $1s^2 2p^1 \rightarrow 1s^2 2s^1$ transition.

A transition decay time given by the spontaneous decay time (27 ns) and collisional de-excitation processes produce smearing of the information about density over $\Delta z \approx 2$ cm for a 60 keV beam and plasma density $n_e(z) = 3 \times 10^{19} \text{ m}^{-3}$. Due to low temporal resolution of the CCD camera, this article

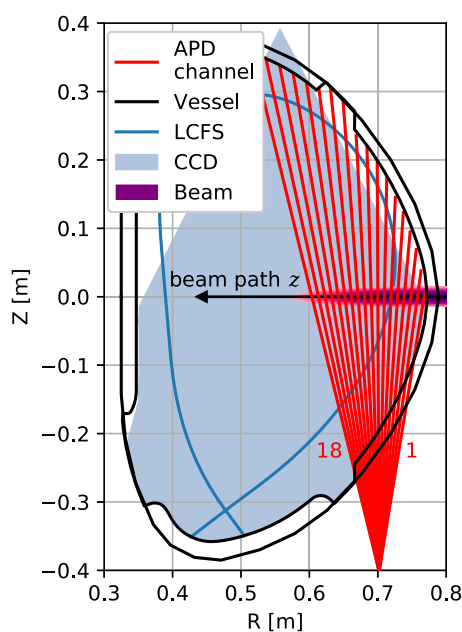


FIG. 1. Poloidal cross section of the COMPASS tokamak vessel with observation system's (18 APDs in one row) lines of sight and last closed flux surface (LCFS) of typical diverted plasma shape.

focuses on processing of the signal from the APD system; therefore, the temporal resolution of the density measurement is given by a beam chopping frequency (on/off modulation of the beam). The maximal chopping frequency is 250 kHz, and the light profile can be obtained both on the raising and decreasing edges of the chopping signal (Fig. 4), and then the maximal temporal resolution is $2 \mu\text{s}$.

II. THEORETICAL MODEL

A. Collisional-radiative model

CR model describes the population of excitation states of lithium atoms during interaction with plasma. The relation for the population of the i th excitation state N_i is given by Eq. (1) where n_e and n_p are the electron and proton densities, respectively, $\langle \sigma_{e,ij} v \rangle$ stands for the rate coefficients (RC) for the electron impact processes from the i th to j th state, $\sigma_{p,ij}$ express the cross section (CS) for proton impact processes from the i th to j th state, $\sigma_{pEL,i}$ is the proton impact electron loss, A_{ij} are the transition probabilities of spontaneous emission from the i th to j th state, $\langle \sigma_{eion,i} v \rangle$ is the rate coefficient for the electron impact ionization, and v_b is the beam velocity,

$$\begin{aligned} \frac{dN_i}{dz} = & \sum_{j,j \neq i} \frac{\langle \sigma_{e,ji} v \rangle}{v_b} n_e N_j - \sum_{j,j \neq i} \frac{\langle \sigma_{e,ij} v \rangle}{v_b} n_e N_i + \sum_{j,j \neq i} \sigma_{p,ji} n_p N_j \\ & - \sum_{j,j \neq i} \sigma_{p,ij} n_p N_i + \sum_{j,j > i} \frac{A_{ji}}{v_b} N_j - \sum_{j,j < i} \frac{A_{ij}}{v_b} N_i \\ & - \frac{\langle \sigma_{eion,i} v \rangle}{v_b} n_e N_i - \sigma_{pEL,i} n_p N_i. \end{aligned} \quad (1)$$

Approximate rate coefficients $\langle \sigma v \rangle$ were used in (1) since $v_p \ll v_b \ll v_e$ [for edge plasma, $v_p(75 - 150 \text{ eV}) = 1.2 - 1.7 \times 10^5 \text{ m/s}$, $v_b(40 - 60 \text{ keV}) = 1.1 - 1.3 \times 10^6 \text{ m/s}$, and $v_e(150 - 300 \text{ eV}) = 0.7 - 1.0 \times 10^7 \text{ m/s}$], the relative velocities are $|v_p - v_b| \approx v_b$ and $|v_e - v_b| \approx v_e$, and the rate coefficients are

$$\langle \sigma_p v \rangle = \sigma(v_p) v_b, \quad \langle \sigma_e v \rangle = \int \sigma(v_e) v_e f(v_e) dv_e,$$

where $f(v_e)$ is the electron velocity distribution function.

The rate coefficient formula for the Maxwell-Boltzmann velocity distribution function of electrons can be found in the work of Bell *et al.*, 1983,

$$\langle \sigma_e v \rangle = \left(\frac{8kT}{\pi m_e} \right)^{\frac{1}{2}} \int_{\frac{E_{Th}}{kT}}^{\infty} \sigma(E) \frac{E}{kT} e^{-\frac{E}{kT}} d\left(\frac{E}{kT} \right), \quad (2)$$

where m_e is the electron mass, E_{Th} is the threshold energy for the corresponding process, and kT is the temperature of the plasma in eV.

The cross section for inelastic collisions of the lithium atoms with electrons and protons was taken from databases (Janev and Smith, 1993; Wutte *et al.*, 1997; and Schweinzer *et al.*, 1999). Cross sections for the downward transition processes are obtained from a detailed balance condition.

B. Density equation

The implemented reconstruction method was described by Schweinzer (Schweinzer *et al.*, 1992). The method is based

on the algebraic rearrangement of the differential equation (1) for the 2p level, obtaining the explicit equation for the density

n_e as a function of the beam coordinate z and all occupation densities N_i ,

$$n_e(z) = \frac{num}{den} \approx \frac{\alpha(Li_{2p}(z+h) - Li_{2p}(z)) - \alpha A_{22} \int_z^{z+h} Li_{2p}(s) ds - h A_{2k} N_k(z)}{\alpha \int_z^{z+h} \sigma_{22}(s) Li_{2p}(s) ds + \int_z^{z+h} \sigma_{2l}(s) ds N_l(z)}, \quad k \equiv j \neq 2, \quad l \equiv j > 2, \quad (3)$$

where $\sigma_{2j} = \sigma_{e,2j} + \sigma_{p,2j}$, h is an integration step,

$$\alpha Li_{2p}(z) = N_2(z),$$

A_{2k} are the Einstein coefficients for spontaneous emission, and α is a calibration constant which is unknown at the beginning of the reconstruction and its initial value can be set arbitrarily. Estimation of n_e comprises simultaneous calculation of (3) together with integration of the system of five ordinary differential equations (1) for 2s, 2p, 3s, 3p, and 3d levels. Inclusion of more bound $Li(nl)$ states with $n \geq 4$ into the calculations has been found unnecessary (Schweitzer *et al.*, 1992).

C. Error estimation theory

Measurement of the radiation along the beam path is performed in M points with a step Δz given by the spatial resolution of the detection system. Each measurement point M corresponds to one APD channel sightline (Fig. 1). The detected light in the j th APD channel depends on densities in all previous channels as described in Sec. I A; thus,

$$Li_{2p}(z_j) = f(n_e(z_1), \dots, n_e(z_j)), \quad j \in M, \quad (4)$$

where $Li_{2p}(z_j)$ is the detected light intensity in the j th channel and $n_e(z_i)$ is the electron density in the i th channel where $i \leq j$ and f represents the CR model.

Dependence of the light signal amplitude on plasma temperature is negligible compared to the density dependence (Pietrzyk *et al.*, 1993). This means that the reconstructed density profiles will only slightly depend on the temperature profiles. A comparison between density profiles reconstructed for the same light profile but for different temperature profiles [either measured by the Thomson scattering diagnostics (Stefanikova *et al.*, 2016) or parabolic, with the same central temperature] is shown in Fig. 2. The relative change in the reconstructed density profile is ≈ 10 times lower than the relative change in temperature profiles; therefore, the region with 50% change in the temperature profile produces only 5% change in the density profile.

Let us denote the light variables at positions z_j with superscript j and the density variables at positions z_i with superscript i , i.e., $Li_{2p}(z_j)$ as Li_{2p}^j and $n_e(z_i)$ as n_e^i . Let us suppose that we are able to determine the standard deviation of a light profile in all channels σ_{Li}^j from the measurement and let us denote the standard deviation of density as $\sigma_{n_e}^i$. Gauss' law of error propagation will hold; thus, the standard deviation of the light signal σ_{Li}^j in the j th channel can be written as follows:

$$(\sigma_{Li}^j)^2 = \sum_{i=1}^j \left| \frac{\partial Li_{2p}^j}{\partial n_e^i} \right|^2 (\sigma_{n_e}^i)^2, \quad (5)$$

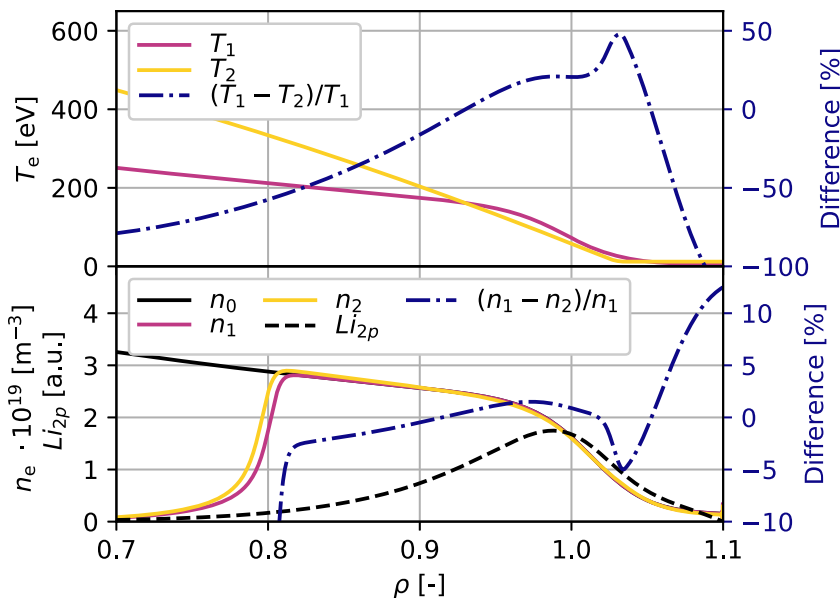


FIG. 2. Sensitivity of the reconstruction algorithm on the temperature profile. COMPASS (Stefanikova *et al.*, 2016) T_1 and parabolic T_2 profiles (top graph) were used for reconstruction of the light profile Li_{2p} obtained from profiles n_0 and T_1 using the CR model. Density profiles n_1 and n_2 correspond to reconstructions with temperature profiles T_1 and T_2 , respectively.

which can be rewritten into the vector form

$$\sigma_{Li}^2 = \mathbb{F} \sigma_{n_e}^2, \quad (6)$$

where the error propagation matrix \mathbb{F} is given by

$$\mathbb{F}_{ji} = \left| \frac{\partial Li_{2p}^j}{\partial n_e^i} \right|^2 \approx \left| \frac{Li_{2p}^j(n_e^i + \delta n_e^i) - Li_{2p}^j(n_e^i)}{\delta n_e^i} \right|^2 \quad (7)$$

$\delta n_e^i \ll n_e^i.$

$\sigma_{n_e}^i$ can be obtained by solving the system of Eq. (6). There are several issues when constructing the \mathbb{F} matrix due to measurements in discrete points. First, the density profile is interpolated to the numerical grid; second, the spatial Gaussian perturbation is added to the density profile; and lastly, the profile is averaged to the measurement points and δn_e^i is estimated. Gaussian perturbation must follow these requirements:

1. perturbation is small enough to fulfill linearization in (7);

2. perturbation is local, i.e., only one density channel is influenced; and
3. the biggest light perturbation is on the same channel as density perturbation.

Otherwise solution (6) will contain negative values for errors.

III. RECONSTRUCTION ALGORITHM

The aim of the reconstruction is to obtain a density profile from a $1s^22s^1-1s^22p^1$ transition radiation profile. The overall reconstruction process which can run automatically is shown in the diagram in Fig. 3.

The reconstruction process can be separated into 4 main phases:

- light profile generation (Sec. III A),
- CS and RC calculation (Sec. III B),
- density reconstruction (Sec. III C), and
- error estimation (Sec. III D).

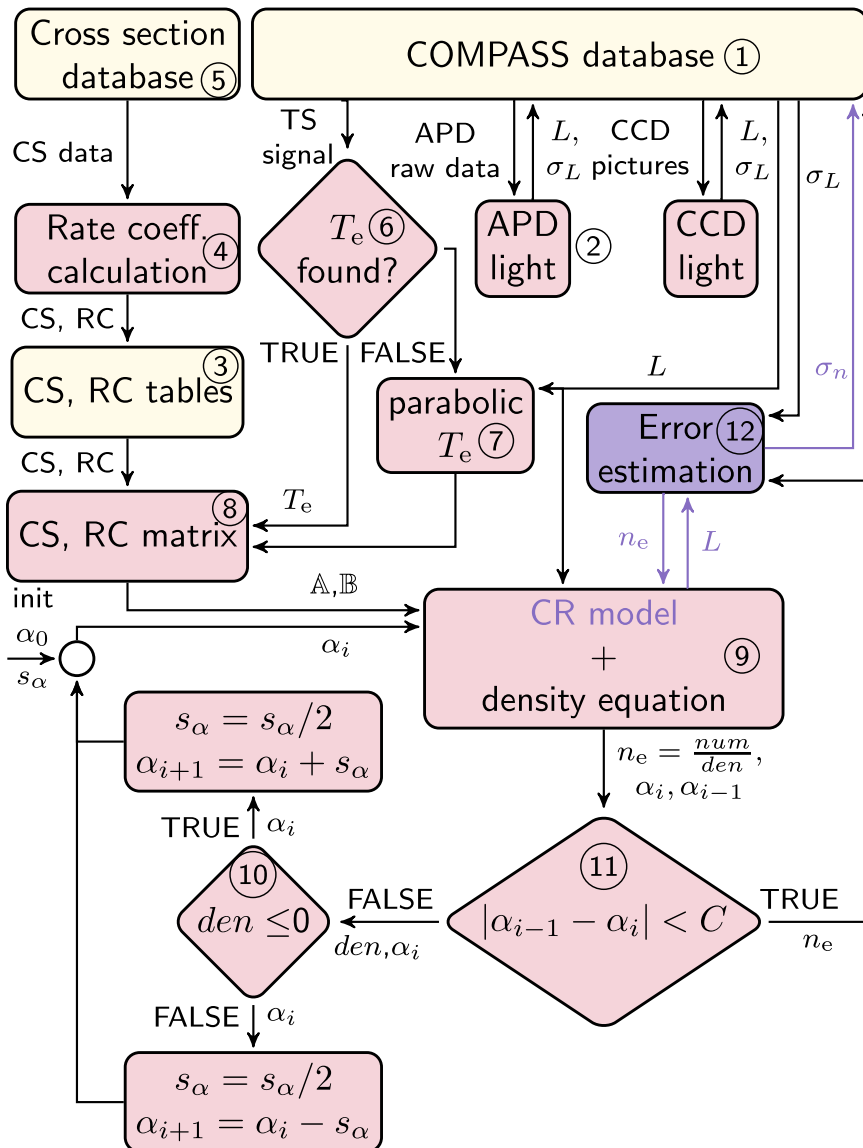


FIG. 3. Automated density reconstruction process. Numbers in the circles serve for referring from the text.

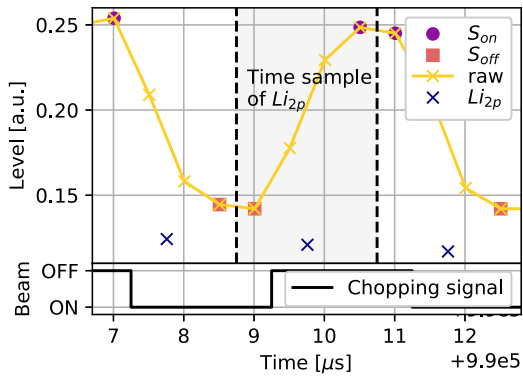


FIG. 4. Time evolution detail of the signal from APD channel 11 in shot #13691 with the 250 kHz chopping signal.

A. Light profile generation

Raw signals from APD and CCD camera are stored in the COMPASS database (CDB) (① in Fig. 3) (Urban *et al.*, 2014). This article will focus on the processing of the APD signal because this detector is the only one relevant for the fast density measurement. CCD camera signal processing is described elsewhere (Anda *et al.*, 2016).

Code “APD light” (② in Fig. 3) reads a raw signal and generates the light profile. The raw signal from APD channel 11 is shown in Fig. 4. At first, the signals with the beam S_{on} and without the beam S_{off} are separated with respect to the chopping frequency. Each time slice is given by the edge in the chopping signal. It results in $2\times$ higher sampling frequency than the chopping frequency. As can be seen in Fig. 4, the lowest temporal resolution is $2\ \mu\text{s}$ which comprises only 1 measurement point in each half-period (a 500 kHz bandwidth of an analog amplifier smears the 2 points on the edge).

Relative calibration of the APD channels and background subtraction is performed on separated signals. Figure 5 shows the APD signal in a neutral gas and in the plasma discharge. The APD signal contains electronic noise S_{el} , background signal S_{bg} , and beam signal S_b .

Part of the discharge with neutral gas is used for the relative calibration. Due to a low ionization rate in neutral gas and the balance of excitation and de-excitation processes along the beam path, a constant signal is expected on all channels. Then a normalized calibration coefficient a_j for channel j is given

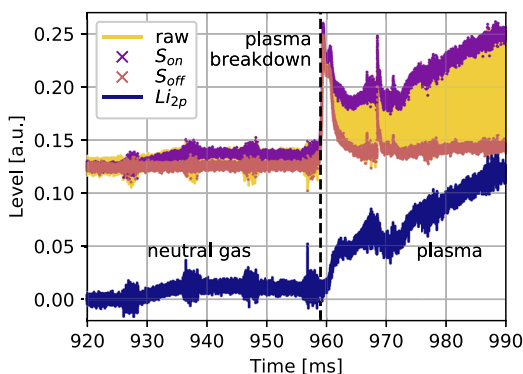


FIG. 5. Time evolution of the signal from APD channel 11 in shot #13691 with the 250 kHz chopping signal.

by

$$a_j = \frac{S_{g,on}^j - S_{g,off}^j}{S_{g,on}^{ref} - S_{g,off}^{ref}}, \quad j \in M, \quad j \neq ref, \quad (8)$$

$$a_j = 1, \quad j = ref,$$

where $S_{g,on}^j = S_{el}^j + S_b^j$ and $S_{g,off}^j = S_{el}^j$ are the signals in the neutral gas when the beam is on and off, respectively, and ref denotes the reference channel (typically with the largest signal). The coefficients a_j include the filter transmission, amplification of the channel, and signal attenuation caused by geometrical reasons.

After the calibration, the light profiles Li_{2p}^j are generated from the APD signal during the plasma discharge,

$$Li_{2p}^j = \frac{S_{p,on} - S_{p,off}}{a_j}, \quad (9)$$

where $S_{p,on}^j = S_{el}^j + S_{bg}^j + S_b^j$ and $S_{p,off}^j = S_{el}^j + S_{bg}^j$ are the signals during plasma discharge when the beam is on and off, respectively.

Calibration coefficients are a dominant source of the light signal error σ_{Li} which is stored in CDB since photon rates are $\approx 10^{4-5}$ ph/ μs on the COMPASS tokamak (Berta *et al.*, 2015).

B. Cross section and rate coefficients

CS and RC tables (③ in Fig. 3) were pre-calculated (④ in Fig. 3) for a wide range of energies and electron temperatures based on CS fitting coefficients from the literature (Janev and Smith, 1993; Wutte *et al.*, 1997; and Schweinzer *et al.*, 1999) (⑤ in Fig. 3). Before the reconstruction, CS and RC are interpolated from these tables according to the temperature profile and beam energy in each shot.

The temperature profile is obtained from Thomson scattering (TS) diagnostics (⑥ in Fig. 3). In a case where the TS profile is not available, a parabolic profile is used instead of it (⑦ in Fig. 3). The error in the temperature profile is negligible because of low dependence of the reconstructed density on the temperature profile, see Fig. 2, as noted above.

The collisional matrix \mathbb{A} (3D, i.e., path dependent) and spontaneous transition matrix \mathbb{B} (2D—constant along the beam path) are used in the reconstruction algorithm (⑧ in Fig. 3).

C. Reconstruction algorithm

The system of differential equations (1) can be rewritten into the matrix notation

$$\frac{dN}{dz} = (\mathbb{A}(z)n_e(z) + \mathbb{B})N \quad (10)$$

and solved by the four-step Adams-Bashforth method (Butcher, 2016). Integration in (3) is performed by Boole’s rule method. Both Eqs. (10) and (3) are solved simultaneously (⑨ in Fig. 3) with an initial condition $N(z=0) = [1\ 0\ 0\ 0\ 0]^T$ for Li states with $n = 2, 3$ and $n_e(z=0) = 0$ for density where $z = 0$ is the position of a tokamak vessel. After each run, the α constant is changed by step s_α to fulfill a requirement that the numerator and denominator of (3) change sign at the same z coordinate (⑩ in Fig. 3) and the result is positive everywhere. A bisection method is used to find correct α ; therefore, the

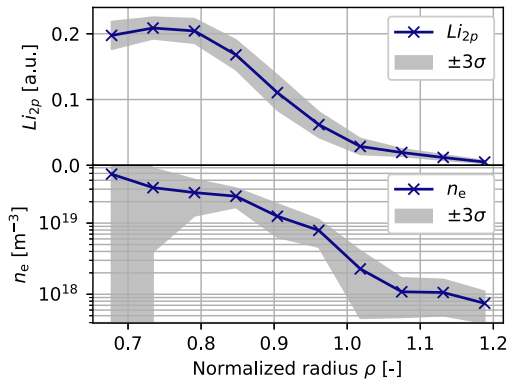


FIG. 6. Light and density profiles with measurement uncertainty from shot #13691 ($t = 1009$ ms) with $2 \mu\text{s}$ temporal resolution.

initial estimate of α_0 and s_α must cover the expected value of α . The reconstruction stops when the relative change in α is smaller than the given constant C (① in Fig. 3).

An integration step h has to be much smaller than the distance between measurement points in order to have the convergent reconstruction scheme. Measurement points are interpolated to a numerical grid using cubic splines. The reconstructed density profile is then averaged to the measurement grid. Figure 6 depicts one reconstruction profile with the reconstruction error.

D. Error estimation

The error estimation code (② in Fig. 3) reads the measurement uncertainty of the light profile from CDB (① in Fig. 3) and gets the density profile from the reconstruction code. Small density perturbations δn_e^i are applied channel by channel to the density profile, and the profile is interpolated to the numerical grid. The CR model is used for forward calculation of the perturbed light profile. The average value of the light signal is calculated for each of the channels. The difference between the perturbed light profile and the measured light profiles gives information about light perturbation δLi_{2p}^i , and the error propagation matrix \mathbb{F} is calculated using Eq. (7). The measurement uncertainty of the density profile σ_{n_e} is obtained from Eq. (6). Light and density profiles with the measurement uncertainty are shown in Fig. 6.

The error of the density profile accumulates toward the center of the plasma because information about density propagates along the beam path. The maximal value is reached just behind the maximum of the light profile at a position where the light profile is insensitive to the density variation. The response of the light profile to the small positive change in the density is positive in the rising part of the light profile and negative in the decreasing part of the light profile. Somewhere between must be the point where the light signal is insensitive to density perturbation.

Compared to the probabilistic reconstruction technique (Fischer *et al.*, 2008), there is no straightforward method on how to add the constraints on the density profile from other diagnostics, e.g., Thomson scattering, to minimize the density error. Any kind of the optimization technique will decrease the speed of the reconstruction algorithm.

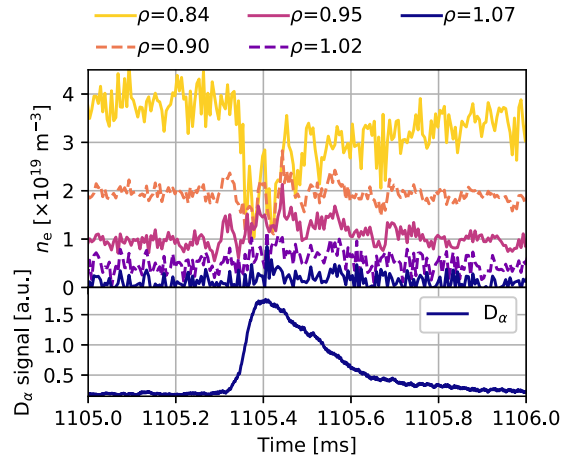


FIG. 7. A time evolution of the density profile during ELM event with a temporal resolution of $2 \mu\text{s}$ (shot #17271). The APD channel position is mapped to normalized radius ρ .

IV. RESULTS

A. Reconstructed density

Temporal evolution of the electron density profile during one Edge Localized Mode (ELM) event measured with $2 \mu\text{s}$ temporal resolution is shown in Fig. 7.

One can see a decrease in density on the inner channel ($\rho = 0.84$) and an increase in density on the outer channels ($\rho = 0.90$ and 0.95) together with the density oscillations (D_α signal has been added to Fig. 7 as a reference for density reconstruction during the ELM period).

B. Reconstruction execution time

The reconstruction algorithm was written in Python in order to reduce execution time and simplify the implementation into CDB post-processing routines (CDB is also implemented in Python).

Since the APD detector produces up to 10^6 light profiles during each plasma discharge, there is an urgent need for a fast reconstruction algorithm. Different implementations of a core section of the reconstruction algorithm were compared with respect to the execution time; see Table I. It can be seen that the Python code with Numba compiler gives satisfactory results. The code consists of loops with simple numerical operations available in the Numba environment. Several modifications were performed: Numba removal, vectorization (vect.), i.e., more profiles are processed simultaneously in one processor core, and parallelization to 3 processor cores (par.); thus, the whole reconstruction procedure was able to get below 10 ms

TABLE I. Execution time of one reconstruction for different code implementations at Intel Core i5-4460 CPU at 3.20 GHz with 88 GFLOPs.^a

Language	Execution time (s)	%
Python	1.888	100.0
Python + Numba	0.104	5.5
Python + vect.	0.018	1.0
Python + vect. + par.	0.009	0.5

^aBenchmarked by LINPACK.

for one profile, and it takes about 16 min to process 10^6 light profiles, and this fact gives us a possibility to reconstruct density profiles with time resolution equal to $2 \mu\text{s}$ on a shot to shot basis.

Although the code is quite fast, it will not run on a real-time (RT) system because the MicroPython library set is limited and some libraries used in the code are missing, e.g., Numpy. Concerning the memory requirements, the 3D array \mathbb{A} is quite large; thus, a stepwise temperature profile would be required to reduce its size. Moreover this array is obtained using the time-consuming interpolation of rate-coefficients; thus, the predefined temperature profile before the shot would be required. Finally, the present hardware setup is not ready to provide a signal from APD to the RT system.

C. Automation of the reconstruction

The light profiles are calculated within several seconds immediately after the shot. When the light profile is stored in the CDB, the density reconstruction can start. A 300 ms long shot can be reconstructed with $2 \mu\text{s}$ time resolution within 16 min or with $150 \mu\text{s}$ resolution within few seconds, i.e., before the next shot (interval between shots on the COMPASS tokamak is typically 15 min). Density uncertainty estimation is calculated when density profiles are ready for the whole shot.

V. CONCLUSION

This article describes in detail the fast ($2 \mu\text{s}$) automatic density reconstruction process from the Li-BES signal on the COMPASS tokamak. It is shown that the presented reconstruction process is suitable for routine measurements producing a large amount of data, i.e., diagnostics with high temporal resolution. This is also the case of the COMPASS tokamak where the Li-BES diagnostics focuses on density fluctuations and transition events, as shown reconstructed in Fig. 7. The implementation in the Python language together with compilation of core parts with Numba decreases the requirements for computational time by one order of magnitude compared to MATLAB. We were able to get under 10 ms execution time for one reconstruction with further optimization of the code. There is still space for improvements by using Nvidia's CUDA parallel computation.

ACKNOWLEDGMENTS



This work was supported by the grants of Czech Science Foundation No. GA16-25074S and co-funded by MEYS

Project Nos. 8D15001 and LM2015045. This work was also supported by the Grant Agency of Czech Technical University in Prague, under Grant No. SGS17/138/OHK4/2T/14.

- Anda, G., Bencze, A., Berta, M., Dunai, D., Hacek, P., Krbec, J., Réfy, D., Krizsanóczy, T., Bató, S., Ilkei, T. et al., *Fusion Eng. Des.* **108**, 1 (2016).
- Anda, G., Dunai, D., Lampert, M., Krizsanóczy, T., Németh, J., Bató, S., Nam, Y., Hu, G., and Zoletnik, S., *Rev. Sci. Instrum.* **89**, 013503 (2018).
- Bell, K., Gilbody, H., Hughes, J., Kingston, A., and Smith, F., *J. Phys. Chem. Ref. Data* **12**, 891 (1983).
- Berta, M., Anda, G., Bencze, A., Dunai, D., Háček, P., Hron, M., Kovácsik, A., Krbec, J., Pánek, R., Réfy, D. et al., *Fusion Eng. Des.* **96**, 795 (2015).
- Butcher, J. C., *Numerical Methods for Ordinary Differential Equations* (John Wiley & Sons, 2016).
- Fischer, R., Wolfrum, E., Schweinzer, J. et al., *Plasma Phys. Controlled Fusion* **50**, 085009 (2008).
- Guszejnov, D., Pokol, G., Pusztai, I., Refy, D., Zoletnik, S., Lampert, M., and Nam, Y., *Rev. Sci. Instrum.* **83**, 113501 (2012).
- Janev, R. K. and Smith, J., *Atomic and Plasma-Material Interaction Data for Fusion* (IAEA Report, 1993), Vol. 4.
- Lampert, M., Anda, G., Czopf, A., Erdei, G., Guszejnov, D., Kovácsik, Á., Pokol, G., Réfy, D., Nam, Y., and Zoletnik, S., *Rev. Sci. Instrum.* **86**, 073501 (2015).
- Pánek, R., Adámek, J., Aftanas, M., Bílková, P., Böhm, P., Brochard, F., Cahyna, P., Cavalier, J., Dejarnac, R., Dimitrova, M. et al., *Plasma Phys. Controlled Fusion* **58**, 014015 (2015).
- Pánek, R., Bilyková, O., Fuchs, V., Hron, M., Chráska, P., Pavlo, P., Stöckel, J., Urban, J., Weinzettl, V., Zajac, J. et al., *Czech J. Phys.* **56**, B125 (2006).
- Pietrzyk, Z., Breger, P., and Summers, D., *Plasma Phys. Controlled Fusion* **35**, 1725 (1993).
- Pusztai, I., Pokol, G., Dunai, D., Réfy, D., Pór, G., Anda, G., Zoletnik, S., and Schweinzer, J., *Rev. Sci. Instrum.* **80**, 083502 (2009).
- Réfy, D., Brix, M., Gomes, R., Tál, B., Zoletnik, S., Dunai, D., Kocsis, G., Kálvin, S., Szabolcs, T., and JET Contributors, *Rev. Sci. Instrum.* **89**, 043509 (2018).
- Schweinzer, J., Brandenburg, R., Bray, I., Hoekstra, R., Aumayr, F., Janev, R., and Winter, H., *At. Data Nucl. Data Tables* **72**, 239 (1999).
- Schweinzer, J., Wolfrum, E., Aumayr, F., Pockl, M., Winter, H., Schorn, R., Hintz, E., and Unterreiter, A., *Plasma Phys. Controlled Fusion* **34**, 1173 (1992).
- Stefanikova, E., Peterka, M., Bohm, P., Bilkova, P., Aftanas, M., Sos, M., Urban, J., Hron, M., and Panek, R., *Rev. Sci. Instrum.* **87**, 11E536 (2016).
- Thomas, D., *Rev. Sci. Instrum.* **66**, 806 (1995).
- Urban, J., Pipek, J., Hron, M., Janky, F., Papřok, R., Peterka, M., and Duarte, A., *Fusion Eng. Des.* **89**, 712 (2014).
- Weinzettl, V., Panek, R., Hron, M., Stockel, J., Zacek, F., Havlicek, J., Bilkova, P., Naydenkova, D., Hacek, P., Zajac, J. et al., *Fusion Eng. Des.* **86**, 1227 (2011).
- Willensdorfer, M., Birkenmeier, G., Fischer, R., Laggner, F., Wolfrum, E., Veres, G., Aumayr, F., Carralero, D., Guimarães, L., Kurzan, B. et al., *Plasma Phys. Controlled Fusion* **56**, 025008 (2014).
- Wolfrum, E., Aumayr, F., Wutte, D., Winter, H., Hintz, E., Rusbüldt, D., and Schorn, R., *Rev. Sci. Instrum.* **64**, 2285 (1993).
- Wutte, D., Janev, R., Aumayr, F., Schneider, M., Schweinzer, J., Smith, J., and Winter, H., *At. Data Nucl. Data Tables* **65**, 155 (1997).
- Zoletnik, S., Hu, G., Tál, B., Dunai, D., Anda, G., Asztalos, O., Pokol, G., Kálvin, S., Németh, J., and Krizsanóczy, T., *Rev. Sci. Instrum.* **89**, 063503 (2018).
- Zoletnik, S., Petravich, G., Bencze, A., Berta, M., Fiedler, S., McCormick, K., and Schweinzer, J., *Rev. Sci. Instrum.* **76**, 073504 (2005).

■ **A.2 Electromagnetic characteristics of geodesic acoustic mode in the COMPASS tokamak**

Electromagnetic characteristics of geodesic acoustic mode in the COMPASS tokamak

J. Seidl¹, J. Krbec^{1,2} , M. Hron¹, J. Adamek¹, C. Hidalgo³, T. Markovic^{1,4}, A.V. Melnikov^{5,6}, J. Stockel¹, V. Weinzettl¹, M. Aftanas¹, P. Bilkova¹, O. Bogar^{1,7}, P. Bohm¹, L.G. Eliseev⁵, P. Hacek^{1,4}, J. Havlicek¹, J. Horacek¹ , M. Imrisek^{1,4}, K. Kovarik^{1,4}, K. Mitosinkova^{1,4}, R. Panek¹, M. Tomes^{1,4} and P. Vondracek^{1,4}

¹ Institute of Plasma Physics, The Czech Academy of Sciences, Prague, Czech Republic

² Faculty of Nuclear Sciences and Physical Engineering, Czech Technical University in Prague, Prague, Czech Republic

³ Laboratorio Nacional de Fusión, CIEMAT, Madrid, Spain

⁴ Faculty of Mathematics and Physics, Charles University, Prague, Czech Republic

⁵ National Research Centre 'Kurchatov Institute', Moscow, Russian Federation

⁶ National Research Nuclear University MEPhI, Moscow, Russian Federation

⁷ Faculty of Mathematics, Physics and Informatics, Comenius University, Bratislava, Slovakia

E-mail: seidl@ipp.cas.cz

Received 17 January 2017, revised 14 August 2017

Accepted for publication 31 August 2017

Published 13 October 2017



Abstract

Axisymmetric geodesic acoustic mode (GAM) oscillations of the magnetic field, plasma potential and electron temperature have been identified on the COMPASS tokamak. This work brings an overview of their electromagnetic properties studied by multi-pin reciprocating probes and magnetic diagnostics. The $n = 0$ fluctuations form a continuous spectrum in limited plasmas but change to a single dominant peak in diverted configuration. At the edge of diverted plasmas the mode exhibits a non-local structure with a constant frequency over a radial extent of at least several centimeters. Nevertheless, the frequency still reacts on temporal changes of plasma temperature caused by an auxiliary NBI heating as well as those induced by periodic sawtooth crashes. Radial wavelength of the mode is found to be about 1–4 cm, with values larger for the plasma potential than for the electron temperature. The mode propagates radially outward and its radial structure induces oscillations of a poloidal $E \times B$ velocity, that can locally reach the level of the mean poloidal flow. Bicoherence analysis confirms a non-linear interaction of GAM with a broadband ambient turbulence. The mode exhibits strong axisymmetric magnetic oscillations that are studied both in the poloidal and radial components of the magnetic field. Their poloidal standing-wave structure was confirmed and described for the first time in diverted plasmas. In limited plasmas their amplitude scales with safety factor. Strong suppression of the magnetic GAM component, and possibly of GAM itself, is observed during co-current but not counter-current NBI.

Keywords: geodesic acoustic mode, tokamak, turbulence, COMPASS

(Some figures may appear in colour only in the online journal)

1. Introduction

Geodesic acoustic mode (GAM) [1] is a high-frequency oscillatory branch of zonal flows (ZFs) [2]. The zonal flows are turbulence-driven sheared poloidal flows which can play an important role in self-regulation of turbulent transport. By causing shear decorrelation of turbulent structures [3] ZFs

contribute to establishing a saturated level of the turbulence and the energy transfer from turbulence to ZFs is believed to be an important part of the dynamics of the L-mode to H-mode (L-H) transition [4, 5] or I-mode [6].

As a kind of ZFs, GAM forms a toroidally symmetric ($n = 0$) oscillating poloidal flow with the plasma potential approximately constant on a flux surface ($m_\phi \approx 0$) and with

a finite radial wave number k_r . Due to a geodesic curvature the flow couples to the $m_p = 1$ pressure perturbation with a standing wave pattern. Temperature oscillations associated with GAM have been reported as well [7]. The evidence of the finite radial wave number for GAM was reported e.g. in [8–10].

GAM oscillations are driven by a non-linear three-wave coupling with ambient turbulent oscillations [2], but can be destabilized also by an interaction with fast ions [11–13]. In practice, the non-linear coupling to turbulence is detected using bicoherence analysis [10, 14, 15]. Even though GAM is mainly an electrostatic mode, it can still generate a detectable perturbation of the magnetic field. The magnetic component has been recently described both in the theory [16–19] and experiment [7, 20–22]. While in circular plasmas the magnetic component has a standing wave structure with the poloidal mode number $m_B = 2$ [16, 20, 21], other Fourier components can be induced by plasma shaping [16] or due to mesoscale radial structure of the mode [20, 21].

Frequency of the mode in circular plasmas has been first derived in [1]. It scales with the ion sound speed c_s , the tokamak major radius R_0 and the safety factor q as

$$2\pi f_{\text{GAM}} = (2 + q^{-2})^{1/2} c_s / R_0. \quad (1)$$

Here $c_s = \sqrt{(T_e + \gamma_i T_i) / m_i}$, T_e and T_i is the electron and ion temperature, respectively, m_i is the ion mass and γ_i is the ion specific heat ratio. However, experiments in the non-circular plasmas [23, 24] have shown GAM frequency lower than that predicted by the scaling (1), which led to the development of theoretical [16, 25, 26] and heuristic [23] scalings that incorporate also other geometrical factors, mainly the plasma boundary elongation κ_b . The frequency can change also due to the interaction with fast ions, in which case it often exhibits a chirping character [11, 12].

While the frequency smoothly changes over the plasma radius on some devices [10, 27], following the radial profile of c_s , other machines report one or more GAM non-local eigenmodes with the frequency forming radially localized plateaus of a constant value [8, 20, 23]. There are also reports of a global GAM eigenmode covering the whole plasma extent with a constant GAM frequency [28].

The non-local eigenmode structure of GAM can form when the GAM continuum has a maximum, e.g. due to reversed shear configuration [11] or presence of fast ions [29], but the radial structure of the mode can be influenced also by other factors such as β -coupling of poloidal harmonics [29]. GAM eigenmode radially propagating to the region with lower GAM frequency can also arise when finite gyroradius effects are taken into account [30]. Moreover, similarly to the $m_B = 2$ magnetic halo, strong global $m = 2$ perturbation of the pressure, density and poloidal flow was derived for the continuum GAM in [16].

In this paper, we present observation of GAM oscillations in diverted deuterium discharges on the COMPASS tokamak. The mode is detected in a form of long range correlations of plasma potential between pair of reciprocating probes and in a form of axisymmetric oscillations of poloidal and radial magnetic field.

Several interesting properties of the mode are shown, such as: (i) poloidal structure of a magnetic halo of the mode in diverted plasmas measured simultaneously in B_p and B_r components of the field, showing shift between the components in the poloidal angle, approximately by $\pi/2$ as predicted in [16], and distortion compared to an ideal $m_B = 2$ structure. (ii) Amplitude of the magnetic fluctuations in limited plasmas increases with safety factor, transition from a broad to a narrow spectrum of fluctuations is observed at high plasma shaping. (iii) Temperature oscillations at GAM frequency are detected, their radial propagation speed and radial wave number is different from that of the plasma potential. (iv) Injection of a co-current (but not counter-current) neutral beam suppresses the mode existing in ohmic plasma.

The article is organized as follows. In section 2 we begin with description of the used experimental setup. In section 3 we identify GAM oscillations in COMPASS plasmas and describe their properties. Namely, section 3.1 presents spectra of the measured signals, frequency of GAM and its temperature scaling are discussed in section 3.2, poloidal and radial structure of the mode is described in sections 3.3 and 3.4, respectively, and section 3.5 confirms the non-linear interaction between GAM and the ambient turbulence (AT). In section 4 we present initial observations of change of GAM amplitude in dependence on the direction of NBI. Finally, a brief summary is given in section 5.

2. Experimental setup

COMPASS ($R = 0.56$ m, $a = 0.2$ m) is a tokamak with an ITER-like plasma configuration, plasma current $I_p < 400$ kA, toroidal magnetic field $B_T < 2.1$ T and boundary elongation $\kappa_b \leq 1.85$ [31]. Auxiliary plasma heating is available using two NBI beams (40 keV) with a power of 350 kW each.

This study focuses mainly on diverted L-mode plasmas, where the presence of GAM has been confirmed in most of the available discharges and the mode is well accessible by both the probe and magnetic diagnostics. GAM presence has been confirmed also in limited discharges, but since in this case the mode is localized deeper in the plasma, further from the last closed flux surface (LCFS), the current database of deep probe plunges usable for the analysis of the mode is sparse and mainly magnetic data were used.

Figure 1(a) shows an example of a typical shape of plasmas analyzed in this work. All of the discharges had similar boundary elongation $\kappa_b \approx 1.8$ and the toroidal magnetic field $B_T = 1.15$ T. The lower and upper triangularity δ_l and δ_u , respectively, were linearly coupled to the elongation as $\delta_l \approx 0.56\kappa_b - 0.5$ and $\delta_u \approx 0.35\kappa_b - 0.3$. Unless noted otherwise, purely ohmic heating was used.

2.1. Probe diagnostics

COMPASS is equipped with two pneumatic reciprocating probe manipulators that can be used to detect electrostatic fluctuations associated with GAM. The manipulators are located at the top of the vessel and at the low-field side (LFS) mid-plane (figure 1(a)), toroidally shifted by 22.5° (figure 1(b)).

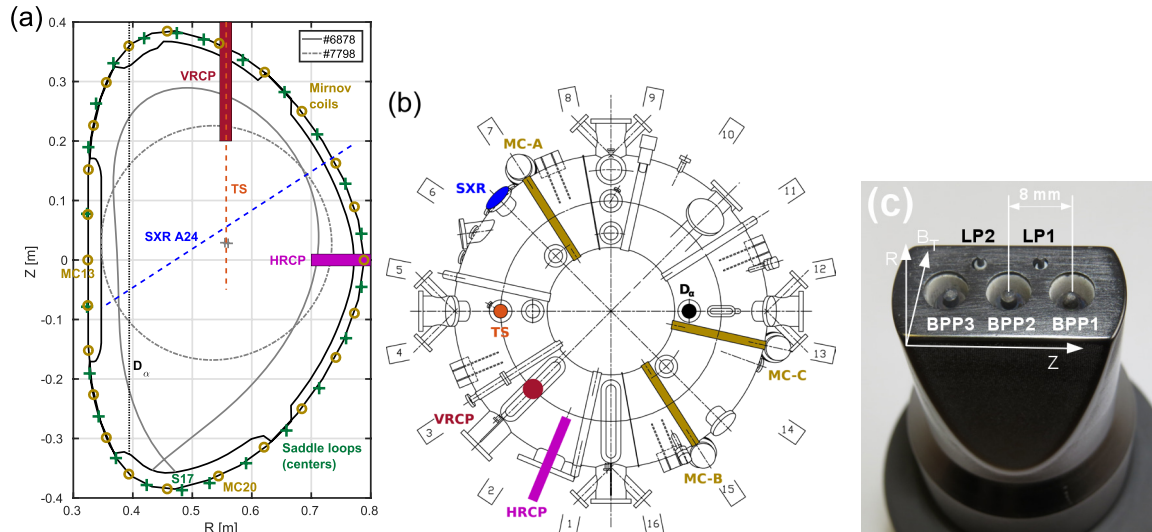


Figure 1. (a) Poloidal cross-section of the COMPASS tokamak showing layout of the used diagnostics together with a typical shape of the analyzed diverted and limited plasmas. (b) Top view of the tokamak with toroidal positions of the diagnostics. (c) Layout of probes on the horizontal probe head.

In the analyzed plasmas the manipulators were not directly connected by magnetic field lines. Schematic picture of the standard probe head used on the horizontal reciprocating manipulator (HRCP) is plotted in figure 1(c). It consists of several ball-pen probes (BPP) and Langmuir probes (LP) that are used to measure the floating potential of the BPP V_{BPP} , the floating potential of the LP V_{fl} and the ion saturation current I_{sat} , all with 5 MHz sampling rate. The potentials are measured on both manipulators but the I_{sat} only at the midplane. Since V_{BPP} is influenced by the electron temperature T_e much less than V_{fl} , as $V_{\text{BPP}} \approx \phi - 0.7T_e$ [32, 33], we use it as a close proxy to the real plasma potential.

The available combination of LPs and BPPs allows also estimation of local electron temperature T_e and its fluctuations using the formula [33]:

$$T_e = (V_{\text{BPP}} - V_{\text{fl}}) / 2.2. \quad (2)$$

In practice, the T_e measurement is limited by an incident heat flux on the Langmuir pin that can, in deeper parts of the plasma, cause LP self-emission [34]. In such a case the T_e measurement is lost but the self-emitting LP can be used as a cross-verification of the potential measurement by the BPP as $V_{\text{BPP}} \approx V_{\text{fl, self-emit}} \approx \phi - 0.7T_e$ [33, 35].

Since BPP and LP are shifted poloidally by 4 mm, there is a risk that the temperature fluctuations could be dominated by an artificial phase-shift arising due to the non-locality of the measurement. Therefore, the temperature is evaluated from an average potential $(\text{BPP1} + \text{BPP2})/2$ that represents potential of a virtual BPP that is located at the poloidal position of the LP. This mitigates part of the phase-shift caused by the low- k_p part of the poloidal wave number spectra. The high- k_p does not seem to significantly contribute to the T_e fluctuations at the GAM frequency because of the strong poloidal flow of several km s^{-1} , which can advect small-scale structures between the probes on a time scale of several μs . This time scale is much shorter than the GAM period and such fluctuations, possibly

affected by the artificial phase shift, are thus filtered out when the T_e signal is band-pass filtered around the GAM frequency.

Both manipulators are able to reciprocate inside the last closed flux surface without overheating of the probe head. However, the position of the probes is not in a full agreement with the LCFS determined by an EFIT reconstruction. A typical shift at the LFS midplane is less than 1 cm in the circular plasmas but of about 2 cm in the diverted ones. As both probes can provide measurement of the local T_e , we therefore carry out magnetic surface labeling, that is necessary for a comparison of the data at the two poloidal positions, using an assumption that T_e is constant over flux surface. This is justified by a short distance along field line between both poloidal positions, which is comparable or smaller than the electron mean free path in the edge, allowing for a fast energy exchange between the two positions. It is also supported by a reasonable match between the temperature profiles when an EFIT correction is applied [33]. Nevertheless, an influence of possible poloidal asymmetries in the plasma edge on the surface labeling using T_e cannot be fully excluded.

Since a direct measurement of the plasma potential is available, we use it for radial localization of the measurements with respect to the radius of a zero radial electric field $R_{E_r=0}$. At the LFS midplane the radius is defined as a position where $E_r = -\partial\langle\phi\rangle/\partial r \approx -\partial\langle\phi\rangle/\partial R = 0$ and a similar definition is used for the vertical position $Z_{E_r=0}$. This reference point, that marks location of the edge sheared poloidal flows, can be directly measured by the probes in any ohmic or L-mode discharge with a sufficiently deep probe plunge. Here, $\langle\cdot\rangle$ represents a radial profile computed either by bin-averaging or by low-pass filtering of the original 5 MHz data by higher-order Butterworth filter with 200 Hz cut-off frequency. Such cut-off frequency is high enough not to distort the profiles due to the radial movement of the probe with velocity $v_{\text{tcp}} \approx 0.5\text{--}1 \text{ m}\cdot\text{s}^{-1}$ and at the same time low enough to remove an influence of sawtooth oscillations that in ohmic

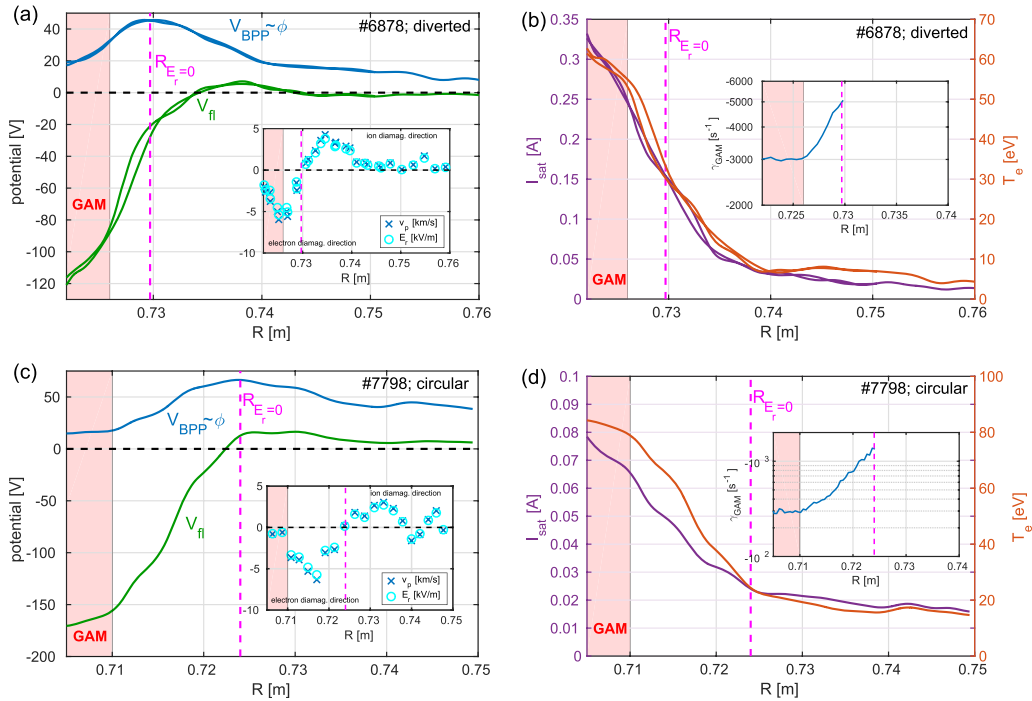


Figure 2. Radial profile of the mean plasma potential ϕ and floating potential V_{fi} , in diverted (a) and limited circular (c) plasmas. Radial profile of the mean ion saturation current I_{sat} and electron temperature T_e in diverted (b) and limited (d) plasmas. Measured by HRCF at the LFS midplane. The inset plots in (a) and (c) show radial profile of the radial electric field E_r and radial profile of the mean poloidal $E \times B$ velocity $\langle v_p \rangle$. The inset plots in (b) and (d) show radial profile of a combined Landau and collisional damping evaluated from the data. Dashed magenta line marks position $R_{E_r=0}$. Data from #6878 are plotted for both directions of probe movement (inward and outward). Pink area marks radial location of GAM oscillations visible in the potential power spectra.

discharges appear at frequencies above 300 Hz and may temporarily change edge plasma parameters.

Typical radial profiles of $\langle \phi \rangle$, $\langle V_{fi} \rangle$ and $\langle E_r \rangle$ measured by the HRCF in the SOL of diverted and circular plasmas are shown in figure 2. One can readily see a significant difference between the plasma potential approximated by V_{BPP} and the floating potential of a Langmuir probe V_{fi} . The difference is proportional to the local electron temperature (equation (2), figures 2(b) and (d)). Local maximum of V_{BPP} defines the reference radius $R_{E_r=0}$ with $E_r = 0$ and thus the place of reversal of the direction of a poloidal $E \times B$ flow $\langle v_p \rangle = -(\partial \langle \phi \rangle / \partial r) / B$. In the analyzed discharges the maximum magnitude of the mean poloidal flow typically reached 5–6 km s⁻¹, with the maximum located inside $R_{E_r=0}$. The absolute value of poloidal shearing rate $\omega_{E \times B} = \partial \langle v_p \rangle / \partial r$ on the other hand peaked typically at or very close to the position $R_{E_r=0}$.

Since V_{fi} drops at the position of the GAM mode to very low values ($V_{fi} < -100$ V), biasing voltage of the LP used for I_{sat} measurement was adjusted appropriately to $V_{bias} = -270$ V $\ll V_{fi}$.

Figures 2(b) and (d) show that the radial I_{sat} and T_e profiles are steepened around the position of $R_{E_r=0}$ radius, and they flatten in the SOL. This is consistent with the definition of near and far SOL [36]. Another flattening of the temperature profiles is observed in the plasma, inside the $E_r = 0$ radius. This indicates that the profile steepening may be linked to the presence of the velocity shear layer around $R_{E_r=0}$ and possibly

also to the presence of the LCFS in this region. Even though the hypothesis $R_{E_r=0} \approx R_{LCFS}$ could not be directly verified on COMPASS, similar BPP measurements on ASDEX Upgrade show good correspondence of both locations [37] and good agreement has been found also in stellarators [38]. Therefore, since the position of $R_{E_r=0}$ is measured simultaneously with the analyzed data by the same diagnostics, it is used as a reliable reference point and as a proxy for the position of the LCFS. The question of a precise localization of the LCFS with respect to the velocity shear layer in COMPASS plasmas is left open for a further study.

2.2. Magnetic diagnostics

COMPASS is equipped with three poloidal rings of magnetic Mirnov coils (MC) labeled MC-A, MC-B and MC-C, each capable of measuring all three components of the magnetic field. Their poloidal coverage is shown in figure 1(a) and toroidal positioning in figure 1(b). In order to detect magnetic fluctuations associated with GAM, the probe diagnostics was supplemented by measurement of fluctuations of poloidal (tangential to the first wall) and radial (normal to the first wall) components of magnetic field B_p and B_r , respectively, with 2 MHz sampling rate along the full poloidal cross-section.

Moreover, a set of saddle loops, that are divided into four toroidal quadrants and poloidally cover most of the vessel (see figure 1(a) and [39]), was used for measurement of axisymmetric $n = 0$ part of B_r fluctuations at 24 poloidal positions.

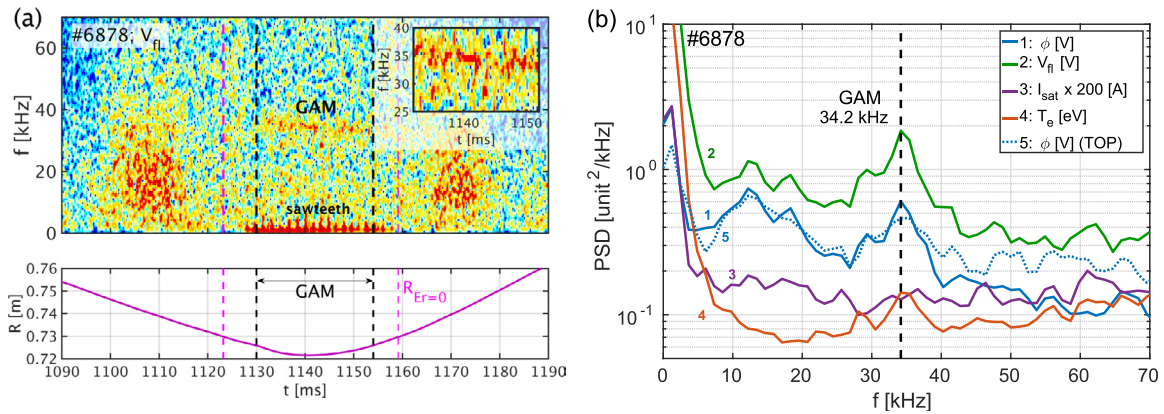


Figure 3. (a) Spectrogram of V_{fl} during reciprocation of HRCP. Probe position in time is shown at the bottom. Magenta lines mark position of the $R_{Er=0}$ radius and black vertical lines mark the appearance of GAM. The radial localization of the GAM region corresponds to that marked in figures 2(a) and (b) by the pink background. The inset plot zooms the spectrogram on the GAM oscillations. (b) Power spectral density of HRCP (solid) and VRCP (dotted) signals in the discharge #6878, 8 mm inside $R_{Er=0}$ at HRCP and 5 mm inside $Z_{Er=0}$ at the top.

2.3. Other diagnostics

Line averaged density n_e is measured by a single-channel interferometer ($\lambda = 2$ mm) along a central vertical chord. High-resolution Thomson scattering system (TS) [40, 41] is used to obtain electron temperature and density profiles vertically at the top of the plasma with spatial resolution ~ 3 –4 mm and temporal resolution 16 ms. The relatively low temporal resolution is increased by combining TS data with fast measurement of relative temperature changes by an ECE/EBW system [42]. Neutral particle analyzer (NPA) provides ion temperature in the center of the plasma. To approximate profiles of T_i with respect to the normalized poloidal flux ψ_N we use formula $T_i(\psi_N) = \{T_i(\psi_N = 0) + [T_e(\psi_N = 0) - T_i(\psi_N = 0)]\psi_N\} / [T_e(\psi_N) / T_e(\psi_N = 0)]$. Single central chord (figure 1(a)) of a multi-chord SXR system is used to monitor soft-x-ray (SXR) radiation in the plasma center and to detect temporal evolution of a sawtooth instability in the plasma center.

3. GAM oscillations

On COMPASS, an electrostatic as well as magnetic component of GAM oscillations can be observed. First, we describe localization of the mode on the data from the horizontal reciprocating probe. Figure 3(a) shows spectrogram of the V_{fl} signal during movement of HRCP in the flat-top of a diverted discharge (#6878, $I_p = 170$ kA, $n_e = 3.5 \times 10^{19}$ m $^{-3}$, $q_{95} = 4.6$). As soon as the probe gets several millimeters inside the $R_{Er=0}$ radius, it starts to register intermittent GAM oscillations at frequency $f_{GAM} \sim 35$ kHz. The situation is similar also in circular discharges but the observed GAM frequency is higher (>40 kHz) and the GAM mode is detected significantly deeper in the plasma (compare the pink areas in the figures 2(a) and (c)). GAM extends from this point radially into the plasma throughout the whole range that the probe can penetrate before becoming overheated (typically 1–2 cm from $R_{Er=0}$ at the LFS but even more than 3 cm at the top) and probably continues further inward.

Appearance of GAM is a combined effect of its drive and damping. As the combination of a collisional and Landau

damping [43] in the edge is approximately 5–10 times higher in the diverted case (compare insets of figures 2(b) and (d)), where the mode is detected closer to the edge, the observed difference in the GAM localization is not caused by a difference in the absolute value of GAM damping rate. Nevertheless, GAM edge correlates with the radius where T_e profile suddenly steepens towards SOL, which will cause faster GAM suppression due to a relative increase of the collisional damping compared to the plateau present in the GAM region. Moreover, an inward radial shift in the edge turbulence characteristics, which may influence also drive of the mode, comparable to the shift of GAM edge, was found in plasmas with low elongation. Localization of a transition region between the hole-dominated (inside, negative skewness of density fluctuations) and blob-dominated (outside, positive skewness) regions, where number of blobs and holes is balanced and PDF of density fluctuations is Gaussian, roughly corresponds in both cases to the GAM edge.

3.1. Spectra of electrostatic and magnetic components

Since poloidal structure of GAM is $m_\phi \approx 0$ in the potential and $m_n \approx 1$ in the density (with the node of oscillations localized at the midplane) and also $\delta n/n = \sqrt{2} k_r \rho_i \delta \phi / (e T_e) \sin(\theta) \gg \delta \phi / (e T_e)$ [2], where θ is the poloidal angle, k_r is the GAM radial wavenumber, ρ_i is the ion Larmor radius, and $k_r \rho_i < 1$, it is expected that close to the midplane GAM should exhibit significant oscillations of ϕ but no or only weak oscillations of I_{sat} or density (as shown e.g. in [44]). This is confirmed by a power spectral density (PSD) of probe signals plotted in figure 3(b). The PSD was computed over the whole region where the GAM oscillations are present in the probe signals (see black dashed lines in figure 3(a)) and it shows a clear peak on ϕ and V_{fl} , i.e. oscillations linked to the plasma potential, both at the LFS and the top, but no peak in the spectra is present on the I_{sat} signal at the LFS, which is consistent with the basic model of the GAM poloidal structure. Absence of the I_{sat} fluctuations is further confirmed by a negligible cross-coherence between the I_{sat} and both potential signals, that was evaluated at the GAM frequency. Interestingly, the

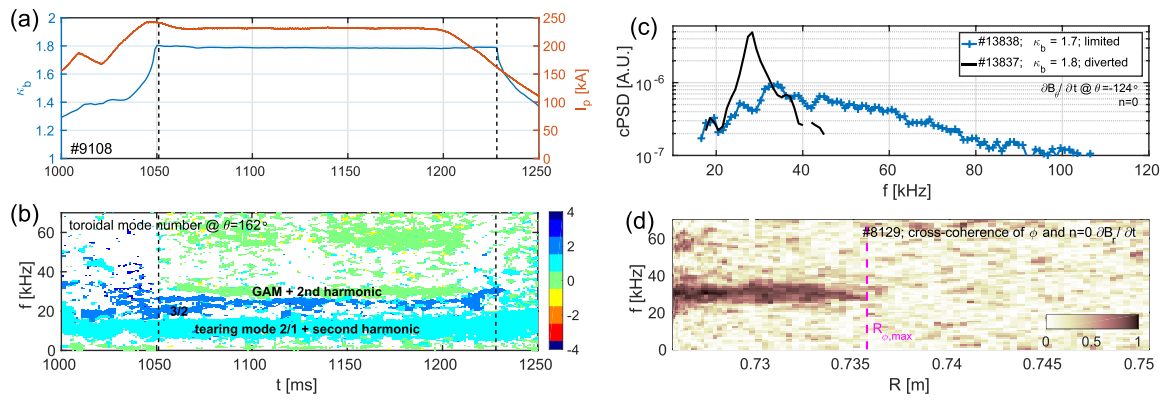


Figure 4. (a) Plasma current and boundary elongation in the discharge #9108. (b) Toroidal mode number of $\partial B_p/\partial t$ oscillations in #9108 evaluated from the cross-phase of toroidally shifted Mirnov coils MC-C13 and MC-B13. Vertical lines mark diverted phase of the discharge. (c) Coherent part of the $n=0$ $\partial B_p/\partial t$ spectra in the case of a diverted and a strongly elongated discharge. (d) Cross-coherence of the $n=0$ component of $\partial B_p/\partial t$ signal and fluctuations of the plasma potential at midplane.

oscillations in ϕ and V_{\parallel} are not identical, which implies presence of a small oscillation in T_e in the order of $\delta T_e \approx 1\text{--}2\text{ eV}$ or $\delta T_e/T_e \sim 2\%$ (for more details see figure 13(d) in section 3.4).

GAM is not a purely electrostatic mode and it is expected to exhibit also electromagnetic features. In COMPASS diverted discharges the magnetic GAM component is strong enough to be directly measured by Mirnov coils and saddle loops. This is demonstrated in figures 4(a) and (b) that show time evolution of modes visible in the spectra of $\partial B_p/\partial t$ signals at the HFS midplane in discharge #9108 ($I_p = 230\text{ kA}$, $n_e = 6.5 \times 10^{19}\text{ m}^{-3}$, $q_{95} = 3.5$). While there is no clear $n=0$ mode (green color) visible in the limited phase of the discharge, at about the same time when the X-point is created, axisymmetric oscillations attributed to GAM appear at frequency 29 kHz. The oscillations last until the end of the flat top phase and disappear when the elongation is decreased and the plasma becomes limited again. To confirm that the magnetic oscillations are related to the oscillations of the plasma potential, a cross-coherence of both has been computed and plotted in figure 4(d).

In the limited plasmas, the magnetic GAM oscillations are still present, both in B_p and B_r , but with a weaker amplitude, often below the background level, and somewhat different poloidal structure, visible only at HFS around $\theta \approx \pm(90\text{--}135)^\circ$.

Figure 4(c) shows difference in coherent spectra of $\partial B_p/\partial t$ for a strongly shaped limited plasma and the diverted plasma. The coherent spectrum cPSD was computed to limit the effect of the background fluctuations as $\text{cPSD}(f) = c_{AC}(f)\text{PSD}_A(f)$, where $c_{AC}(f)$ is the cross-coherence between two toroidally separated poloidal Mirnov coils from rings A and C and PSD_A is the power spectral density of the coil A. Data points at frequencies with non-zero cross-phase, i.e. $n \neq 0$, were removed. While only a single peak is present in diverted cases ($\kappa_b \geq 1.8$, $\delta_1 \geq 0.5$), the spectrum is significantly broader in the limited plasmas ($\kappa_b \leq 1.75$, $\delta_1 \leq 0.46$), with detectable $n=0$ oscillations and non-negligible cross-coherence in the range 25–100 kHz. This suggests that in the latter case the coils pick up GAM oscillations coming from different plasma regions with different f_{GAM} , likely from a continuum GAM. With shaping increased close to $\kappa_b \approx 1.7$ a small peak typically

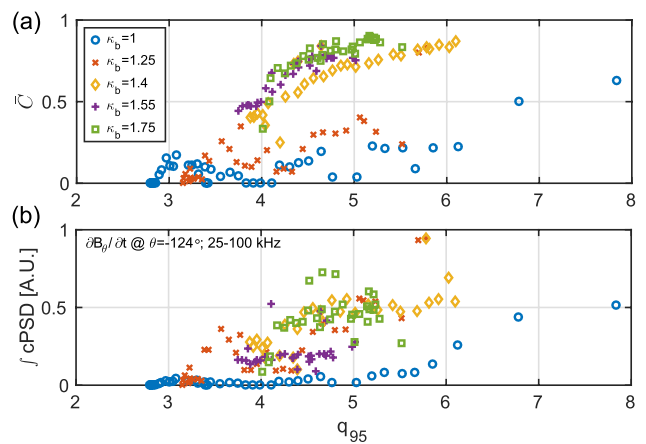


Figure 5. Dependence of the mean cross-coherence between Mirnov coils MC-A17 and MC-C17 (a) and integral of the coherent part of the spectra cPSD (b) in the frequency range 25–100 kHz on edge safety factor and elongation in a series of current ramp-up discharges ($n_e = 3$). Frequencies with a non-zero phase shift were set to 0 during the averaging/integration.

starts to form around 30 kHz at the bottom part of the broad spectra, i.e. in the plasma edge. When the shaping further increases above $\kappa_b \approx 1.75$ and an X-point is formed, a formation of a single dominant non-local GAM with strong magnetic oscillations around a single frequency is triggered, while the rest of the $n=0$ spectra typically becomes suppressed. Properties of this dominant mode will be described in the rest of the paper.

As the Landau damping increases with q , the GAM amplitude is expected to scale with q as well. Similar trend is observed for the magnetic component of the broadband GAM oscillations in the limited plasmas. Figure 5(a) shows mean coherence between two toroidally shifted Mirnov coils in the GAM frequency range 25–100 kHz, where contributions of $n \neq 0$ parts of the spectra were set to zero, plotted as a function of q_{95} and boundary elongation κ_b . This represents a relative amplitude of the GAM activity in this frequency range with respect to the background fluctuations. The relative amplitude clearly increases with q_{95} and also with the plasma shaping. The increase with q_{95} is visible also for the absolute

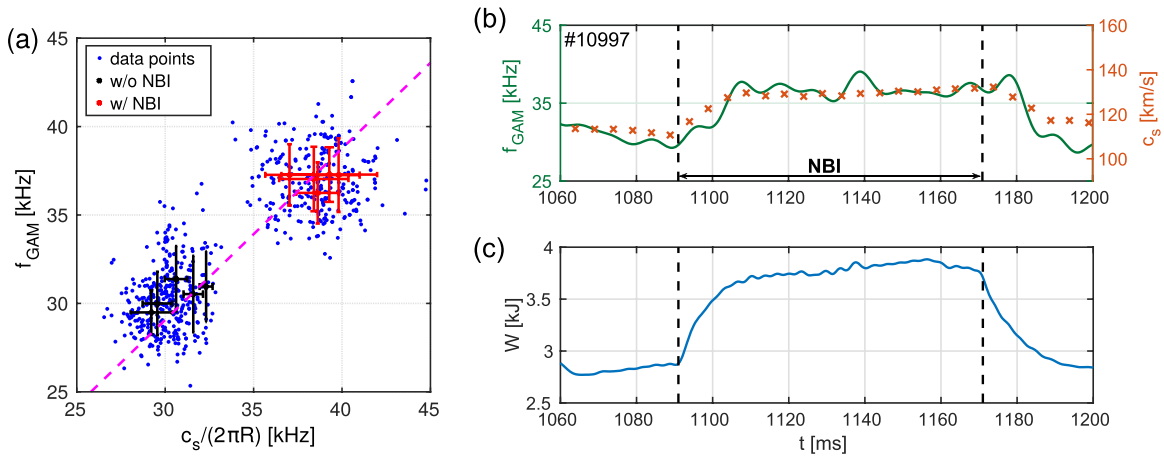


Figure 6. (a) GAM frequency versus ion sound speed at radial position $\psi_N = 0.85$ in ohmic (1066–1090 ms; black crosses) and CO-NBI (1139–1161 ms; red crosses) phases of NBI heated discharges. The magenta dashed line represents $y = 0.98x$. The blue dots represent the same data but sampled every 0.1 ms. (b) Temporal evolution of the GAM frequency during one discharge compared with the edge ion sound speed. (c) Temporal evolution of the plasma energy from EFIT.

amplitude, represented by an integral of the coherent spectrum cPSD in the same frequency range (figure 5(b)).

3.2. Scaling of GAM frequency with the ion sound speed

A typical range of GAM frequencies f_{GAM} observed on COMPASS in diverted ohmic deuterium plasmas is 25–40 kHz. According to the local model (1), f_{GAM} should scale with a square root of the plasma temperature. A series of discharges with co-current NBI (CO-NBI) heating was performed to test the temperature dependence of frequency of the studied mode. We note that the NBI did not alter most of the plasma parameters in the edge, including plasma shape, profile of q or density. The NBI affected mainly plasma temperature and possibly also plasma rotation, which is, however, not measured.

The GAM frequency was extracted using Hilbert transform from Mirnov coil signal MC-A20 band-pass filtered around the GAM peak in the power spectra. The Hilbert transform provides temporal evolution of an instantaneous frequency of the oscillation and low-pass filter at 1 kHz was further applied to reduce the noise but to still keep the evolution of the frequency on a time scale of the sawtooth period. Blue points in figure 6 represent values of f_{GAM} and c_s down-sampled to 0.1 ms resolution. In order to identify radial position whose temperature governs the frequency of the mode, assuming that it does not change when the NBI is applied, we performed a linear regression of the measured frequency before and during NBI heating versus local c_s at several radii in the range $\psi = 0.6$ –0.99. The case with the lowest misfit given by the weighted total least squares estimate [45] was found at $\psi = 0.85$ and is plotted in figure 6(a) showing a linear scaling of f_{GAM} with the edge ion sound speed.

Data points used in the regression and shown in figure 6(a) represent f_{GAM} and c_s in the ohmic phase of the discharge (black) and after reaching an NBI-heated equilibrium (red). Time evolution of the frequency, edge c_s , and plasma energy during one discharge, including a transition period, is shown in more detail in figures 6(b) and (c). Here the GAM frequency

changes smoothly and in relation to the change of plasma energy caused by the NBI, following evolution of local c_s .

Due to a presence of the sawtooth instability, the temperature of the plasma has often a non-negligible temporal evolution even in the flat-top phase of the discharge. After each sawtooth crash, an energy is expelled from the core and propagates towards the plasma boundary on a timescale of several hundreds of microseconds, where it can temporarily change the local temperature by tens of percent [31] as is demonstrated in figure 7(a) (#8848, $I_p = 210$ kA, $n_e = 2.5 \times 10^{19} \text{ m}^{-3}$, $q_{95} = 3.7$). Comparison of edge and core diagnostics shows that a typical delay between the sawtooth crash in the center and the perturbation of the edge is approx. 100–500 μs .

Since GAM frequency is temperature dependent, one would expect periodic oscillations of f_{GAM} with the sawtooth period, similar to the behavior reported on T-10 [22]. While the GAM signal on the electrostatic probes is intermittent (see zoom of the V_{fl} spectrogram in figure 3(a)) and larger statistics than that currently available would be needed to follow the temporal evolution of the frequency, the temporal oscillations of f_{GAM} can be visualized on magnetic diagnostics during a strong sawtooth activity.

Figures 8(a) and (b) show a wavelet spectrogram of a $\partial B_p/\partial t$ signal compared with the central SXR channel. A conditionally averaged evolution of the spectrogram during the sawtooth period is plotted in figure 8(c). The conditional average was performed over 100 ms of the flat-top (#11506, $I_p = 200$ kA, $n_e = 4.5 \times 10^{19} \text{ m}^{-3}$, $q_{95} = 3.7$), the drops of the central SXR that indicate a time of the sawtooth crash in the center were used as triggers. Each drop of the SXR signal (figure 8(e)), caused by an expulsion of energy from the core, is followed by an increase of f_{GAM} delayed by approx. 300 μs , i.e. the time is comparable to the time needed for the energy to propagate from the core to the plasma edge. However, it still comes before the pulse arrives into the SOL as indicated by the delay of a peak in D_α emission in figure 8(d). After the initial sharp increase, the frequency gradually relaxes back to its initial value in a way that is similar to the behavior of T_e in

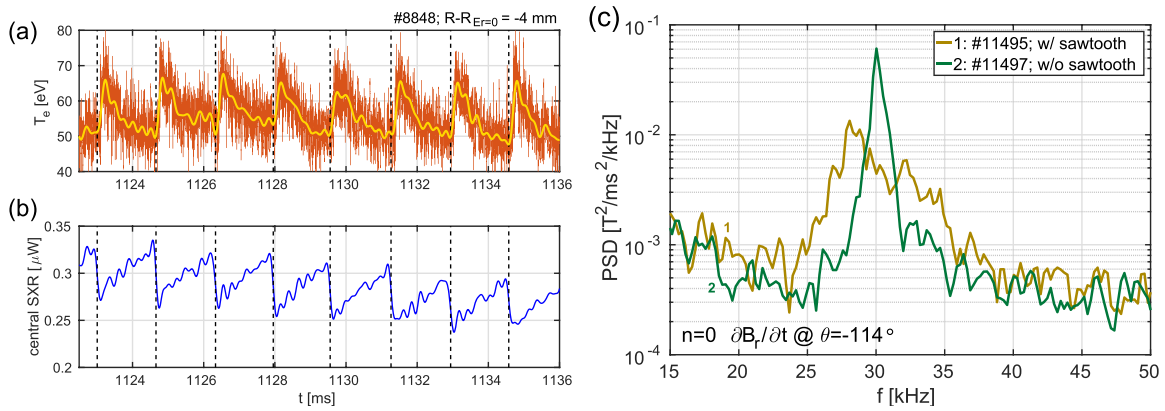


Figure 7. Evolution of the edge plasma temperature measured by HRCF (a) and the core emission of SXR (b). (c) PSD of an axisymmetric part of $\partial B_r/\partial t$ fluctuations in the divertor region in two similar discharges with (gold, 1) and without (green, 2) sawtooth instability.

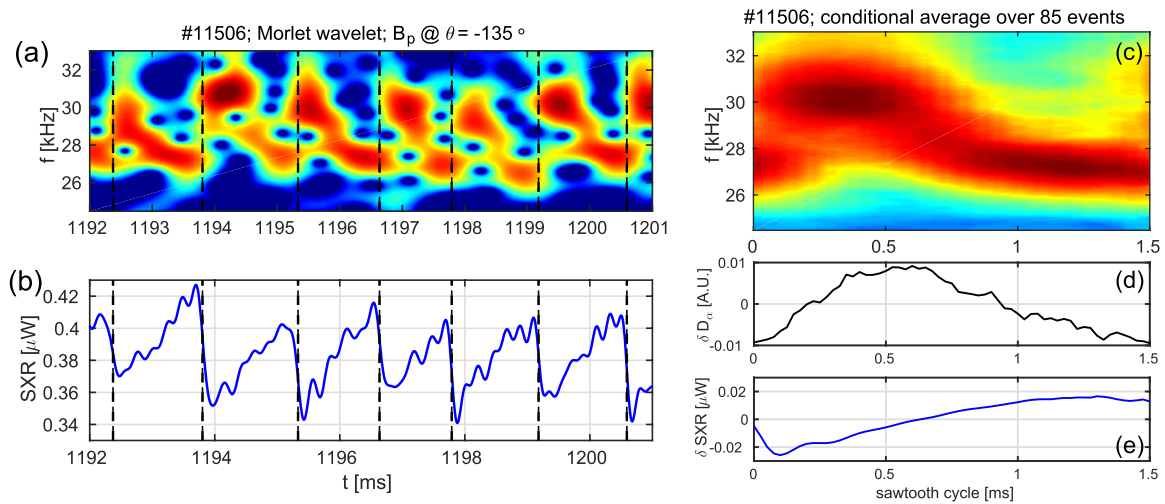


Figure 8. Wavelet spectrogram of $\partial B_r/\partial t$ at MC-A20 during a strong sawtooth activity (a) and the core emission of SXR (b). Conditional average of (a) and (b) and perturbation of D_α emission over 85 sawtooth crashes is shown in (c)–(e).

figure 7(a). The observed change of the frequency would, due to the f_{GAM} dependence on c_s , correspond to a relative change of plasma temperature in the order of tens of percent, i.e. well within the observed range. At this moment, however, the outlined relation between oscillations of f_{GAM} and edge T_e cannot be proved quantitatively since a fast measurement of edge T_e was not available due to overheating of the Langmuir pin by the large sawteeth in the same discharges where significant oscillations of f_{GAM} were measured by the magnetic coils.

The temporal oscillations of f_{GAM} then explain the relative width of the GAM PSD in figures 3 and 4. Figure 7(c) shows difference of the PSD in an ohmic phase of two similar discharges ($I_p = 180$ kA, $n = 4.5 \times 10^{19} \text{ m}^{-3}$, $q_{95} = 3.6$) following 80 ms of CO-NBI heating. In one of them ($P_{NBI2} = 270$ kW) the NBI power was sufficient to stabilize the sawtooth instability leading to a narrow GAM peak $\delta f_{GAM}/f_{GAM} \sim 0.13$ while in the other one ($P_{NBI2} = 220$ kW) the sawtooth instability is present and the GAM peak remains broad, $\delta f/f \sim 0.38$. As visible from figure 8, the broad double-peaked structure of PSD observed in discharges with sawteeth (yellow line in figure 7) does not correspond to a simultaneous presence of two or more modes co-existing at close frequencies, but rather to a temporal evolution of a single mode. When

the perturbation caused by sawteeth is not present, the peak remains narrow. Absence of the sawteeth also increased the GAM amplitude, represented either by the area under the GAM peak in PSD or by a variance of fluctuations in the range 24–36 kHz, both by 35%.

Even though f_{GAM} changes with heating power and it seems to react also on temporal evolution of plasma temperature during the sawtooth cycle, the frequency remains constant in space and does not scale with radial profile of local electron temperature in the edge layer penetrated by the probes. Figure 9 compares f_{GAM} estimated from the spectra of a plasma potential measured by VRCP at the top of a hydrogen plasma (#11162, $I_p = 200$ kA, $n_e = 8 \times 10^{19} \text{ m}^{-3}$, $q_{95} = 3.9$) with a local profile of $\sqrt{T_e}$ measured by the same probe head. In the case of a local GAM the frequency scaling given by the equation (1) holds locally and the profile of f_{GAM} should follow the profile of $\sqrt{T_e}$, assuming a constant ratio of T_i/T_e at the edge and neglecting a change of q . However, as figure 9 shows, in COMPASS plasmas the frequency remains approximately constant while $\sqrt{T_e}$ changes by a factor of 1.5. This indicates presence of a non-local GAM with a frequency plateau in the radial direction. The extent of the plotted data is limited by the range of probe measurements but the frequency plateau seems

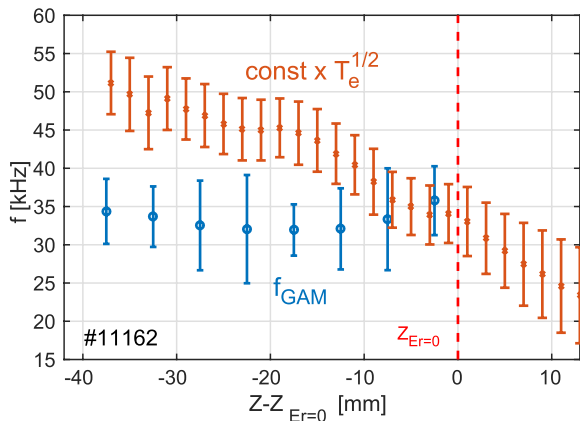


Figure 9. Spatial profile of f_{GAM} (blue) and of $\sqrt{T_e}$ scaled to fit f_{GAM} around $Z_{E_r=0}$ (orange).

to continue further inward. Currently it is not clear what is the full radial extent of the GAM and at which radius does the mode originate. Two examples from other devices show that a non-local mode can form radially localized plateau regions as on AUG [23] or it could even span the whole plasma as on T-10 [28].

3.3. Poloidal structure

While axisymmetric in all fields, GAM is expected to have different poloidal mode numbers in plasma potential, m_ϕ , density, m_n , and magnetic field, m_B .

The oscillations of plasma potential should be constant on a flux surface with mode numbers $m_\phi/n \approx 0/0$. This structure implies presence of long-range correlations (LRC) with a zero phase shift at the GAM frequency between plasma potential measured at two poloidally and toroidally displaced parts of a single flux surface. On COMPASS, this can be detected using the pair of reciprocating probes that are located at the LFS and top of the plasma and toroidally shifted. This is shown in figure 10 using cross-coherence of V_{fl} during a simultaneous deep plunge of the probes (#7732, $I_p = 200$ kA, $n_e = 4 \times 10^{19} \text{ m}^{-3}$, $q_{95} = 4$). An increased value of the coherence clearly appears shortly after both probes enter the relevant area inside the $R_{E_r=0}$ radius and disappears just before the first of them leaves it. On the same flux surface, marked by the black dashed vertical line, the cross-coherence of the signal reaches 0.9 and the mutual phase shift is close to zero (figure 10(c)), $\Delta\varphi = 0.1\pi$, consistent with $n/m_\phi \approx 0/0$ expected for GAM.

This observation is further supported by an estimation of a wavenumber-frequency spectra [46] from two-point measurements of two BPPs located on the horizontal manipulator and separated vertically by 1.6 cm. This method assumes that the measured signals consist of a superposition of wave packets characterized by the wave number $k(f)$ and frequency f . When two signals measured at the distance Δx are divided into M realizations of an equal length, the local wavenumber-frequency spectrum $S(k, f)$ can be estimated as

$$S(k, f) = \frac{1}{M} \sum_{j=1}^M I_{\Delta k}(k - k^j(f)) \times \frac{1}{2} [S_1^j(f) + S_2^j(f)]. \quad (3)$$

Here, S_1^j and S_2^j are power spectra of the signals, $k^j(f) = \Delta\varphi_{12}^j(f)$ is a local wave number, $\Delta\varphi_{12}^j(f)$ is a cross-phase between the signals in the realization j , and $I_{\Delta k}(x)$ is an indicator function such that $I_{\Delta k}(x) = 1$ for $x < \Delta k$, and 0 otherwise.

Based on the wavenumber-frequency spectrum $S(k, f)$ one can define also the statistical dispersion relation

$$\bar{k}(f) = \int k S(k, f) dk / \int S(k, f) dk \quad (4)$$

and the wavenumber spectrum width

$$\sigma_k(f) = \sqrt{\int (k - \bar{k}(f))^2 S(k, f) dk / \int S(k, f) dk}. \quad (5)$$

$S(k, f)$ estimated from 285 ms of two-point ϕ measurements collected from several identical discharges (#9548-9559, $I_p = 200$ kA, $n_e = 3 \times 10^{19} \text{ m}^{-3}$, $q_{95} = 3.8$) and carried out by BPP1 and BPP3 in the GAM region is plotted in figure 10(d). The estimate of the GAM poloidal wavenumber and the wavenumber spectrum width computed using the equations (4) and (5) is $\bar{k}_p(f_{\text{GAM}}) = 0.01 \pm 0.08 \text{ cm}^{-1}$, which corresponds to the poloidal mode number $m_\phi = 0.2 \pm 1.4$. The mean value is close to $m_\phi \approx 0$ within the precision given by a radial misalignment of the probe pins with respect to the magnetic surfaces, estimated from an EFIT reconstruction as ~ 0.1 – 0.2 cm, and the fact that $k_r \gg k_p$ (see section 3.4 for estimation of k_r in the same type of discharge).

In the case of the magnetic component, a standing wave with $m_B = 2$ structure shown in figure 11(g) is predicted for circular plasmas [16, 19] and has been previously confirmed on several devices [20, 21]. However, additional Fourier components can be excited as an effect of plasma shaping [16], radial width of the mode or plasma beta [17, 18]. Poloidal structure of the amplitude and phase of the GAM magnetic component in a diverted COMPASS plasma without sawteeth is plotted in figures 11(a)–(f) for two components of the magnetic field, B_r and B_p . The structure exhibits phase jumps by $\sim \pi$, confirming the non-rotating standing wave structure of the oscillations, even though the poloidal structure is more complex than simple $m_B = 2$. The B_r field (figure 11(c)) has two regions of a constant phase shift $\varphi \sim \pi$ at the top and bottom of the plasma, consistent with GAM in an ideal circular plasma, but the bottom one is relatively narrow and an additional region with $\varphi \sim \pi$ and low amplitude of oscillations appears around HFS midplane. In the B_p field, the bottom HFS part seems to have a mixed phase of $\varphi \sim \pi/2$ and an additional region with $\varphi \sim \pi$ appears at the bottom LFS.

The amplitude of the magnetic oscillations plotted in figure 11 has been estimated in a 5 kHz frequency band centered around f_{GAM} . The oscillations in B_r are about one order of magnitude weaker than in B_p . GAM is strongest in both

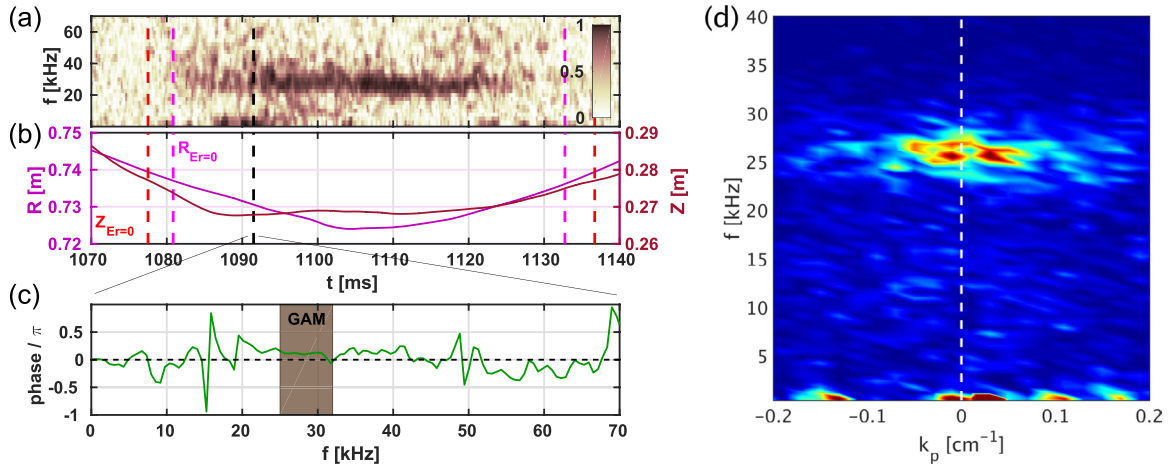


Figure 10. (a) Cross-coherence of $V_{||}$ at the top and LFS midplane measured by HRCP and VRCP in discharge #7732. (b) Position of the probes in time. The vertical black dashed line marks the time when both probes are at the same flux surface; red and magenta dashed lines mark crossing of the position of $E_r = 0$. (c) Cross-phase of the $V_{||}$ oscillations measured simultaneously on the same flux surface at the top and LFS midplane. The brown region marks the GAM frequency. (d) Poloidal wavenumber-frequency spectrum of plasma potential fluctuations measured by HRCP at the outer midplane using two BPPs separated vertically by 1.6 cm.

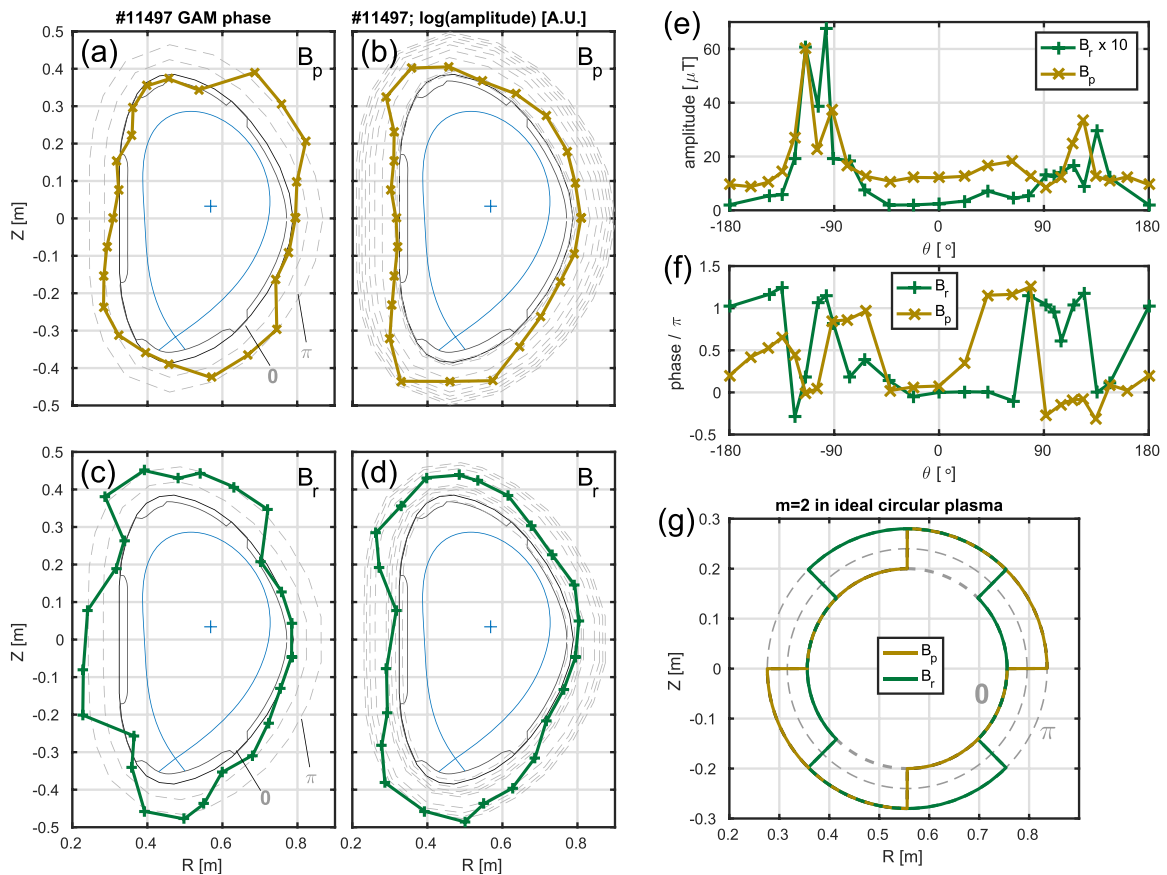


Figure 11. Poloidal structure of the GAM phase shift (a), (c) and (f) and structure of the standard deviation of magnetic fluctuations around the GAM frequency (b), (d) and (e) for the $n = 0$ component of B_r field (c)–(f) and the local B_p field (a), (b), (e) and (f). GAM phase with the $m = 2$ structure predicted for an ideal circular plasma is shown in (g). Contours of a constant value are marked in (a)–(d) by the gray dashed lines and follow rescaled shape of the vessel.

components at the bottom and the top of the plasma, somewhat shifted to the HFS, and weak on midplane. This is similar to the GAM structure observed on TCv [20]. The regions of the non-standard phase shift exhibit an overall low amplitude of oscillations and can thus be considered to be only a minor perturbation of the GAM structure.

3.4. Radial structure

In order to determine radial structure of GAM, two methods were used. First, we have used the $n = 0$ component of saddle loops S17 as a reference signal and computed cross-phase $\varphi_{cc}(R)$ of the magnetic oscillations at GAM frequency and

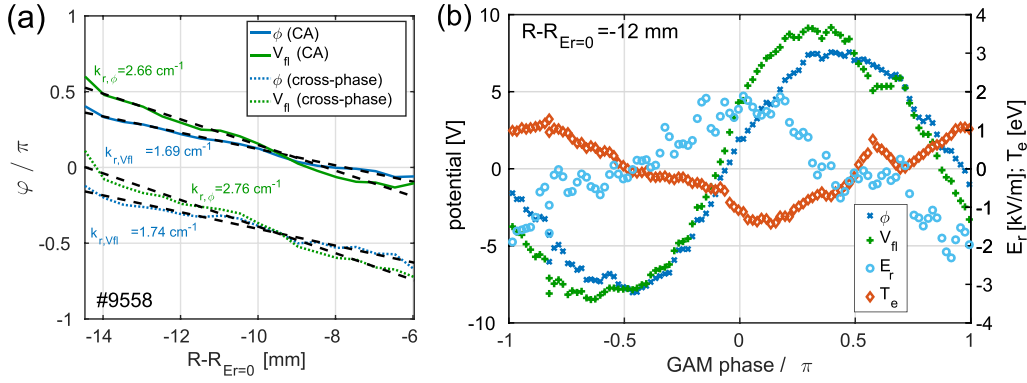


Figure 12. (a) Cross-phase φ_{CC} of potential and magnetic fluctuations and phase φ_{CA} of the conditionally averaged (CA) fluctuations as a function of the radial position of the probe. Black dashed lines show the linear fit of GAM k_r . (b) Evolution of the potential, electric field and temperature perturbation at a fixed probe position during an average GAM phase.

a potential measured during the movement of the horizontal probe head. The radial GAM wavenumber k_r was then determined by a linear regression as $k_r = -\varphi_{CC}(R)/\partial R$.

Second, an instantaneous phase φ_{GAM} of the $n = 0$ magnetic oscillations in $\partial B_r/\partial t$ from the coil S17 band-passed around GAM peak was determined using Hilbert transform. Since the magnetic signal is measured at a fixed point, independent on the probe position, and the mode frequency is not radially dependent, the phase φ_{GAM} can be interpreted as a GAM phase at some fixed, even though unknown radius. This allows to use φ_{GAM} as a trigger to compute a conditionally averaged GAM oscillation of the plasma and floating potentials with respect to φ_{GAM} . The averaging was performed independently for each probe radius and, as it exhibits a harmonic behavior (see figure 12(b)), it was fitted by a harmonic function $V(R,t) = \delta V \cdot \sin(2\pi f_{GAM}t + \varphi_{CA}(R))$. The radial GAM wavenumber k_r was then determined similarly as in the first case as $k_r = -\varphi_{CA}(R)/\partial R$.

Comparison of k_r , $\varphi_{CA}(R)$ and $\varphi_{CC}(R)$ of plasma and floating potentials is plotted in figure 12(a). Clearly, both methods well agree and show that GAM potential oscillations at different radii are out of phase, hence, the plasma potential oscillations are accompanied also by oscillations of the radial electric field $E_r = -\partial\phi/\partial r$. The radial wavenumber k_R of the mode in plasma potential is for the first method $k_{R,\phi} = 1.74 \pm 0.16 \text{ cm}^{-1}$ and somewhat larger value is found for V_{fl} , $k_{R,V_{fl}} = 2.76 \pm 0.24 \text{ cm}^{-1}$, indicating an influence of the temperature field that itself shows even larger wave number $k_{R,T_e} = 5.68 \pm 0.59 \text{ cm}^{-1}$. Larmor radius in the measured region is $\rho_{i,T_i=T_e} \approx 2 \text{ mm}$ and the GAM radial wavelength $\lambda_r = 2\pi/k_r$ thus fulfills $\lambda_r \gg \rho_i$.

Figure 13 shows a 2D space-time plot of the conditionally averaged GAM. The amplitude of the GAM potential oscillations is $\delta V \sim 5\text{--}10 \text{ V}$ and the amplitude of the radial electric field oscillations computed as a radial derivative of the former is $\delta E_r \sim 1.5\text{--}2.5 \text{ kV m}^{-1}$, in agreement with an estimate $\delta E_r \approx k_r \delta V \sim 1.5 \text{ kV m}^{-1}$. With local $B_T = 0.87 \text{ T}$ this corresponds to an amplitude of the poloidal $E \times B$ drift fluctuations in the order of $\sim 2\text{--}3 \text{ km s}^{-1}$, i.e. $\geq 40\%$ of the maximal magnitude of the poloidal edge flows, and is comparable to the local mean poloidal flow $\langle v_p \rangle|_{R=0.726 \text{ m}} = 2.2 \text{ km s}^{-1}$. An estimate of the shearing rate caused by GAM gives

$\omega_{E \times B} = \partial v_p / \partial r = -\partial^2 \delta \phi / \partial r^2 / B \approx k_r^2 \delta \phi / B \approx 5 \times 10^5 \text{ s}^{-1}$. This value is about a factor of 3 smaller than the shearing rate of the mean flow that peaks around $R_{E_r=0}$ with $\max(|\omega_{E \times B}|) \approx 1.5 \times 10^6 \text{ s}^{-1}$.

Figure 13 also shows that the GAM perturbation propagates radially outward with a radial velocity of propagation of the potentials $0.6\text{--}0.8 \text{ km s}^{-1}$. This value is comparable to the velocity $v_r \approx 0.6 \text{ km s}^{-1}$ found for the floating potential on the TEXTOR tokamak [10]. On COMPASS, the radial velocity, however, differs between the potentials and the temperature, whose radial propagation is slower. This seems to be consistent with the observed difference in the radial wave numbers, taking into account that for a radially propagating wave it holds $v_r k_r \approx 2\pi f_{GAM}$.

3.5. GAM interaction with the turbulence

One of the key properties of GAM is its three-wave interaction with turbulent oscillations that drive the mode. Such interaction can be detected using bicoherence [47, 48]. The squared (auto-)bicoherence of a signal $x(t)$ with a Fourier spectrum $X(f)$,

$$b_x^2(f_1, f_2) = \frac{|\langle X(f_1) X(f_2) X^*(f_1 + f_2) \rangle|^2}{\langle |X(f_1) X(f_2)|^2 \rangle \langle |X(f_1 + f_2)| \rangle},$$

where $\langle \cdot \rangle$ represents an averaging over different segments of the signal, is used to identify frequencies that exchange energy by a non-linear interaction. A typical pattern of high values of bicoherence at $b(f, \pm f_{GAM})$, $b(f_{GAM}, f)$ and $b(f, f \pm f_{GAM})$ for a broad range of frequencies f is expected for GAM [8, 14]. To confirm this property for the mode observed on COMPASS, wavelet bicoherence [48] has been computed in figures 14(a) and (b). While a similar picture can be obtained also using the standard Fourier bicoherence, the wavelet bicoherence appears to be more robust when f_{GAM} oscillates in time and the time series is limited by a fast reciprocation of the probe.

The plot confirms the interaction of GAM with other oscillations in a broad range of frequencies. Moreover, in figure 14(c) we plot summed squared bicoherence defined as $b^2(f) = \sum_{f=f_1+f_2} b^2(f_1, f_2) / N(f)$, where $N(f)$ is the

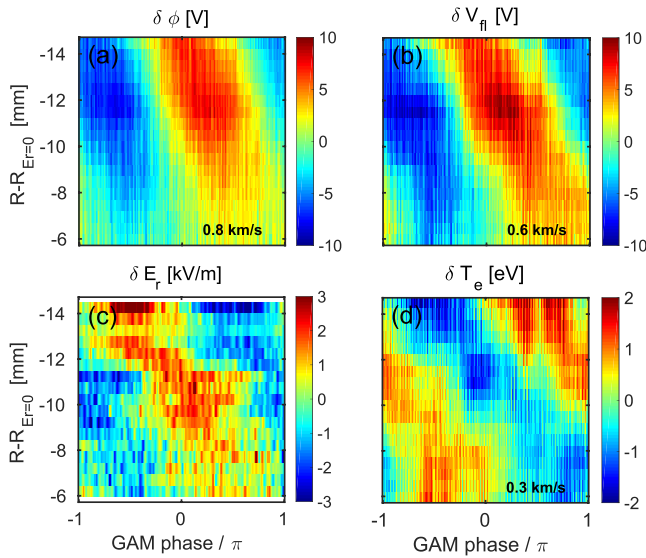


Figure 13. Radial structure and temporal evolution of the conditionally averaged GAM in #9558 in plasma (a) and floating (b) potentials, radial electric field (c) and electron temperature (d). The radial velocity of propagation was estimated from a movement of the position of zero perturbation by linear regression.

number of Fourier components in the summation, and compare it with cross-coherence between local plasma potential and I_{sat} measurements. The plot indicates that GAM nonlinearly exchanges energy mainly with fluctuations in the frequency range 100–500 kHz that correspond to coherent structures of the ambient turbulence.

A turbulent drive of GAM may then explain the fact that the GAM is observed in L-mode only, disappearing whenever the turbulence is suppressed during an L-H transition and reappearing shortly after the H-L back transition when the turbulence recovers, as shown in figure 15(a) (#8967, $I_p = 270$ kA, $n_e = 6\text{--}12 \times 10^{19} \text{ m}^{-3}$ ramp-up, $q_{95} = 2.5$).

Interestingly, the bicoherence is more pronounced in the floating potential than in the plasma potential, indicating non-negligible contribution also from the temperature field. We note that the difference is not caused by the different measurement techniques (BPP versus LP): when the LP becomes self-emissive and both probes measure a similar potential, the difference in the bicoherence disappears.

4. Change of GAM amplitude with NBI heating

Most of the GAM properties studied in the previous chapters were obtained in ohmic plasmas. Even though a detailed study of the influence of NBI on the GAM properties is beyond the scope of this paper, we still find interesting to demonstrate how the NBI can change GAM.

During the additional on-axis tangential NBI heating, the GAM frequency increases with the increase of plasma temperature. The GAM amplitude changes as well, however, differently for a co-current (CO) and counter-current (CNT) injection (figure 16, $I_p = 180$ kA, $n_e = 4 \times 10^{19} \text{ m}^{-3}$, $q_{95} = 3.7$). While the GAM amplitude is slightly increased during CNT-NBI, the mode is strongly suppressed during

CO-NBI. The behavior resembles observations on other machines [12, 21], reporting easier GAM excitation during CNT-NBI heating than during CO-NBI. Nevertheless, on COMPASS the NBI does not generate a new GAM but rather modifies GAM already existing in ohmic plasmas, without presence of fast ions. Below we discuss two ways how the GAM amplitude could be affected by a direction of the NBI heating.

First, the GAM growth rate γ_{GAM} could be modified through an interaction with fast resonant particles. In [29] it is shown for the case of a slowed-down velocity distribution of fast ions with strongly peaked pitch angle distribution of the form $f_0 = n_b(r)\delta(\chi - \chi_b)\eta(v_b - v)/v^3$ that GAM can be influenced by the fast ions differently for CO- and CNT-NBI. Here n_b and $\chi = v_{\parallel}/v$ is the concentration and pitch angle of the fast particles, respectively, δ is a delta function and η is a step function.

The mode growth rate due to the interaction with fast particles is predicted smaller for CO-NBI than CNT-NBI, which may explain differences in the generation of a new EGAM by NBI observed elsewhere. Moreover, there is a region of parameters where the growth rate is negative and presence of the fast particles could lead to a stabilization of an existing mode. The stabilization can appear due to spatial inhomogeneity of the fast particles, which acts for any χ to stabilize/destabilize the mode in the case of CO/CNT injection, assuming $\partial n_b/\partial r < 0$, or due to velocity anisotropy of the fast particles that stabilizes the mode for $\chi^2 > 0.6$ and destabilizes otherwise, independently on the beam direction. Due to the effect of the spatial inhomogeneity the stabilization is more likely to happen in the CO-NBI case, but the growth rate can be negative even for CNT-NBI if the effect of the velocity anisotropy overcomes the effect of the spatial inhomogeneity.

To estimate the region of pitch angles that could cause GAM damping on COMPASS, a boundary between regions of the positive and negative growth rates was plotted for the CO-NBI case in figure 17(a). In the CNT-NBI case the growth rate was positive everywhere except the largest pitch angles in the central plasma ($|\chi| > 0.9$, $\Psi_N < 0.25$). The growth rates were evaluated based on the experimental profiles shown in figure 17(b) using relation for GAM frequency and growth rate (59) in [29] that is valid in low-beta plasmas. Only the branch that corresponds in the limit $n_b = 0$ to the standard GAM frequency is considered. Comparison of the most common pitch angle estimated with FAFNER code for COMPASS cases modelled in [49] with the minimum pitch angle needed for GAM damping in figure 17(a) indicates that during CO-NBI the fast particles can be present in the region where they can decrease the GAM amplitude. Nevertheless, this optimistic estimate does not take into account that the full distribution function will be significantly broader in χ than the assumed δ -function, as the energy of fast particles quickly, on a millisecond time scale, slides down towards the critical energy $E_c = 14.8T_e[(A_{\text{NBI}}^{3/2}/n_e) \sum_i n_i Z_i^2/A_i]^{2/3}$, where the pitch-angle scattering becomes important due to ion-ion collisions [50]. Here A_{NBI} is the mass number of NBI ions and A_i and Z_i are the mass and charge numbers of the plasma ion species.

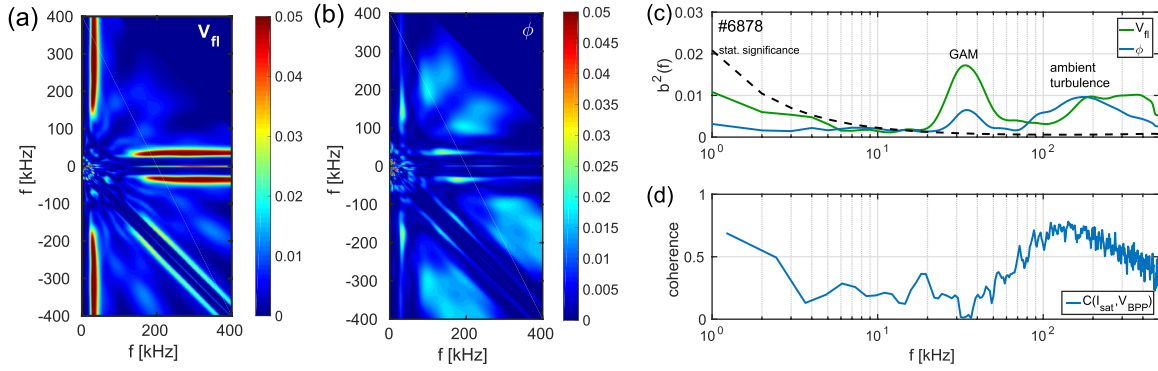


Figure 14. Wavelet bicoherence of floating (a) and plasma (b) potential in #6878. Summed squared bicoherence is shown in (c) and cross-coherence of I_{sat} and ϕ in (d).

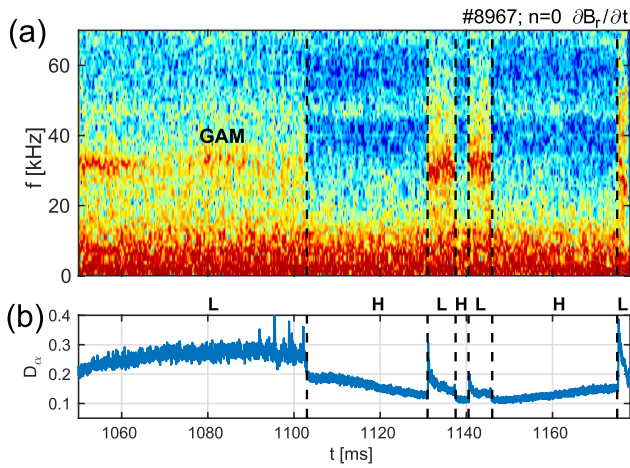


Figure 15. Spectrogram of $\partial B_r/\partial t$ in the divertor region (a) showing GAM behavior during L-H and H-L transitions detected from D_α signal (b).

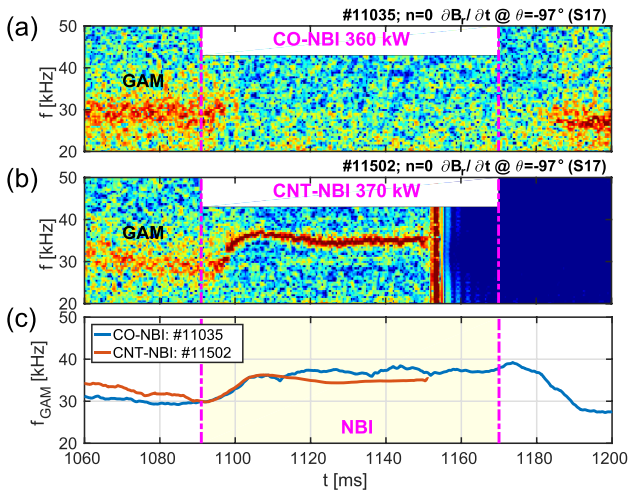


Figure 16. Spectrogram of the $n=0$ $\partial B_r/\partial t$ fluctuations in the divertor region showing frequency and amplitude of GAM magnetic component during CO-NBI and CNT-NBI heating. GAM frequency estimated by Hilbert transform is compared in (c). The CNT-NBI discharge ended with disruption at 1153 ms.

Therefore, we also consider second theory developed in [51, 52] that uses kinetic treatment to study the effect of the electron current combined with the ion flow, modelled by a

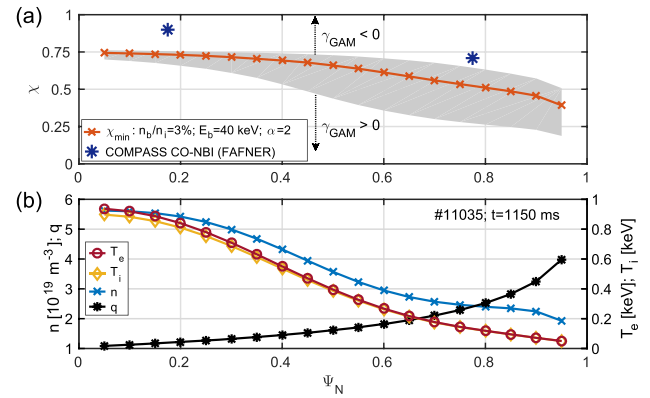


Figure 17. Minimum pitch angle χ_{min} of fast ions needed for $\gamma_{\text{GAM}} < 0$ (a), computed for CO-NBI discharge #11035 with parameters shown in (b). The orange line in (a) shows χ_{min} for one particular set of parameters with beam energy $E_b = m_i v_b^2/2$ equal to $E_{\text{NBI}} = 40$ keV. The gray area shows the region in which χ_{min} lies when the parameters are varied in the range $E_b = 20\text{--}40$ keV, $n_b/n_i = 1\text{--}5\%$ and $n_b \propto (1 - r^2/a^2)^\alpha$ with $\alpha = 1\text{--}4$. The blue stars show an estimate of the most common particle pitch angle based on the FAFNER model.

shifted Maxwell distribution with mean velocity $v_{i/e0}$, on the GAM instability. The GAM instability is predicted to occur when $v_{e0} > Rq\omega_{\text{GAM}}$. When v_{e0} is in the studied cases estimated from the EFIT current profile, the condition is fulfilled in the central plasma, but not at the edge ($\Psi_N > 0.75$), where the safety factor q increases.

The condition for the GAM instability to appear when the electron current velocity combined with the ion flow overcomes Landau damping is more precisely given by [51]:

$$\gamma_{\text{GAM}} \propto \frac{v_{e0}}{v_{Te}} \left[\frac{\rho_L}{4L_n h_\theta} \left(2 + 2\eta_i + 3\frac{T_e}{T_i} \right) + \frac{v_{i0}}{v_{Ti}} - 0.03 \frac{v_{Te}}{v_{e0}} \exp\left(2 - \frac{q^2}{2}\right) \right] \geq 0, \quad (6)$$

where $L_n = -n/(\partial n/\partial r)$, $\eta_i = \partial \ln T_i / \partial \ln n$ and $h_\theta = B_\theta/B_0$. The GAM growth rate γ_{GAM} involves a cross-term of the electron and ion velocities $v_{i0}v_{e0}$, which may be modified during the beam injection. After the ion energy slides down to the critical energy, beam momentum is transferred to the bulk plasma by ion-ion collisions, shifting v_{i0} in the opposite directions for CNT- and CO-NBI. As a result, the change of v_{i0} increases the GAM growth rate for the former and decreases for the latter and if large enough, it could result in a reduction of the

GAM amplitude [52]. Estimating the momentum transfer as $|\Delta v_{i0}| \approx n_b/n_i v_c$ where we used $n_b/n_i \approx 3\%$ and v_c is the critical beam velocity corresponding to the critical energy at which the transfer of energy to bulk ions becomes important, the velocity change in COMPASS conditions $|\Delta v_{i0}| \approx 0.2v_{T_i}$ is comparable to the first term in (6) and in the edge, where $\exp(2 - q^2/2)$ drops, also to the last term. This shows that Δv_{i0} can be large enough to significantly affect GAM growth rate in the condition (6).

The first estimates indicate that both mechanisms could influence GAM amplitude during directed NBI heating, each in a different regime of the pitch angle distribution. To draw a definite conclusion and to quantify their individual role in the observed GAM suppression, a dedicated modelling of a velocity distribution of the fast ions together with a better knowledge of the radial mode localization will be needed.

5. Discussion and summary

Geodesic acoustic mode has been identified in COMPASS plasmas based on its distinctive properties, namely frequency scaling with ion sound speed, spatial structure of the mode and its non-linear interaction with a broad-band turbulence. While the mode has been detected in diverted as well as limited plasmas, its properties were analyzed mostly in the diverted configuration where the mode is more accessible by the available diagnostics due to its localization closer to the edge of the plasma and due to its strong magnetic component.

The difference in the position of the GAM edge correlates with the position where the collisional GAM damping starts to sharply increase due to a steep decrease of the temperature profile towards SOL, which is found more inwards in limited plasmas with low elongation.

The GAM frequency was shown to vary with the plasma heating by the neutral beam injection, proportionally to the change of ion sound speed at the plasma edge. Moreover, the frequency was found to periodically oscillate with the period of the sawtooth instability, suggesting modulation of the frequency by a periodic increase of the edge temperature due to expulsion of energy from the plasma core. In the radial direction the frequency does not change with a temperature profile, indicating non-local nature of the GAM mode. This observation was, however, limited by the radial range accessible by the reciprocating probes, and thus it currently cannot be concluded how deep into the plasma does the mode continue and its full radial extent is a subject of further research.

We note that evaluation of the Alfvén-sound continuum based on experimental profiles was carried out for the diverted cases with a linear MHD code KINX [53]. The results do not show presence of gaps in the continuum and thus, according to this computation, only a local continuum GAM should exist at the plasma periphery. Since a non-local GAM was observed experimentally, some other mechanism must be responsible for its formation.

In diverted plasmas the GAM was found to exhibit magnetic oscillations in a narrow band of frequencies created by a single dominant mode, both in the poloidal and radial

components of the field. In limited plasmas, the magnetic oscillations are much weaker, for small q_{95} often below the level of background, and broadband (25–100 kHz), suggesting presence of a continuum GAM. The relative amplitude of the broadband oscillations was found to scale with q_{95} , as one would expect if governed by Landau damping, which explains why the GAM magnetic component was not previously detected on COMPASS in low- q low- κ_b plasmas.

Investigation of GAM poloidal structure revealed long range correlations of the plasma potential between different points on a single flux surface, consistent with the mode numbers $m_\phi/n \approx 0/0$. Magnetic oscillations were shown to have a form of an axisymmetric poloidal standing wave. Its poloidal structure is somewhat deformed compared to the $m_B = 2$ prediction for an ideal circular plasma and the mode exhibits regions with an altered phase of oscillations. Their amplitude is, however, small compared to the main structure. Poloidal structure of the continuum GAM differs from the diverted one mainly in the divertor region, due to a presence/absence of the X-point. With X-point, the amplitude is strongest at the poloidal angle corresponding to a position of the outer strike-point where the oscillations are not present at all in the limited plasmas. The oscillations of the continuum GAM are visible only around $\theta \approx \pm(90-135)^\circ$, consistent with $m_B = 2$ structure, nevertheless detected only on HFS.

The bicoherence analysis confirmed that the mode non-linearly exchanges energy with the ambient turbulence. Significant difference was found in the auto-bicoherence of the floating and plasma potential. This indicates non-negligible contribution of the temperature field in the bicoherence of V_{fl} , which may lead to an overestimation of the energy exchange between GAM and the local turbulence when a common assumption $V_{fl} \approx \phi$ is used due to non-availability of a direct ϕ measurement.

Interestingly, different values of the GAM radial wavelength were found for the plasma potential and for the temperature, $\lambda_\phi \sim 4$ cm and $\lambda_{T_e} \sim 1$ cm, respectively, accompanied also by different velocities of radial propagation of both fields, such that $v_r/\lambda \approx \text{const}$. Amplitude of the plasma potential oscillations $\sim 5-10$ V results in an oscillating radial electric field with an amplitude in the order of several kV m^{-1} . The associated oscillating $E \times B$ drift can reach the amplitude of the local mean flow. The shearing rate of GAM was estimated as $5 \times 10^5 \text{ s}^{-1}$, by a factor of 3 smaller than the maximal shearing rate of the mean flow. Taking into account that the GAM effective shearing rate will be further reduced due to the large frequency of the oscillations [3], the impact of the mode on turbulence is expected to be rather low compared to the mean flow or to low-frequency zonal flows.

In the last section we reported a significant reduction of the GAM magnetic signal during co-current but not counter-current NBI heating. In contrast to the observations on other machines [12, 21] where NBI destabilizes a new energetic particle driven mode, NBI on COMPASS modifies the amplitude of a mode already existing in ohmic plasmas, i.e. not driven by energetic particles. Two mechanisms how the directed NBI could influence GAM amplitude were proposed. First, if the instability due to a combined effect of the electron current

and ion flux [51, 52] contributes to the GAM growth rate, the NBI driven change of the bulk ion velocity by fast particles around or below the critical energy may increase or decrease GAM growth rate for counter- or co-current injection, respectively, i.e. in the same manner as observed in the experiment. Nevertheless, our estimates show that the condition for the electron driven instability itself is not fulfilled in the edge where GAM is observed. Second, solution of a GAM continuum equation from [29] showed that in the CO-NBI case the GAM growth rate in the edge could be decreased by an interaction with fast resonant particles with high pitch angles. Quantitative impact of both mechanisms on the growth rate and frequency of the edge GAM remains a subject of a further research. Modelling of the fast ions distribution together with an improved experimental characterization of the radial mode localization is being prepared.

Acknowledgment

Authors are grateful to Dr. S. Yu. Medvedev for the computations of the Alfvén continuum with KINX code, Dr. J. Urban for providing the results of the FAFNER code and Dr. A. G. Elfimov for a discussion of the NBI effects. This work was supported by grants of the Czech Science Foundation GA16-25074S, GA14-35260S (Thomson scattering measurement), GA16-24724S (NBI modelling), GA15-10723S (electronics of the horizontal probe) and co-funded by MEYS projects number 8D15001 and LM2015045. This work has been carried out within the framework of the EUROfusion Consortium and has received funding from the Euratom research and training programme 2014–2018 under grant agreement No 633053. The views and opinions expressed herein do not necessarily reflect those of the European Commission. Access to computing and storage facilities owned by parties and projects contributing to the National Grid Infrastructure MetaCentrum provided under the programme ‘Projects of Large Research, Development, and Innovations Infrastructures’ (CESNET LM2015042), is appreciated. Research and data analysis done by Kurchatov team for chapter 3 were funded by Russian Science Foundation, Project 14-22-00193. The work of AVM was partly supported by the Competitiveness Programme of NRNU MEPhI.

ORCID iDs

J. Krbec  <https://orcid.org/0000-0002-3780-6257>

J. Horacek  <https://orcid.org/0000-0002-4276-3124>

References

- [1] Winsor N. *et al* 1968 *Phys. Fluids* **11** 2448
- [2] Diamond P.H. *et al* 2005 *Plasma Phys. Control. Fusion* **47** R35
- [3] Hahm T.S. *et al* 1999 *Phys. Plasmas* **6** 922
- [4] Tynan G.R. *et al* 2016 *Plasma Phys. Control. Fusion* **58** 044003
- [5] Askinazi L.G. *et al* 2017 *Plasma Phys. Control. Fusion* **59** 014037
- [6] Cziegler I. *et al* 2013 *Phys. Plasmas* **20** 055904
- [7] Wang G. *et al* 2013 *Phys. Plasmas* **20** 092501
- [8] Ido T. *et al* 2006 *Plasma Phys. Control. Fusion* **48** S41
- [9] Melnikov A.V. *et al* 2015 *J. Phys.: Conf. Ser.* **591** 012003
- [10] Xu Y. *et al* 2011 *Plasma Phys. Control. Fusion* **53** 095015
- [11] Berk H. *et al* 2006 *Nucl. Fusion* **46** S888
- [12] Nazikian R. *et al* 2008 *Phys. Rev. Lett.* **101** 185001
- [13] Fu G.Y. 2008 *Phys. Rev. Lett.* **101** 185002
- [14] Nagashima Y. *et al* 2005 *Phys. Rev. Lett.* **95** 095002
- [15] Melnikov A.V. *et al* 2017 *Nucl. Fusion* **57** 072004
- [16] Wahlberg C. *et al* 2016 *Plasma Phys. Control. Fusion* **58** 075014
- [17] Smolyakov A.I. *et al* 2010 *Nucl. Fusion* **50** 054002
- [18] Bashir M.F. *et al* 2014 *Phys. Plasmas* **21** 082507
- [19] Wahlberg C. 2009 *Plasma Phys. Control. Fusion* **51** 085006
- [20] de Meijere C.A. *et al* 2014 *Plasma Phys. Control. Fusion* **56** 072001
- [21] Matsunaga G. 2012 *Proc. 39th EPS Conf. on Plasma Physics (Stockholm, Sweden, 2–6 July 2012) Europhysics Conf. Abstracts vol 36F P2.062* (<http://ocs.ciemat.es/epsicpp2012pap/pdf/P2.062.pdf>)
- [22] Melnikov A.V. *et al* 2006 *Plasma Phys. Control. Fusion* **48** S87
- [23] Conway G. *et al* 2008 *Plasma Phys. Control. Fusion* **50** 055009
- [24] Simon P. 2016 *Plasma Phys. Control. Fusion* **58** 045029
- [25] Angelino P. *et al* 2008 *Phys. Plasmas* **15** 062306
- [26] Gao Z. 2011 *Plasma Sci. Technol.* **13** 15
- [27] Leering S. *et al* 2012 *Phys. Rev. Lett.* **109** 165001
- [28] Melnikov A.V. *et al* 2015 *Nucl. Fusion* **55** 063001
- [29] Kolesnichenko Y.I. *et al* 2013 *Plasma Phys. Control. Fusion* **55** 125007
- [30] Gao Z. *et al* 2008 *Phys. Plasmas* **15** 072511
- [31] Panek R. *et al* 2016 *Plasma Phys. Control. Fusion* **58** 014015
- [32] Adánek J. *et al* 2010 *Contrib. Plasma Phys.* **50** 854
- [33] Adánek J. *et al* 2016 *Rev. Sci. Instrum.* **87** 043510
- [34] Adánek J. *et al* 2014 *Contrib. Plasma Phys.* **54** 279
- [35] Schrittwieser R. *et al* 2002 *Plasma Phys. Control. Fusion* **44** 567
- [36] Garcia O.E. *et al* 2007 *Plasma Phys. Control. Fusion* **49** B47
- [37] Muller H.W. *et al* 2011 *Nucl. Fusion* **51** 073023
- [38] Hidalgo C. *et al* 1991 *Nucl. Fusion* **31** 1471
- [39] Markovic T. *et al* 2016 *Nucl. Fusion* **56** 092010
- [40] Aftanas M. *et al* 2012 *Rev. Sci. Instrum.* **83** 10E350
- [41] Bohm P. *et al* 2014 *Rev. Sci. Instrum.* **85** 11E431
- [42] Zajac J. *et al* 2012 *Rev. Sci. Instrum.* **83** 10E327
- [43] Gao Z. 2013 *Phys. Plasmas* **20** 032501
- [44] Kramer-Flecken A. *et al* 2009 *Plasma Phys. Control. Fusion* **51** 015001
- [45] Markovsky I. *et al* 2007 *Signal Process.* **87** 2283
- [46] Beall J.M. *et al* 1982 *J. Appl. Phys.* **53** 3933
- [47] Kim Y.C. *et al* 1979 *IEEE Trans. Plasma Sci.* **PS-7** 120
- [48] van Milligen B.P. *et al* 1995 *Phys. Plasmas* **2** 3017
- [49] Urban J. 2010 *Plasma Phys. Control. Fusion* **52** 045008
- [50] Speth E. 1989 *Rep. Prog. Phys.* **52** 57
- [51] Elfimov A.G. *et al* 2015 *Phys. Plasmas* **22** 114503
- [52] Elfimov A.G. *et al* 2017 *Phys. Lett. A* **381** 3066–70
- [53] Degtyarev L.M. *et al* 1997 *Comput. Phys. Commun.* **103** 10

■ A.3 Geodesic mode instability driven by electron and ion fluxes during neutral beam injection in tokamaks



Geodesic mode instability driven by electron and ion fluxes during neutral beam injection in tokamaks



F. Camilo de Souza^a, A.G. Elfimov^{a,*}, R.M.O. Galvão^a, J. Krbec^{b,c}, J. Seidl^b, J. Stöckel^b, M. Hron^b, J. Havlicek^b, K. Mitosinkova^{b,d}

^a Institute of Physics, University of São Paulo, São Paulo, 05508-090, Brazil

^b Institute of Plasma Physics of the CAS, Prague, Czech Republic

^c Faculty of Nuclear Sciences and Physical Engineering, Czech Technical University, Prague, Czech Republic

^d Faculty of Mathematics and Physics, Charles University in Prague, Prague, Czech Republic

ARTICLE INFO

Article history:

Received 20 January 2017

Received in revised form 20 July 2017

Accepted 22 July 2017

Available online 27 July 2017

Communicated by F. Porcelli

Keywords:

Tokamak

Geodesic acoustic modes

Kinetic theory

Instability

Landau damping

ABSTRACT

The effect of a minor concentration of energetic particles produced by parallel NB injection on Geodesic Acoustic Modes (GAM) spectrum is analyzed using fully kinetic equation. It is found that the GAM frequency is reduced by the effective mass renormalization due to that new energetic GAM appears with higher frequency. The electron current in combination with NB driven ion flow, modeled by shifted Maxwell distribution, may overcome the ion Landau damping thus resulting in the GAM instability when electron current velocity is larger than the effective parallel GAM phase velocity $Rq\omega$. Qualitative agreement of the theory with co/counter NB injection experiments in COMPASS tokamak is demonstrated.

© 2017 Elsevier B.V. All rights reserved.

1. Introduction

Geodesic Acoustic Modes (GAM) are $M = 0$, $N = 0$ axisymmetric toroidal modes combined with $M = \pm 1$, ± 2 poloidal side-bands and defined by the electron and anisotropic ion pressure perturbations with the frequency [1] $\omega_G^2 \approx (7T_i/2 + 2T_e)/R_0^2 m_i$. These modes may be important for plasma transport as it has been theoretically discussed [2] and observed in experiments [3–9]. Furthermore, they may be useful as a diagnostic tool to indicate L–H confinement transition [4] in tokamaks. The nature of the experimentally observed geodesic eigenmodes is still not clear and several different mechanisms might be responsible for their dispersion and manifest themselves in different conditions. Eigenmodes in the geodesic frequency range have been experimentally detected under a wide range of conditions in various tokamaks during ohmic discharges [4,5], but they may also appear during neutral beam (NB) heating [6–9], mainly indicating instability in counter injection in comparison with balanced injection [8]. Early developed theory of GAM instability driven by NB injection had been referred to some pitch angle inhomogeneous distribution [10–12] in the velocity space. Two kinds of geodesic modes were found,

standard GAM and geodesic mode driven by energetic particles (EGAM). In typical plasma conditions, the NB velocity is less than electron thermal velocity $v_{Te} \gg V_{NB}$, this is a reason for the NB velocity to slide down to the critical velocity $V_0 \approx 5.5Z_e^{1/3} \sqrt{T_e/m_b}$ (or to critical energy [13]) due to collisions with electrons without change of pitch angle. In standard cases, the critical velocity is larger than the GAM phase velocity of sidebands $V_0 \gg Rq\omega$ and the GAM instability [10–12] may appear if the injection pitch angle is large $V_{0\perp}/V_0 > 1/2$. For NB velocities of the order of the critical one, $v \approx O(V_0)$, and lower angle, scattering of NB ions on electrons and collision with plasma ions induce strong beam diffusion and scattering forming “bump on tail like” distribution $F_b \propto \exp[-(v_{\parallel} - V_0)^2/2v_{Tb}^2]$ for ions, having the bump ion temperature comparable to the critical energy $v_{Tb}^2 \leq O(V_0^2)$ that stimulates rotation of the main plasma in the same direction. The bump on tail formation is confirmed by TRANSP code calculations for the NB heated plasmas [14]. The bump model has been used in theoretical analyses of GAM instabilities [12,15] driven by two balanced parallel beams producing the instability due to inversed fast ion Landau damping. Physics of balanced and co/counter injection are substantially different; for example, direct effect of balanced beam circulation $\omega_{bal}^2 = V_0^2/R_0^2 q^2$ may generate GAM with the same frequency for enough large beam density [12], but that effect is ab-

* Corresponding author.

E-mail address: elifimov@if.usp.br (A.G. Elfimov).

sent for unbalanced injection, as well as direct inversed Landau damping due to poloidal symmetry of GAM oscillations.

Recently, it has been theoretically shown that GAMs may be driven by an electric current with velocity along the magnetic field in combination with the diamagnetic drift [16,17] and/or rotation [18]. The instability occurs only when the electron current velocity is higher than the GAM phase velocity of sidebands, which is much larger than ion thermal velocity. Here, we extend previous studies [16,17] and investigate whether the parallel particle fluxes can drive the GAMs via coupling due to a cross term of the ion flow and the parallel current or this instability may be directly driven by the parallel neutral beam injection. Finally, comparison with NB experiments in COMPASS tokamak [9,19] will be discussed.

2. Theoretical results

The kinetic treatment of the GAM type modes is fully performed by taking into account the dynamics of ion and energetic particles provided by neutral beam injection in tokamak in the large aspect ratio approach $R_0 \gg a$ with quasi-toroidal set of coordinates (r, ϑ, ζ) and the circular surfaces ($R = R_0 + r \cdot \cos \vartheta$, $z = r \sin \vartheta$), which are formed by the magnetic field with toroidal and poloidal components, $B_\zeta = B_0 R_0 / R$, $B_\vartheta = r B_\zeta / q R_0$ where B_0 is magnetic field in magnetic axis. The dimensionless drift kinetic equation for any specie α electron, ion or beam particles is used in the form

$$\frac{\partial f_\alpha}{\partial \vartheta} - \frac{i\Omega f_\alpha}{w} = \frac{e_\alpha F_\alpha}{m_\alpha w} \left[\frac{(w - v_{0\alpha}) E_3}{k_0 v_{T\alpha}^2} - \frac{(w^2 - v_{0i}^2 t_c + u^2/2)}{v_{T\alpha} \omega_{c\alpha} k_0 R} E_1 \sin \vartheta \right]. \quad (1)$$

Here, $E_{1,3}$ are radial and parallel components of wave field, $\Omega = \omega R_0 q / v_{T\alpha}$ is the normalized wave frequency and $\omega_{c\alpha} = e_\alpha B / m_\alpha c$ are cyclotron frequencies, $k_0 = h_\vartheta / r = 1/qR$ is the parallel wave vector, $h_\vartheta = B_\vartheta / B_0$ is magnetic field inclination, $w = v_\parallel / v_{T\alpha}$ and $u = v_\perp / v_{T\alpha}$ are the normalized space velocities, $v_{T\alpha} = \sqrt{T_\alpha / m_\alpha}$ is particle thermal velocities. A shifted Maxwell distribution $F_\alpha = F_{M\alpha}|_{w=w-v_{0\alpha}}$ with $v_{0\alpha} = V_{0\alpha} / v_{T\alpha}$ is assumed for any specie having the respective parallel equilibrium velocity $V_{0\alpha}$ accounting centrifugal effect $t_c \approx T_e / (T_e + T_i)$. Taking $E_3 = E_s \sin \vartheta + E_c \cos \vartheta$ and $f_\alpha = f_{s\alpha} \sin \vartheta + f_{c\alpha} \cos \vartheta$, the solution for (1) is found

$$\begin{aligned} f_{s\alpha} &= -\frac{ie_\alpha \Omega q (w^2 - t_c v_{0i}^2 + u^2/2) F_\alpha E_1}{\omega_{c\alpha} m_\alpha v_{T\alpha} (\Omega^2 - w^2)} \\ &\quad + \frac{e_\alpha q R F_\alpha (i\Omega E_s - w E_c)}{T_\alpha (\Omega^2 - w^2)} (w - v_{0\alpha}), \\ f_{c\alpha} &= -\frac{e_\alpha q w (w^2 - t_c v_{0i}^2 + u^2/2) F E_1}{\omega_{c\alpha} m_\alpha v_{T\alpha} (\Omega^2 - w^2)} \\ &\quad + \frac{e_\alpha q R F (i\Omega E_c + w E_s)}{T_\alpha (\Omega^2 - w^2)} (w - v_{0\alpha}) \end{aligned} \quad (2)$$

Integrating (2) for each species, we have:

$$\begin{aligned} \tilde{n}_{\alpha s} &= \sqrt{2} \frac{e_\alpha n_\alpha R_0 q}{4 m_\alpha v_{T\alpha}^2} \left\{ \frac{i v_{T\alpha}}{R_0 \omega_{c\alpha}} [(Z_+ - Z_-) (\Omega^2 + 1 - t_c v_{0i}^2)] \right. \\ &\quad + 2\sqrt{2} \Omega E_1 \\ &\quad + [(\Omega + v_{0\alpha}) Z_+ - (\Omega - v_{0\alpha}) Z_- + 2\sqrt{2}] E_c \\ &\quad \left. + i [(\Omega - v_{0\alpha}) Z_- + (\Omega + v_{0\alpha}) Z_+] E_s \right\} \\ \tilde{n}_{\alpha c} &= \sqrt{2} \frac{e_\alpha n_\alpha R_0 q}{4 m_\alpha v_{T\alpha}^2} \left\{ [(\Omega - v_{0\alpha}) Z_- - (\Omega + v_{0\alpha}) Z_+ - 2\sqrt{2}] E_s \right. \end{aligned}$$

$$\begin{aligned} &\quad + i [(\Omega + v_{0\alpha}) Z_+ + (\Omega - v_{0\alpha}) Z_-] E_c \\ &\quad \left. - \frac{v_{T\alpha}}{R_0 \omega_{c\alpha}} [(Z_+ + Z_-) (\Omega^2 + 1 - t_c v_{0i}^2) - 2\sqrt{2} v_{0\alpha}] E_1 \right\} \quad (3) \end{aligned}$$

Here, $Z_\pm = \frac{1}{\sqrt{\pi}} \int_{-\infty}^{\infty} dt \exp(-t^2)/(x-t)$ is the dispersion function where $x = (v_{0\alpha} \pm \Omega) / \sqrt{2}$.

Using the respective distribution in Eq. (2) and the radial magnetic drift velocity $W_{r\alpha} = -[w^2 - v_{0i}^2 T_e / (T_i + T_e) + u^2/2] v_{T\alpha}^2 \sin \vartheta / R \omega_{c\alpha}$, where the term $v_{0i}^2 T_e / (T_i + T_e) v_{T\alpha}^2$ is responsible for centrifugal correction of the magnetic drift via poloidal variation of electrostatic potential over magnetic surface, we get the θ -averaged radial currents:

$$\begin{aligned} \langle \tilde{j}_r^\alpha \rangle &= -\frac{ie_\alpha^2 n_\alpha q}{8 m_\alpha \omega_{c\alpha}} \left\{ [\sqrt{2} (\Omega^2 + 1 - v_{0i}^2 t_c) ((\Omega + v_{0\alpha}) Z_+ \right. \\ &\quad - (\Omega - v_{0\alpha}) Z_-)] E_s \\ &\quad - i [8 + 4\Omega^2 + \sqrt{2} (\Omega^2 + 1 - v_{0i}^2 t_c) ((\Omega + v_{0\alpha}) Z_+ \\ &\quad - (\Omega - v_{0\alpha}) Z_-)] E_c \\ &\quad + \frac{v_{T\alpha}}{R \omega_{c\alpha}} [\sqrt{2} (Z_+ - Z_-) (2\Omega^2 + \Omega^4 + 2 - (\Omega^2 + 1) v_{0i}^2 t_c) \\ &\quad \left. + 4(\Omega^2 + v_{0\alpha}^2 - 2v_{0i}^2 t_c + 3)\Omega] E_1 \right\} \quad (4) \end{aligned}$$

We have used the condition $v_{0e} > v_{0b} \gg \omega R_0 q / v_{Ti} > v_{0i}$ in Eq. (2) to obtain the simplified density perturbations for each species [18] and the electron density perturbations become:

$$\begin{aligned} \tilde{n}_{es} &= (e_i n_0 R_0 q / T_e) [\sqrt{\pi \mu / 2 \tau_e} v_{0e} E_s - E_c], \\ \tilde{n}_{ec} &= (e_i n_0 R_0 q / T_e) [\sqrt{\pi \mu / 2 \tau_e} v_{0e} E_c + E_s] \end{aligned} \quad (5)$$

where $\mu = m_e / m_i$, $\tau_e = T_e / T_i$. The corresponding simplified expressions for ions are

$$\begin{aligned} \tilde{n}_{is} &= \frac{e_i n_{0i} R_0 q}{m_i v_{Ti}^2} \left\{ 2i \frac{v_{0i}}{\Omega^3} E_s - \frac{E_c}{\Omega^2} - \frac{i v_{Ti}}{\omega_{ci} R \Omega} \left[2 + v_{0i}^2 (1 - t_c) \right. \right. \\ &\quad \left. \left. + \frac{(7v_{0i}^2 + 1)}{\Omega^2} \right] E_1 \right. \\ &\quad \left. + \frac{\sqrt{2\pi}}{2} \left[i\Omega E_c - \frac{v_{Ti}}{\omega_{ci} R} (\Omega^2 + 1) E_1 \right] \exp\left(-\frac{\Omega^2}{2}\right) \right\}; \quad (6a) \end{aligned}$$

$$\begin{aligned} \tilde{n}_{ic} &= \frac{e_i n_{0i} R_0 q}{m_i v_{Ti}^2} \left\{ \frac{E_s}{\Omega^2} + i \frac{2v_{0i}}{\Omega^3} E_c - 4 \frac{v_{Ti}}{\omega_{ci} R} \frac{v_{0i}}{\Omega^2} E_1 \right. \\ &\quad \left. - \frac{\sqrt{2\pi}}{2} i\Omega E_s \exp\left(-\frac{\Omega^2}{2}\right) \right\} \quad (6b) \end{aligned}$$

In the limit $v_{0b} \gg \Omega$, the bump particles density perturbations are reduced to the form:

$$\begin{aligned} \tilde{n}_{bs} &= \left(\frac{e_i n_{0b} R_0 q}{m_i v_{Ti}^2} \right) \left\{ \frac{i\Omega v_{Ti}}{\omega_{ci} R_0 v_{0b}^2} \left[1 - v_{0i}^2 t_c + \frac{(\Omega^2 + v_{0b}^2)}{\tau_b} \right] E_1 \right. \\ &\quad - \frac{E_c}{v_{0b}^2} + \frac{\sqrt{2\pi}}{4\sqrt{\tau_b^3}} \left[(\Omega - v_{0b}) (iE_c + E_s) \right. \\ &\quad \left. - \frac{v_{Ti}}{\omega_{ci} R_0} (\tau_b + \Omega^2) E_1 \right] \exp\left(-\frac{(\Omega - v_{0b})^2}{2\tau_b}\right) \right\} \quad (7a) \end{aligned}$$

$$\begin{aligned} \tilde{n}_{bc} &= \left(\frac{e_i n_{0b} R_0 q}{m_i v_{Ti}^2} \right) \left\{ \frac{i v_{Ti}}{\omega_{ci} R_0 \tau_b} \left(\frac{\Omega^2}{v_{0b}} + v_{0b} + \frac{\tau_b}{v_{0b}} \right) E_1 + \frac{E_s}{v_{0b}^2} \right. \\ &\quad \left. + \frac{\sqrt{2\pi}}{4\sqrt{\tau_b^3}} \left[\frac{v_{Ti} (\tau_b + \Omega^2)}{\omega_{ci} R_0} E_1 + (v_{0b} - \Omega) (iE_s - E_c) \right] \right\} \end{aligned}$$

$$\times \exp\left(-\frac{(\Omega - v_{0b})^2}{2\tau_b}\right)\} \quad (7b)$$

where $\tau_b = T_b/T_i$. The equations for currents are simplified for each particle species in the same limits:

$$\langle \tilde{j}_r^e \rangle = \frac{e_i^2 q n_0}{m_i \omega_{ci}} \left[i \sqrt{\frac{\pi}{8}} \sqrt{\frac{\mu}{t_e}} v_{0e} E_s - (1 + v_{0i}^2 t_c / 2t_e) E_c \right]; \quad (8)$$

$$\langle \tilde{j}_r^i \rangle = \frac{e_i^2 n_{0i} q}{m_i \omega_{ci} \Omega} \left\{ i \left[(t_c - 3) v_{0i}^2 - 2 + i \frac{\sqrt{2\pi}}{4} \Omega^3 (\Omega^2 + 1) \right] \times \exp\left(-\frac{\Omega^2}{2}\right) \right\} E_c - v_{0i} \Omega E_s + \frac{v_{Ti} \Omega}{R_0 \omega_{ci}} \left[\left(\frac{7}{2} + \frac{23}{2\Omega^2} + 2v_{0i}^2 (2 - t_c) \right) - \sqrt{2\pi} i \frac{\Omega}{2} \left(\frac{\Omega^4}{2} + \Omega^2 + 1 \right) \exp\left(-\frac{\Omega^2}{2}\right) \right] E_1 \}; \quad (9)$$

$$\langle \tilde{j}_r^b \rangle = \frac{e_i^2 n_{0b} q}{2m_i \omega_{ci} \Omega} \left\{ \frac{v_{Ti} \Omega^2}{\omega_{ci} R_0 \tau_b} [v_{0b}^2 + \Omega^2 + 3\tau_b] E_1 + i \Omega E_c - \frac{\sqrt{2\pi}}{4\sqrt{\tau_b}} \left[\left(\frac{\Omega^2}{\tau_b} + 1 \right) (v_{0b} - \Omega) \right] (iE_s - E_c) + i \frac{v_{Ti} \Omega}{\omega_{ci} R_0 \tau_b} (\Omega^4 + 2\tau_b (\Omega^2 + \tau_b)) E_1 \right\} \times \exp\left(-\frac{(\Omega - v_{0b})^2}{2\tau_b}\right)\} \quad (10)$$

Furthermore, using the quasi-neutrality condition together with the electron density in Eqs. (5)–(7), we find the electric field amplitudes $E_{s,c}$, which have to be used in calculations of the radial currents. In this case, the sum of the radial components of currents together with the ion radial polarization current gives the GAM resonance condition $\langle \tilde{j}_r^e + \tilde{j}_r^i + \tilde{j}_r^b \rangle + j_p = 0$, where $j_p = -i\omega c^2 E_1 / 4\pi c_A^2$ is the ion polarization current and $c_A = B / \sqrt{4\pi n_i m_i}$. Next, we get the equation for the GAM continuum frequency from the real part of the radial current:

$$\frac{\Omega^2}{q^2} = \frac{7}{2} + 4v_{0i}^2 + \frac{t_e [(2\Omega^2 + \Omega^2 v_{0i}^2 + 8 + 12v_{0i}^2)(\Omega^2 - \tau_e) + 12\tau_e v_{0i}^2]}{[(\Omega^2 - \tau_e)^2 - v_{0i}^2 \tau_e^2 / \Omega^2]} + \frac{23 + 59v_{i0}^2}{(\Omega^2 - \tau_e)} - \frac{[\Omega^6 + (v_{0b}^2 + 3\tau_b + \tau_e)\Omega^4 - (v_{0b}^2 + \tau_b - 4)\Omega^2 + 4\tau_b \tau_e] n_b}{2\tau_b (\Omega^2 - \tau_e)} \quad (11)$$

where $n_b = n_{0b}/n_{0i}$ is relative beam density.

In the limit $\Omega^2 \gg \tau_e$ in Eq. (11), we obtain the GAM frequency modified by beam:

$$\frac{\Omega_G^2}{q^2} = \left(\frac{\omega_G^2 R_0^2}{v_{Ti}^2} \right) \approx \frac{[\frac{7}{2} + 2\tau_e + 4v_{0i}^2 - \frac{n_b \tau_e}{\tau_b} (2\tau_e + \tau_b + \tau_e^2 + v_{0i} v_{0b})]}{[1 + n_b q^2 (v_{0b}^2 + 3\tau_b + q^2 \tau_e + 7q^2/4)/2\tau_b]} \quad (12)$$

In the case of $q^2 \gg 1$, we found that the GAM frequency may be substantially reduced by NB energetic particles due to “energetic particle factor” $[1 + n_b q^2 (v_{0b}^2 + 3\tau_b + q^2 \tau_e + 7q^2/4)/2\tau_b]$. Similar effect was discussed in theoretical [17] and numerical calculations

[12]. From the imaginary part of the radial current, we obtain the increment of the GAM instability:

$$\gamma \approx \sqrt{\frac{\pi}{2}} \frac{v_{Ti} \tau_e q}{2R_0} \left\{ \frac{\sqrt{\tau_e \mu}}{\Omega^2} v_{0e} \times \left[4v_{i0} + v_* - (\Omega^2 + 2\tau_e + 2) \frac{n_b v_{0b}}{2\tau_b} \right] - \frac{1}{\tau_e} \left[\frac{\Omega^4}{2} + (2\tau_e + 1)\Omega^2 + 3\tau_e^2 + 4\tau_e + 1 \right] \right\} \times \exp\left(-\frac{\Omega^2}{2}\right)\} \quad (13)$$

where we formally add the drift term $v_* = (2 + 2d \ln T_i / d \ln n_i + 3t_e) \rho_{Li} / d_i h_p$, which is obtained in our previous theoretical studies [16,17] (for example, the first term in Eq. (11) of Ref. [16]). In difference with our previous study [18], the instability that is driven by ion rotation crossed with electron current velocity is slightly reduced by small parameter $(\Omega^2 + 2\tau_e + 4)n_b v_{0b} / 2\tau_b$ related to the bump due to $\tau_b > \Omega^2 \gg \tau_e > 1 \gg n_b$. We note that part of Landau damping that is produced by the bump on tail is ignored in Eq. (13), because it is exponentially small due to approach $|v_{0b} \pm \Omega| \gg 1$.

It should be noted that there is one more geodesic mode named EGAM, which was earlier discussed in Refs. [10–12], that may be found from the set of Eqs. (5), (6), (8), (9) together with Eqs. (3), (4) for energetic particles. To avoid complex numerical calculations of this set, we suggest that the mode frequency stays near the bump circulation frequency. We introduce normalized difference between the new EGAM and bump circulation frequency $\delta = \omega_{EG} R q / V_0 - 1$ where $\delta^2 \ll 1$ in dependence from the standard GAM that is defined by the dimensionless distance from the bump circulation $\Delta = 1 - \Omega_G^2 (1 - 2i\gamma / \Omega_G) / V_0^2$ where $|\Delta| < 1$.

In this case, the energetic ion current is

$$\langle \tilde{j}_r^b \rangle = i \frac{e_i^2 n_{0b} q}{2m_i \omega_{ci} \tau_b^2 \Omega} \left\{ v_{0b}^3 \delta \left[v_{0b} (\delta + 2) \delta - i \frac{\sqrt{2\pi} \tau_b}{4} \right] (iE_s - E_c) + 5 \frac{v_{Ti} v_{0b}^4}{\omega_{ci} R_0} \left[v_{0b}^2 (\delta + 1) \delta + 2\delta^2 + \frac{1}{10} \delta - \frac{7}{20} \tau_b \right] - i \frac{\sqrt{2\pi} \tau_b}{20} \right\} E_1 \} \quad (14)$$

Combining it with Eqs. (5)–(6), (8)–(9) we obtain the simplified dispersion equation for $q^2 \gg 1$

$$\delta^4 + \delta^3 + \frac{\delta^2}{2} + \frac{\delta}{10} + \eta [1 - (1 + \delta)^2 - \Delta] = 0 \quad (15)$$

where the parameter $\eta = \frac{2}{5} \frac{\tau_b^2}{q^2 n_b v_{0b}^4}$ was used in the limits $0.1 < \eta < 1$. The bump ion energy was assumed to be large enough to have an oscillating solution with small increment or decrement. For small δ , two solutions are found (shown in Fig. 1 for $\eta = 0.1$ –0.4). In the case of the bump resonance $\Delta = 1 - \omega_G R_0 q / V_0 = 0$, the first mode is $\omega_1 = V_0 / R_0 q$, which branch has prolongation to the GAM in Eq. (12) and second mode (assumed as EGAM) has frequency $\omega R_0 q / V_0 - 1 \approx 0.24\eta^{2/3} + 1.26\eta^{1/3} - 0.37$ with increment (or decrement) sign opposite to the first mode shown in Eq. (13). Both modes begin to be split or couple at the frequency defined by equations $\delta_{\text{coupl}} = \omega_{\text{coupl}} R_0 q / V_0 - 1 \approx 0.18\eta^{2/3} + 0.76\eta^{1/3} - 0.51 - 0.026/\eta^{1/3}$ and $\Delta_{\text{min}} = (V_0^2 - \Omega_G^2) / V_0^2 \approx -\delta_{\text{coupl}} (1 - 1/\eta + \delta_{\text{coupl}})$. Complete numerical analysis of this case using Eqs. (3)–(4) is under development and results will be published elsewhere.

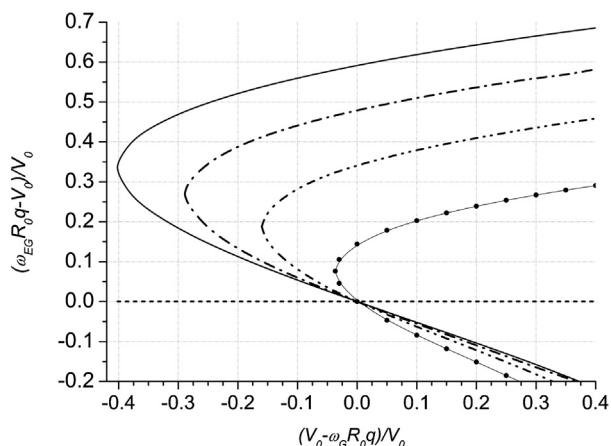


Fig. 1. Plot of normalized geodesic frequencies (EGAM) modified by energetic ions in dependence over normalized difference between energetic ion circulation and standard GAM frequencies for $\eta = 0.1$ (dotted line), 0.2 (dash-dot-dot), 0.3 (dash-dot) and 0.4 (solid lines).

3. GAM observation during NB heating in COMPASS tokamak

COMPASS ($R = 0.56$ m, $a = 0.2$ m) is a tokamak with ITER-like shape diverted plasma configuration [20]. Magnetic pick up coils [9] was supplied for measurement of poloidal and radial magnetic field fluctuations with 2 MHz sampling rate, as well as two poloidal rings of Mirnov coils and a set of saddle loops covering the whole toroidal angle. There are two pneumatic reciprocating probe manipulators [9], which are equipped by a combination of Langmuir probes measuring floating potential V_{fl} and/or ion saturation current I_{sat} , and ball-pen probes providing fast measurement of a plasma potential, as well as the electron temperature together with two high resolution Thomson scattering systems for core and edge plasmas. GAM like oscillations ($N = 0, M = 0, \pm 1, \pm 2$) in the frequency band $f = 30\text{--}37$ kHz were detected by the magnetic and Langmuir probes [9] with high coherence level (at the position $\Delta r \approx -1\text{--}2$ cm deep from the last magnetic surface) during ohmic discharges shown in Fig. 2 in deuterium plasmas ($B_t = 1.15$ T, $I_p = 190$ kA, elongation $\kappa = 1.8$, $n_0 = 4\text{--}5 \cdot 10^{19}$ m $^{-3}$, $T_{e0} = 800\text{--}900$ eV). The GAM frequency in Eq. (12) corresponds to the theoretically predicted one [1] assuming the ion temperature $T_{ia} \approx T_{ea} = 30\text{--}35$ eV at the border. Series of discharges with co (similar to #11035, 12 A, $U_{NB} = 40$ keV, $P_{NB} = 360$ kW) and counter NB injection (#11502, 12 A, $U_{NB} = 40$ keV, $P_{NBI} \sim 370$ kW) is used to study NB heating effect on GAMs presented in Fig. 2. Due to temperature and rotation increasing with NB application, it is observed that the GAM frequency increases for co and

counter injection in Fig. 3. Dramatic changes in the GAM amplitude occur during the NB injection period $t_{NB} = 1090\text{--}1170$ ms. While the GAM amplitude increases moderately during the counter injection, the GAM instability is strongly suppressed by the co-injection, as it is shown in Fig. 3, possibly, due rotation. Here, we note that there is no phase resonance between the beam circulation and GAM frequency $V_{NB} = \sqrt{2U_{NB}/m_i} \gg R_0 q \omega_G$.

4. Discussion

After NB application, the ion temperature increases rapidly for counter and co-injection with $\Delta(T_i)/(T_i) \approx 50\%$ and 62% , respectively. This is obtained from neutral particle analyzer and is confirmed by the diamagnetic signal variation in Fig. 2 and Thomson scattering diagnostics during initial period $\Delta t = 10$ ms. The effect is accompanied by the respective GAM frequency increase $\Delta f/f \approx 21\%$ and 28% . The frequency change $\Delta f/f \approx 22\%$ and 26% may be explained by the GAM frequency dependence in Eq. (12), using the respective estimates for the electron and ion temperature variation and assuming that there is no substantial fast ion density maximum accumulation. In fact, this variation is about $n_b \approx 3\text{--}3.5\%$ for 12 A NB injection at the end of the initial period $\Delta t \approx 10$ ms, giving possibility to ignore the bump effect $n_b V_0^2/m \ll T_i + T_e$ in the frequency estimation. To explain the GAM amplitude variation, we propose that it should be proportional to the instability increment in Eq. (13). In the ohmic stage, the observed instability may be driven by the cross term between the electron velocity and ion counter rotation (or/and diamagnetic drift [16,17]) with increment $\gamma \propto [V_{e0}(V_{oi} + V_*)/v_{Ti}v_{Te} - 0.03 \exp(2 - q^2/2)]$. The condition for the instability (inversed electron Landau damping effect) is to have large electron current speed $V_{e0} \gg Rq\omega_G > v_{Ti}$, which is satisfied for the entire COMPASS cross-sections calculated from the current profile by EFIT code. For counter rotation, the electron and ion velocities have the same direction and their cross term might drive the instability, whereas this term may strongly reduce it for co-rotation when the velocity has the order of the ion drift velocity $V_{i0} \approx \rho_{Li}v_{Ti}/d\tau h_\theta$.

There are two reasons to explain the GAM amplitude modification during NB injection. The first one is changing profiles of the electron distribution function and another is modification of the rotation velocity. For counter NB injection, the electron distribution is modified by the beam [15] in the velocity interval $[V_0 - V_{NB}]$ that reduces the population of slide away electrons due to electric field inverting and making shifted electron distribution more peaked, creating the better distribution for inverse Landau damping in comparison with Maxwell distribution. For co injection, the electron distribution inclination is diminished at the phase res-

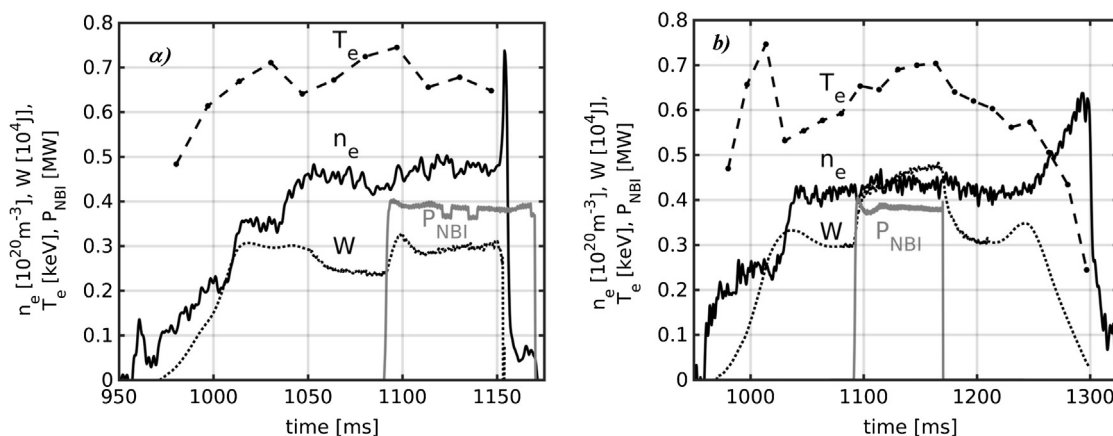


Fig. 2. Temporal evolution of electron temperature, line density and diamagnetic energy during counter (#11502, a) and co NB injection (#11035, b).

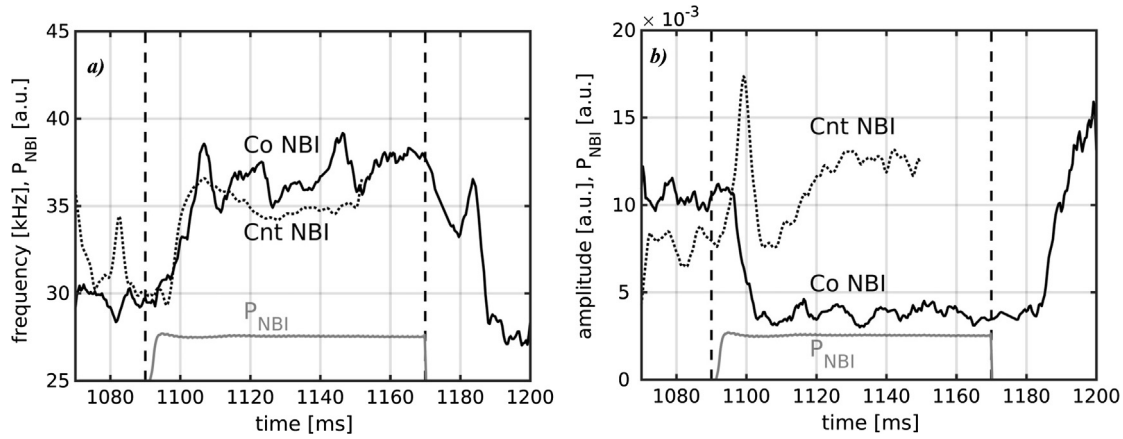


Fig. 3. Temporal evolution of the frequency (a) and amplitude (b) of magnetic probe signals during counter and co NB injection.

onance due to NB heating of the electrons moving in opposite direction.

Next, we discuss effect of rotation driven by NB injection on GAM stability. The bump formation by the beam is complete after a time delay of the order of the slowing down time [15] $t_s \approx 6.3 \cdot 10^8 AT_e/Z_{ef}n_0 \ln \Lambda \sim 0.3$ ms from beginning of the NB injection. After this delay, the beam momentum (order of $n_b n_0 V_0$) begins to transfer this additional momentum to the main plasma due to ion-ion collisions [15] increasing or reducing plasma rotation by the value $V_{ad} \geq n_b |V_0|$. In this case, the increment in Eq. (13) should be corrected with $V_{ad} \approx n_b V_0$

$$\gamma \propto \frac{V_{oe}}{v_{Te}} \left\{ 4V_{0i} + v_{Ti} v_* + n_b V_0 [4 - (\Omega^2 + 2\tau_e + 2) T_i / 2T_b] - \frac{\Omega^2}{\tau_e} \left[\frac{\Omega^4}{2} + (2\tau_e + 1)\Omega^2 + 3\tau_e^2 + 4\tau_e + 1 \right] \exp\left(-\frac{\Omega^2}{2}\right) \right\}$$

Now, it is clear that the counter injection ($V_0 > 0$) increases the increment because direct bump effect is small due to $T_i/T_b \ll 1$ and co-injection reduces the increment. Comparing the GAM amplitudes for counter and co injections in Fig. 3, we may expect that the ion rotation momentum may substantially modify the GAM amplitude in the condition $n_b V_0 \approx v_{Ti} (4v_{0i} + v_{Ti} v_*) \geq 0.03 v_{Te} v_{Ti} / V_{0e} \exp(2 - q^2/2)$. Assuming the NB the density accumulation is $n_b \approx 3\%$, $V_0 \approx 5.5 v_{Ti}$ in the region where $q \approx 2.5$, we estimate $V_{e0}/v_{Te} \approx 0.1$ that is in the consistence with EFIT calculations for COMPASS.

Finally, we conclude that the theoretically found GAM instability, which is induced or suppressed by plasma ion flux, results from the cross term of the electron and ion fluxes induced by the NB injection that stays in qualitative agreement with COMPASS experiments.

Acknowledgements

The theoretical part of work was supported by CNPq (National Council of Scientific and Technological Development) contracts 480733/2013-9 and 306757/2015-0, Brazil and the COMPASS experiments were supported by Czech Science Foundation grant GA16-25074S and GA14-35260S and co-funded by MEYS projects number 8D15001 and LM2015045.

References

- [1] V.B. Lebedev, P.N. Yushmanov, P.H. Diamond, S.V. Novakovskii, A.I. Smolyakov, *Phys. Plasmas* 3 (1996) 3023.
- [2] P.H. Diamond, S.-I. Itoh, K. Itoh, T.S. Hahm, *Plasma Phys. Control. Fusion* 47 (2005) R35.
- [3] G.R. McKee, D.K. Gupta, R.J. Fonck, D.J. Schlossberg, M.W. Shafer, P. Gohil, *Plasma Phys. Control. Fusion* 48 (2006) S123.
- [4] G.D. Conway, B. Scott, J. Schirmer, M. Reich, A. Kendl, *Plasma Phys. Control. Fusion* 47 (2005) 1165.
- [5] A.V. Melnikov, L.G. Eliseev, S.V. Perfilov, S.E. Lysenko, R.V. Shurygin, V.N. Zenin, S.A. Grashin, L.I. Krupnik, A.S. Kozachek, R.Yu. Solomatina, A.G. Elfimov, A.I. Smolyakov, M.V. Ufimtsev, *Plasma Phys. Control. Fusion* 48 (2006) S87.
- [6] R. Nazikian, G.Y. Fu, M.E. Austin, H.L. Berk, R.V. Budny, N.N. Gorelenkov, W.W. Heidbrink, C.T. Holcomb, G.J. Kramer, G.R. McKee, M.A. Makowski, W.M. Solomon, M. Shafer, E.J. Strait, M.A. Van Zeeland, *Phys. Rev. Lett.* 101 (2008) 185001.
- [7] H.L. Berk, C.J. Boswell, D. Borba, A.C.A. Figueiredo, T. Johnson, M.F.F. Nave, S.D. Pinches, S.E. Sharapov, *Nucl. Fusion* 46 (2006) S888.
- [8] G. Matsunaga, K. Kamiya, K. Shinohara, N. Miyato, A. Kojima, A. Bierwage, in: 39th EPS Conference & 16th ICPP, Stockholm, Sweden, July 2012, P2.062.
- [9] J. Seidl, M. Hron, J. Adamek, P. Vondracek, J. Horacek, C. Hidalgo, A. Melnikov, L. Eliseev, T. Markovic, J. Stöckel, D. Basu, P. Hacek, J. Havlicek, M. Imříšek, K. Kovarik, V. Weinzettl, R. Panek, in: 42nd EPS Conference on Plasma Physics, Lisbon, Portugal, June 2015, P4.103.
- [10] G.Y. Fu, *Phys. Rev. Lett.* 101 (2008) 185002.
- [11] Z. Qiu, F. Zonca, L. Chen, *Plasma Phys. Control. Fusion* 52 (2010) 095003.
- [12] H. Wang, Y. Todo, T. Ido, M. Osakabe, *Phys. Plasmas* 22 (2015) 092507.
- [13] T.H. Stix, *Plasma Phys.* 14 (1972) 367.
- [14] B. Geiger, R. Dux, R.M. McDermott, S. Potzel, M. Reich, F. Rytter, M. Weiland, D. Wunderlich, M. Garcia-Munoz, *Rev. Sci. Instrum.* 84 (2013) 113502.
- [15] D. Zarzoso, X. Garbet, Y. Sarazin, R. Dumont, V. Grandgirard, *Phys. Plasmas* 19 (2012) 022102.
- [16] A.G. Elfimov, R.M.O. Galvão, A.I. Smolyakov, *Phys. Lett. A* 378 (2014) 800.
- [17] A.G. Elfimov, *Phys. Lett. A* 378 (2014) 3533.
- [18] A.G. Elfimov, F. Camilo de Souza, R.M.O. Galvão, *Phys. Plasmas* 22 (2015) 114503.
- [19] A.G. Elfimov, F. Camilo de Souza, R.M.O. Galvão, J. Krbec, J. Seidl, J. Stöckel, M. Hron, J. Havlicek, K. Mitošinkova, in: 43rd EPS Conference on Plasma Physics, 4–8 July 2016, Leuven, Belgium, in: *Europhysics Conference Abstracts*, vol. 40A, 2016, P2.038.
- [20] R. Panek, J. Adamek, M. Aftanas, P. Bílková, P. Böhm, F. Brochard, P. Cahyna, J. Cavalier, R. Dejarnac, M. Dimitrova, O. Grover, J. Harrison, P. Háček, J. Havlíček, A. Havránek, J. Horáček, M. Hron, M. Imříšek, F. Janky, A. Kirk, M. Komm, K. Kovařík, J. Krbec, L. Kripner, T. Marković, K. Mitošinková, J. Mlynář, D. Nайдenkova, M. Peterka, J. Seidl, J. Stöckel, E. Štefániková, M. Tomeš, J. Urban, P. Vondráček, M. Varavin, J. Varju, V. Weinzettl, J. Zajac, *Plasma Phys. Control. Fusion* 58 (2016) 014015.

Appendix B

Bibliography

- [Adamek et al., 2010] Adamek, J., Horacek, J., Müller, H., Rohde, V., Ionita, C., Schrittwieser, R., Mehlmann, F., Kurzan, B., Stöckel, J., Dejarnac, R., et al. (2010). Ball-Pen Probe Measurements in L-Mode and H-Mode on ASDEX Upgrade. *Contributions to Plasma Physics*, 50(9):854–859.
- [Adamek et al., 2014] Adamek, J., Horacek, J., Seidl, J., Müller, H., Schrittwieser, R., Mehlmann, F., Vondracek, P., Ptak, S., Team, C., Team, A. U., et al. (2014). Direct Plasma Potential Measurements by Ball-Pen Probe and Self-Emitting Langmuir Probe on COMPASS and ASDEX Upgrade. *Contributions to Plasma Physics*, 54(3):279–284.
- [Adamek et al., 2016] Adamek, J., Seidl, J., Komm, M., Weinzettl, V., Panek, R., Stöckel, J., Hron, M., Hacek, P., Imrisek, M., Vondracek, P., et al. (2016). Fast measurements of the electron temperature and parallel heat flux in ELMy H-mode on the COMPASS tokamak. *Nuclear Fusion*, 57(2):022010.
- [Alonso et al., 2006] Alonso, J., Zweben, S., Carvalho, P., de Pablos, J., de la Cal, E., Hidalgo, C., Klinger, T., van Milligen, B. P., Maqueda, R., Pedrosa, M., et al. (2006). Impact of different confinement regimes on the two-dimensional structure of edge turbulence. *Plasma physics and controlled fusion*, 48(12B):B465.
- [Anda et al., 2018] Anda, G., Dunai, D., Lampert, M., Krizsanóczy, T., Németh, J., Bató, S., Nam, Y., Hu, G., and Zoletnik, S. (2018). Development of a high current 60 keV neutral lithium beam injector for beam emission spectroscopy measurements on fusion experiments. *Review of Scientific Instruments*, 89(1):013503.
- [Angelino et al., 2008] Angelino, P., Garbet, X., Villard, L., Bottino, A., Jolliet, S., Ghendrih, P., Grandgirard, V., McMillan, B., Sarazin, Y., Dif-Pradalier, G., et al. (2008). The role of plasma elongation on the linear damping of zonal flows. *Physics of Plasmas*, 15(6):062306.
- [Appel et al., 2006] Appel, L., Huysmans, G., Lao, L., McCarthy, P., Muir, D., Solano, E., Storrs, J., Taylor, D., Zwingmann, W., et al. (2006). A

- unified approach to equilibrium reconstruction. In *33rd EPS Conference on Plasma Physics*.
- [Aragón et al., 2008] Aragón, J. L., Naumis, G. G., Bai, M., Torres, M., and Maini, P. K. (2008). Turbulent luminance in impassioned van Gogh paintings. *Journal of Mathematical Imaging and Vision*, 30(3):275–283.
- [Artaud et al., 2018] Artaud, J., Imbeaux, F., Garcia, J., Giruzzi, G., Aniel, T., Basiuk, V., Bécoulet, A., Bourdelle, C., Buravand, Y., Decker, J., et al. (2018). METIS: a fast integrated tokamak modelling tool for scenario design. *Nuclear Fusion*, 58(10):105001.
- [ASDEX Team, 1989] ASDEX Team (1989). The H-mode of ASDEX. *Nuclear Fusion*, 29(11):1959.
- [Berionni and Gürçan, 2011] Berionni, V. and Gürçan, Ö. D. (2011). Predator prey oscillations in a simple cascade model of drift wave turbulence. *Physics of Plasmas*, 18(11):112301.
- [Bickerton et al., 1971] Bickerton, R., Connor, J., and Taylor, J. (1971). Diffusion driven plasma currents and bootstrap tokamak. *Nature Physical Science*, 229(4):110.
- [Bilkova et al., 2018] Bilkova, P., Bohm, P., Aftanas, M., Sos, M., Havranek, A., Sestak, D., Weinzettl, V., Hron, M., Panek, R., et al. (2018). High resolution thomson scattering on the COMPASS tokamak—extending edge plasma view and increasing repetition rate. *Journal of Instrumentation*, 13(01):C01024.
- [Boedo et al., 2006] Boedo, J., Maqueda, R., Rudakov, D., McKee, G., Kugel, H., Maingi, R., Crocker, N., Moyer, R., Soukhanovskii, V., Menard, J., et al. (2006). Particle and energy transport in the SOL of DIII-D and NSTX. Technical report, Lawrence Livermore National Lab.(LLNL), Livermore, CA (United States).
- [Bohm et al., 2010] Bohm, P., Sestak, D., Bilkova, P., Aftanas, M., Weinzettl, V., Hron, M., Panek, R., Baillon, L., Dunstan, M., Naylor, G., et al. (2010). Laser system for high resolution thomson scattering diagnostics on the COMPASS tokamak. *Review of Scientific Instruments*, 81(10):10D511.
- [Bulanin et al., 2016] Bulanin, V., Askinazi, L., Belokurov, A., Kornev, V., Lebedev, V., Petrov, A., Tukachinsky, A., Vildjunas, M., Wagner, F., and Yashin, A. Y. (2016). GAM observation in the TUMAN-3M tokamak. *Plasma Physics and Controlled Fusion*, 58(4):045006.
- [Burrell et al., 1992] Burrell, K., Carlstrom, T., Doyle, E., Finkenthal, D., Gohil, P., Groebner, R., Hillis, D., Kim, J., Matsumoto, H., Moyer, R., et al. (1992). Physics of the L-mode to H-mode transition in tokamaks. *Plasma Physics and Controlled Fusion*, 34(13):1859.

- [Butterworth et al., 1930] Butterworth, S. et al. (1930). On the theory of filter amplifiers. *Wireless Engineer*, 7(6):536–541.
- [Cap, 2013] Cap, F. F. (2013). *Handbook on plasma instabilities*, volume 2. Academic Press.
- [Carreras et al., 1998] Carreras, B., Van Milligen, B., Pedrosa, M., Balbín, R., Hidalgo, C., Newman, D., Sánchez, E., Frances, M., García-Cortés, I., Bleuel, J., et al. (1998). Long-range time correlations in plasma edge turbulence. *Physical review letters*, 80(20):4438.
- [Chang et al., 2009] Chang, C., Ku, S., Diamond, P., Adams, M., Barreto, R., Chen, Y., Cummings, J., D’Azevedo, E., Dif-Pradalier, G., Ethier, S., et al. (2009). Whole-volume integrated gyrokinetic simulation of plasma turbulence in realistic diverted-tokamak geometry. In *Journal of Physics: Conference Series*, volume 180. IOP Publishing.
- [Chen, 1984] Chen, F. F. (1984). *Introduction to plasma physics and controlled fusion*, volume 1. Springer.
- [Clay Mathematics Institute, 2000] Clay Mathematics Institute (2000). Millennium Problems. <http://www.claymath.org/millennium-problems>, Cited: 2019-01-07.
- [Cohen, 1995] Cohen, L. (1995). *Time-frequency analysis*, volume 778. Prentice hall.
- [Connor et al., 1998] Connor, J., Hastie, R., Wilson, H., and Miller, R. (1998). Magnetohydrodynamic stability of tokamak edge plasmas. *Physics of Plasmas*, 5(7):2687–2700.
- [Conway et al., 2008] Conway, G., Tröster, C., Scott, B., Hallatschek, K., et al. (2008). Frequency scaling and localization of geodesic acoustic modes in ASDEX upgrade. *Plasma Physics and Controlled Fusion*, 50(5):055009.
- [Cowan, 1998] Cowan, G. (1998). *Statistical data analysis*. Oxford university press.
- [Cowley et al., 1991] Cowley, S. C., Kulsrud, R., and Sudan, R. (1991). Considerations of ion-temperature-gradient-driven turbulence. *Physics of Fluids B: Plasma Physics*, 3(10):2767–2782.
- [Cziegler et al., 2013] Cziegler, I., Diamond, P., Fedorczak, N., Manz, P., Tynan, G., Xu, M., Churchill, R., Hubbard, A., Lipschultz, B., Sierchio, J., et al. (2013). Fluctuating zonal flows in the I-mode regime in Alcator C-Mod. *Physics of Plasmas*, 20(5):055904.
- [Daniell, 1920] Daniell, P. (1920). Stieltjes-Volterra products. *Congr. Intern. des Math., Strasbourg*, pages 13–136.

- [Dejarnac et al., 2009] Dejarnac, R., Komm, M., Gunn, J., and Panek, R. (2009). Power flux in the ITER divertor tile gaps during ELMs. *Journal of Nuclear Materials*, 390:818–821.
- [Diamond et al., 2005] Diamond, P. H., Itoh, S., Itoh, K., and Hahm, T. (2005). Zonal flows in plasma—a review. *Plasma Physics and Controlled Fusion*, 47(5):R35.
- [Diamond et al., 2010] Diamond, P. H., Itoh, S.-I., and Itoh, K. (2010). *Modern Plasma Physics: Volume 1, Physical Kinetics of Turbulent Plasmas*. Cambridge University Press.
- [Dimitrova et al., 2017] Dimitrova, M., Popov, T. K., Adamek, J., Kovačič, J., Ivanova, P., Hasan, E., López-Bruna, D., Seidl, J., Vondráček, P., Dejarnac, R., et al. (2017). Plasma potential and electron temperature evaluated by ball-pen and langmuir probes in the COMPASS tokamak. *Plasma Physics and Controlled Fusion*, 59(12):125001.
- [Dominguez, 1991] Dominguez, R. (1991). The trapped ion mode in hot ion plasmas. *Nuclear Fusion*, 31(4):747.
- [Dunai et al., 2010] Dunai, D., Zoletnik, S., Sárközi, J., and Field, A. (2010). Avalanche photodiode based detector for beam emission spectroscopy. *Review of Scientific Instruments*, 81(10):103503.
- [Eich et al., 2017] Eich, T., Sieglin, B., Thornton, A., Faitsch, M., Kirk, A., Herrmann, A., Suttrop, W., et al. (2017). ELM divertor peak energy fluence scaling to ITER with data from JET, MAST and ASDEX upgrade. *Nuclear Materials and Energy*, 12:84–90.
- [Endler et al., 1995] Endler, M., Niedermeyer, H., Giannone, L., Kolzhauer, E., Rudyj, A., Theimer, G., and Tsois, N. (1995). Measurements and modelling of electrostatic fluctuations in the scrape-off layer of ASDEX. *Nuclear Fusion*, 35(11):1307.
- [Freidberg, 1987] Freidberg, J. P. (1987). *Ideal Magnetohydrodynamics*. Cambridge University Press.
- [Fried and Conte, 2015] Fried, B. D. and Conte, S. D. (2015). *The plasma dispersion function: the Hilbert transform of the Gaussian*. Academic Press.
- [Frieman and Chen, 1982] Frieman, E. and Chen, L. (1982). Nonlinear gyrokinetic equations for low-frequency electromagnetic waves in general plasma equilibria. *The Physics of Fluids*, 25(3):502–508.
- [Galeev et al., 1963] Galeev, A., Oraevskii, V., and Sagdeev, R. (1963). Universal stability of an inhomogeneous plasma in a magnetic field. *Zh. Eksperim. i Teor. Fiz.*, 44.
- [Galeev and Sagdeev, 1968] Galeev, A. and Sagdeev, R. (1968). Transport phenomena in a collisionless plasma in a toroidal magnetic system. *Sov. Phys. JETP*, 26(1):233–240.

- [Galeev and Sagdeev, 1971] Galeev, A. and Sagdeev, R. (1971). Limiting Plasma Pressure in a Tokamak. *ZhETF Pisma Redaktsiiu*, 13:162.
- [Gao, 2010] Gao, Z. (2010). Plasma shaping effects on the geodesic acoustic mode in the large orbit drift width limit. *Physics of Plasmas*, 17(9):092503.
- [Gao, 2013] Gao, Z. (2013). Collisional damping of the geodesic acoustic mode. *Physics of Plasmas*, 20(3):032501.
- [Garcia, 2012] Garcia, O. (2012). Stochastic modeling of intermittent scrape-off layer plasma fluctuations. *Physical review letters*, 108(26):265001.
- [Garcia et al., 2005] Garcia, O., Horacek, J., Pitts, R., Nielsen, A., Fundamenski, W., Graves, J., Naulin, V., and Rasmussen, J. J. (2005). Interchange turbulence in the TCV scrape-off layer. *Plasma physics and controlled fusion*, 48(1):L1.
- [Garcia et al., 2007a] Garcia, O. E., Horacek, J., Pitts, R., Nielsen, A. H., Fundamenski, W., Naulin, V., and Rasmussen, J. J. (2007a). Fluctuations and transport in the TCV scrape-off layer. *Nuclear fusion*, 47(7):667.
- [Garcia et al., 2007b] Garcia, O. E., Pitts, R., Horacek, J., Nielsen, A., Fundamenski, W., Graves, J., Naulin, V., and Rasmussen, J. J. (2007b). Turbulent transport in the TCV SOL. *Journal of Nuclear Materials*, 363:575–580.
- [Gibson and team, 1998] Gibson, A. and team, J. (1998). Deuterium–tritium plasmas in the Joint European Torus (JET): Behavior and implications. *Physics of Plasmas*, 5(5):1839–1847.
- [Golub and Van Loan, 1980] Golub, G. H. and Van Loan, C. F. (1980). An analysis of the total least squares problem. *SIAM journal on numerical analysis*, 17(6):883–893.
- [Grant et al., 1962] Grant, H., Stewart, R., and Moilliet, A. (1962). Turbulence spectra from a tidal channel. *Journal of Fluid Mechanics*, 12(2):241–268.
- [Green et al., 2003] Green, B. et al. (2003). ITER: burning plasma physics experiment. *Plasma physics and controlled fusion*, 45(5):687.
- [Grover et al., 2017] Grover, O., Adamek, J., Seidl, J., Devitre, A., Sos, M., Vondracek, P., Bilkova, P., and Hron, M. (2017). First simultaneous measurements of reynolds stress with ball-pen and langmuir probes. *Review of Scientific Instruments*, 88(6):063501.
- [Gunn et al., 2017] Gunn, J., Carpentier-Chouchana, S., Escourbiac, F., Hirai, T., Panayotis, S., Pitts, R., Corre, Y., Dejarnac, R., Firdaouss, M., Kočan, M., et al. (2017). Surface heat loads on the ITER divertor vertical targets. *Nuclear Fusion*, 57(4):046025.

- [Guszejnov et al., 2012] Guszejnov, D., Pokol, G., Pusztai, I., Refy, D., Zolotnik, S., Lampert, M., and Nam, Y. (2012). Three-dimensional modeling of beam emission spectroscopy measurements in fusion plasmas. *Review of Scientific Instruments*, 83(11):113501.
- [Hahm and Burrell, 1995] Hahm, T. and Burrell, K. (1995). Flow shear induced fluctuation suppression in finite aspect ratio shaped tokamak plasma. *Physics of Plasmas*, 2(5):1648–1651.
- [Havlicek et al., 2009] Havlicek, J., Horacek, J., Weinzettl, V., Hronova, O., Naydenkova, D., and Zajac, J. (2009). Magnetic diagnostics for start-up phase of COMPASS. *WDS'09 Proceedings of Contributed Papers: Part II—Physics of Plasmas and Ionized Media*, pages 148–152.
- [Hawryluk et al., 1998] Hawryluk, R., Batha, S., Blanchard, W., Beer, M., Bell, M., Bell, R., Berk, H., Bernabei, S., Bitter, M., Breizman, B., et al. (1998). Fusion plasma experiments on TFTR: A 20 year retrospective. *Physics of Plasmas*, 5(5):1577–1589.
- [Horacek et al., 2010] Horacek, J., Hidalgo, C., Seidl, J., Nielsen, A., Rasmussen, J., and Stoeckel, J. (2010). What we (don't) know about tokamak edge plasma transport from experiment and modeling. <https://slideplayer.com/slide/11875865/>. 2019-03-17.
- [Horton, 1999] Horton, W. (1999). Drift waves and transport. *Reviews of Modern Physics*, 71(3):735.
- [Imrisek et al., 2014] Imrisek, M., Weinzettl, V., Mlynar, J., Odstrcil, T., Odstrcil, M., Ficker, O., Pinzon, J., Ehrlacher, C., Panek, R., and Hron, M. (2014). Use of soft x-ray diagnostic on the COMPASS tokamak for investigations of sawteeth crash neighborhood and of plasma position using fast inversion methods. *Review of Scientific Instruments*, 85(11):11E433.
- [Jenko et al., 2000] Jenko, F., Dorland, W., Kotschenreuther, M., and Rogers, B. (2000). Electron temperature gradient driven turbulence. *Physics of Plasmas*, 7(5):1904–1910.
- [Jury et al., 1964] Jury, E. I., Jury, E. I., Jury, E. I., and Jury, E. I. (1964). *Theory and Application of the z-Transform Method*, volume 3. Wiley New York.
- [Katz et al., 2008] Katz, N., Egedal, J., Fox, W., Le, A., and Porkolab, M. (2008). Experiments on the propagation of plasma filaments. *Physical review letters*, 101(1):015003.
- [Kolmogorov, 1941] Kolmogorov, A. N. (1941). Equations of turbulent motion in an incompressible fluid. In *Dokl. Akad. Nauk SSSR*, volume 30, pages 299–303.
- [Kraichnan, 1967] Kraichnan, R. H. (1967). Inertial ranges in two-dimensional turbulence. *The Physics of Fluids*, 10(7):1417–1423.

- [Ku et al., 2009] Ku, S., Chang, C.-S., and Diamond, P. (2009). Full-f gyrokinetic particle simulation of centrally heated global ITG turbulence from magnetic axis to edge pedestal top in a realistic tokamak geometry. *Nuclear Fusion*, 49(11):115021.
- [Lampert et al., 2015] Lampert, M., Anda, G., Czopf, A., Erdei, G., Guszejnov, D., Kovácsik, Á., Pokol, G., Réfy, D., Nam, Y., and Zoletnik, S. (2015). Combined hydrogen and lithium beam emission spectroscopy observation system for Korea Superconducting Tokamak Advanced Research. *Review of Scientific Instruments*, 86(7):073501.
- [Lawrence Berkeley National Laboratory, 2017] Lawrence Berkeley National Laboratory (2017). NERSC Sims Show How Recycled Atoms Boost Plasma Turbulence. <https://cs.lbl.gov/news-media/news/2017/simulations-show-how-recycled-atoms-boost-plasma-turbulence/>. 2019-07-06.
- [Lawson, 1957] Lawson, J. D. (1957). Some criteria for a power producing thermonuclear reactor. *Proceedings of the Physical Society. Section B*, 70(1):6.
- [Legendre, 1805] Legendre, A. M. (1805). *Nouvelles méthodes pour la détermination des orbites des comètes*. F. Didot.
- [Lortz, 1975] Lortz, D. (1975). The general “peeling” instability. *Nuclear Fusion*, 15(1):49.
- [Malkov and Diamond, 2009] Malkov, M. and Diamond, P. (2009). Weak hysteresis in a simplified model of the LH transition. *Physics of Plasmas*, 16(1):012504.
- [Manfredi et al., 2001] Manfredi, G., Roach, C., and Dendy, R. (2001). Zonal flow and streamer generation in drift turbulence. *Plasma physics and controlled fusion*, 43(6):825.
- [Markovsky and Huffel, 2004] Markovsky, I. and Huffel, S. V. (2004). A Matlab toolbox for weighted total least squares approximation. Technical Report 04-220, Dept. EE, K.U. Leuven.
- [Mazzucato et al., 1996] Mazzucato, E., Batha, S., Beer, M., Bell, M., Bell, R., Budny, R., Bush, C., Hahm, T., Hammett, G., Levinton, F., et al. (1996). Turbulent fluctuations in TFTR configurations with reversed magnetic shear. *Physical review letters*, 77(15):3145.
- [Mercier, 1962] Mercier, C. (1962). Stability criterion of a hydromagnetic toroidal system with scalar pressure. *Nuclear Fusion*, pages 801–808.
- [Mitosinkova et al., 2016] Mitosinkova, K., Melnik, A., Tomes, M., Stockel, J., Janky, F., Komm, M., Imrisek, M., Hacek, P., Varju, J., and Weinzettl, V. (2016). First results from the Neutral Particle Analyzer on the COMPASS

- [Press et al., 2007] Press, W. H., Teukolsky, S. A., Vetterling, W. T., and Flannery, B. P. (2007). *Numerical Recipes, The Art of Scientific Computing, 3rd edition*. Cambridge University Press.
- [Pueschel et al., 2012] Pueschel, M., Jenko, F., Schneller, M., Hauff, T., Günter, S., and Tardini, G. (2012). Anomalous diffusion of energetic particles: connecting experiment and simulations. *Nuclear Fusion*, 52(10):103018.
- [Pusztai et al., 2009] Pusztai, I., Pokol, G., Dunai, D., Réfy, D., Pór, G., Anda, G., Zoletnik, S., and Schweinzer, J. (2009). Deconvolution-based correction of alkali beam emission spectroscopy density profile measurements. *Review of Scientific Instruments*, 80(8):083502.
- [Réfy et al., 2018] Réfy, D., Brix, M., Gomes, R., Tál, B., Zoletnik, S., Dunai, D., Kocsis, G., Kálvin, S., Szabolics, T., and Contributors, J. (2018). Sub-millisecond electron density profile measurement at the JET tokamak with the fast lithium beam emission spectroscopy system. *Review of Scientific Instruments*, 89(4):043509.
- [Rudakov and Sagdeev, 1961] Rudakov, L. I. and Sagdeev, R. Z. (1961). On the instability of a nonuniform rarefied plasma in a strong magnetic field. In *Soviet Physics Doklady*, volume 6, page 415.
- [Rutgers, 1998] Rutgers, M. A. (1998). Forced 2D turbulence: Experimental evidence of simultaneous inverse energy and forward enstrophy cascades. *Physical review letters*, 81(11):2244.
- [Ryter et al., 1998] Ryter, F., Suttrop, W., Brüsehauer, B., Kaufmann, M., Mertens, V., Murmann, H., Peeters, A., Stober, J., Schweinzer, J., Zohm, H., et al. (1998). H-mode power threshold and transition in ASDEX Upgrade. *Plasma physics and controlled fusion*, 40(5):725.
- [Sakharov and Tamm, 1958] Sakharov, A. D. and Tamm, I. Y. (1958). Theory of the magnetic thermonuclear reactor. *Plasma Physics and the CTF Problem*, 1.
- [Schmitz et al., 2014] Schmitz, L., Zeng, L., Rhodes, T. L., Hillesheim, J. C., Peebles, W. A., Groebner, R. J., Burrell, K. H., McKee, G. R., Yan, Z., Tynan, G., et al. (2014). The role of zonal flows and predator–prey oscillations in triggering the formation of edge and core transport barriers. *Nuclear Fusion*, 54(7):073012.
- [Schweinzer et al., 1992] Schweinzer, J., Wolfrum, E., Aumayr, F., Pockl, M., Winter, H., Schorn, R., Hintz, E., and Unterreiter, A. (1992). Reconstruction of plasma edge density profiles from Li I (2s-2p) emission profiles. *Plasma physics and controlled fusion*, 34(7):1173.
- [SciPy, 2019] SciPy (2019). SciPy documentation. <https://docs.scipy.org/doc/scipy/reference/index.html>, Cited: 2019-12-07.

- [Simon et al., 2016] Simon, P., Conway, G., Stroth, U., Biancalani, A., Palermo, F., et al. (2016). Comparison of experiment and models of geodesic acoustic mode frequency and amplitude geometric scaling in ASDEX upgrade. *Plasma Physics and Controlled Fusion*, 58(4):045029.
- [Sivia and Skilling, 2006] Sivia, D. and Skilling, J. (2006). *Data analysis: a Bayesian tutorial*. OUP Oxford.
- [Smith et al., 1997] Smith, S. W. et al. (1997). *The scientist and engineer's guide to digital signal processing*. California Technical Pub. San Diego.
- [Snipes et al., 1998] Snipes, J., Granetz, R., Greenwald, M., Hubbard, A., Hutchinson, I., Irby, J., Kesner, J., Migliuolo, S., Pedersen, T. S., Ramos, J., et al. (1998). ELMs and fast edge fluctuations in Alcator C-Mod. *Plasma physics and controlled fusion*, 40(5):765.
- [Snyder et al., 2004] Snyder, P., Wilson, H., Ferron, J., Lao, L., Leonard, A., Mossessian, D., Murakami, M., Osborne, T., Turnbull, A., and Xu, X. (2004). Elms and constraints on the h-mode pedestal: peeling–ballooning stability calculation and comparison with experiment. *Nuclear fusion*, 44(2):320.
- [Snyder et al., 2002] Snyder, P., Wilson, H., Ferron, J., Lao, L., Leonard, A., Osborne, T., Turnbull, A., Mossessian, D., Murakami, M., and Xu, X. (2002). Edge localized modes and the pedestal: A model based on coupled peeling–ballooning modes. *Physics of Plasmas*, 9(5):2037–2043.
- [Snyder et al., 2015] Snyder, P. B., Solomon, W. M., Burrell, K. H., Garofalo, A. M., Grierson, B. A., Groebner, R. J., Leonard, A. W., Nazikian, R., Osborne, T. H., Belli, E. A., et al. (2015). Super H-mode: theoretical prediction and initial observations of a new high performance regime for tokamak operation. *Nuclear Fusion*, 55(8):083026.
- [Snyman and Wilke, 2018] Snyman, J. A. and Wilke, D. N. (2018). *Practical Mathematical Optimization: Basic Optimization Theory and Gradient-based Algorithms*, volume 133. Springer.
- [Stefanikova et al., 2016] Stefanikova, E., Peterka, M., Bohm, P., Bilkova, P., Aftanas, M., Sos, M., Urban, J., Hron, M., and Panek, R. (2016). Fitting of the Thomson scattering density and temperature profiles on the COMPASS tokamak. *Review of Scientific Instruments*, 87(11):11E536.
- [Taylor and Williams, 1995] Taylor, F. and Williams, A. (1995). Electronic filter design handbook. *McGraw-Hill, USA*.
- [Terry, 2000] Terry, P. (2000). Suppression of turbulence and transport by sheared flow. *Reviews of Modern Physics*, 72(1):109.
- [Thomas, 1995] Thomas, D. (1995). Development of lithium beam emission spectroscopy as an edge fluctuation diagnostic for DIII-D. *Review of scientific instruments*, 66(1):806–811.

- [Ulrich, 2006] Ulrich, T. (2006). Envelope calculation from the Hilbert transform. *Los Alamos Nat. Lab., Los Alamos, NM, USA, Tech. Rep.*
- [Vondráček, 2012] Vondráček, P. (2012). Studium okrajového plazmatu tokamaku COMPASS pomocí dvojice reciprokových sond. Master's thesis, České vysoké učení technické v Praze.
- [Wade, 2009] Wade, M. R. (2009). Physics and engineering issues associated with edge localized mode control in ITER. *Fusion Engineering and Design*, 84(2-6):178–185.
- [Wagner et al., 1982] Wagner, F., Becker, G., Behringer, K., Campbell, D., Eberhagen, A., Engelhardt, W., Fussmann, G., Gehre, O., Gernhardt, J., Gierke, G. v., et al. (1982). Regime of improved confinement and high beta in neutral-beam-heated divertor discharges of the ASDEX tokamak. *Physical Review Letters*, 49(19):1408.
- [Weinberg, 1957] Weinberg, L. (1957). Explicit formulas for Tschebyscheff and Butterworth ladder networks. *Journal of Applied Physics*, 28(10):1155–1160.
- [Weinzettl et al., 2010] Weinzettl, V., Naydenkova, D., Sestak, D., Vlcek, J., Mlynar, J., Melich, R., Jares, D., Malot, J., Sarychev, D., and Igochine, V. (2010). Design of multi-range tomographic system for transport studies in tokamak plasmas. *Nuclear Instruments and Methods in Physics Research Section A: Accelerators, Spectrometers, Detectors and Associated Equipment*, 623(2):806–808.
- [Weinzettl et al., 2011] Weinzettl, V., Panek, R., Hron, M., Stockel, J., Zacek, F., Havlicek, J., Bilkova, P., Naydenkova, D., Hacek, P., Zajac, J., et al. (2011). Overview of the COMPASS diagnostics. *Fusion Engineering and Design*, 86(6-8):1227–1231.
- [Wesson and Campbell, 2011] Wesson, J. and Campbell, D. J. (2011). *Tokamaks*, volume 149. Oxford University Press.
- [Whyte et al., 2010] Whyte, D., Hubbard, A., Hughes, J., Lipschultz, B., Rice, J., Marmar, E., Greenwald, M., Cziegler, I., Dominguez, A., Golfinopoulos, T., et al. (2010). I-mode: an H-mode energy confinement regime with L-mode particle transport in Alcator C-Mod. *Nuclear Fusion*, 50(10):105005.
- [Willensdorfer et al., 2014] Willensdorfer, M., Birkenmeier, G., Fischer, R., Laggner, F., Wolfrum, E., Veres, G., Aumayr, F., Carralero, D., Guimarães, L., Kurzan, B., et al. (2014). Characterization of the Li-BES at ASDEX Upgrade. *Plasma Physics and Controlled Fusion*, 56(2):025008.
- [Winsor et al., 1968] Winsor, N., Johnson, J. L., and Dawson, J. M. (1968). Geodesic acoustic waves in hydromagnetic systems. *The Physics of Fluids*, 11(11):2448–2450.

- [Wolf, 2002] Wolf, R. (2002). Internal transport barriers in tokamak plasmas. *Plasma Physics and Controlled Fusion*, 45(1):R1.
- [Wolfrum et al., 1993] Wolfrum, E., Aumayr, F., Wutte, D., Winter, H., Hintz, E., Rusbüldt, D., and Schorn, R. (1993). Fast lithium-beam spectroscopy of tokamak edge plasmas. *Review of scientific instruments*, 64(8):2285–2292.
- [Zohm, 1996] Zohm, H. (1996). Edge localized modes (ELMs). *Plasma Physics and Controlled Fusion*, 38(2):105.
- [Zoletnik et al., 1999] Zoletnik, S., Anton, M., Endler, M., Fiedler, S., Hirsch, M., McCormick, K., Schweinzer, J., and team, W.-A. (1999). Density fluctuation phenomena in the scrape-off layer and edge plasma of the Wendelstein 7-AS stellarator. *Physics of Plasmas*, 6(11):4239–4247.
- [Zoletnik et al., 2018] Zoletnik, S., Hu, G., Tál, B., Dunai, D., Anda, G., Asztalos, O., Pokol, G., Kálvin, S., Németh, J., and Krizsanóczy, T. (2018). Ultrafast two-dimensional lithium beam emission spectroscopy diagnostic on the EAST tokamak. *Review of Scientific Instruments*, 89(6):063503.
- [Zoletnik et al., 2005] Zoletnik, S., Petravich, G., Bencze, A., Berta, M., Fiedler, S., McCormick, K., and Schweinzer, J. (2005). Two-dimensional density and density fluctuation diagnostic for the edge plasma in fusion devices. *Review of scientific instruments*, 76(7):073504.
- [Zweben and Gould, 1985] Zweben, S. and Gould, R. (1985). Structure of edge-plasma turbulence in the Caltech tokamak. *Nuclear fusion*, 25(2):171.
- [Zweben et al., 2003] Zweben, S., Maqueda, R., Stotler, D., Keese, A., Boedo, J., Bush, C., Kaye, S., LeBlanc, B., Lowrance, J., Mastrocola, V., et al. (2003). High-speed imaging of edge turbulence in NSTX. *Nuclear Fusion*, 44(1):134.

Appendix C

List of author's publications

C.1 Publications related to the thesis

- [1] **Krbec, J.**, and Háček, P., Berta, M., Seidl, J., Hron, M., Pánek, R. (2018), Fast density reconstruction of Li-BES signal on the COMPASS tokamak, *Review of Scientific Instruments*, 89(11):113504
- [2] Seidl, J., **Krbec, J.**, Hron, M., Adamek, J., Hidalgo, C., Markovic, T., Melnikov, A., Stockel, J., Weinzettl, V., Aftanas, M., et al. (2017), Electromagnetic characteristics of geodesic acoustic mode in the COMPASS tokamak, *Nuclear Fusion*, 57(12):126048
- [3] de Souza, F.C., Elfimov, A., Galvão, R., **Krbec, J.**, Seidl, J., Stöckel, J., Hron, M., Havlicek, J., Mitosinkova, K. (2017), Geodesic mode instability driven by electron and ion fluxes during neutral beam injection in tokamaks, *Physics Letters A*, 381(36):3066-3070
- [4] Anda, G., Bencze, A., Berta, M., Dunai, D., Hacek, P., **Krbec, J.**, Réfy, D., Krizsanóczy, T., Bató, S., Ilkei, T., et al. (2016), Lithium beam diagnostic system on the COMPASS tokamak, *Fusion Engineering and Design*, 108:1-6
- [5] Komm, M., Bílková, P., Aftanas, M., Berta, M., Böhm, P., Bogár, O., Frassinetti, L., Grover, O., Háček, P., Havlicek, J., Hron, M., Imříšek, M., **Krbec, J.**, et al. (2017), Contribution to the multi-machine pedestal scaling from the COMPASS tokamak, *Nuclear Fusion*, 57(5):056041
- [6] Berta, M., Anda, G., Bencze, A., Dunai, D., Háček, P., Hron, M., Kovácsik, A., **Krbec, J.**, Pánek, R., Réfy, D., et al. (2015), Li-BES detection system for plasma turbulence measurements on the COMPASS tokamak, *Fusion Engineering and Design*, 96:795-798
- [7] Weinzettl, V., Adamek, J., Berta, M., Bilkova, P., Bogar, O., Bohm, P., Cavalier, J., Dejarnac, R., Dimitrova, M., Ficker, O., Fridrich, D., Grover, O., Hacek, P., Havlicek, J., Havranek, A., Horacek, J., Hron, M., Imrisek, M., Komm, M., Kovarik, K., **Krbec, J.**, et al. (2017), Progress

in diagnostics of the COMPASS tokamak, *Journal of Instrumentation*, 12(12):C12015

- [8] Bencze, A., Berta, M., Buzas, A., Hacek, P., **Krbec, J.**, Szutyanyi, M., and COMPASS Team, et al. (2019), Characterization of edge and scrape-off layer fluctuations using the fast Li-BES system on COMPASS, *Plasma Physics and Controlled Fusion*, 61(8):085014
- [9] Grover, O., Seidl, J., Réfy, D., Adamek, J., Vondracek, P., Tomes, M., Junek, P., Hacek, P., **Krbec, J.**, Weinzettl, V., et al. (2018), Limit cycle oscillations measurements with Langmuir and ball-pen probes on COMPASS, *Nuclear Fusion*, 58.11: 112010

C.2 Other publications

- [10] Komm, M., Khodunov, I., Cavalier, J., Vondracek, P., Henderson, S.S., Seidl, J., Horacek, J., Naydenkova, D., Adamek, J., Bilkova, P., Bohm, P., Devitre, A.R., Dimitrova, M., Elmore, S., Faitsch, M., Hacek, P., Havlicek, J., Havranek, A., Imrisek, M., **Krbec, J.**, et al. (2019), Divertor impurity seeding experiments at the COMPASS tokamak, *Nuclear Fusion*, 59.10: 106035.
- [11] Ficker, O., Macusova, E., Mlynář, J., Bren, D., Casolari, A., Cerovsky, J., Farnik, M., Grover, O., Havlicek, J., Havranek, A., Hron, M., Imrisek, M., Jerab, M., **Krbec, J.**, et al. (2019), Runaway electron beam stability and decay in COMPASS, *Nuclear Fusion*, 59.9: 096036.
- [12] Weinzettl, V., Adamek, J., Bilkova, P., Havlicek, J., Panek, R., Hron, M., Bogar, O., Bohm, P., Casolari, A., Cavalier, J., Dejarnac, R., Dimitrova, M., Duran, I., Entler, S., Ficker, O., Hacek, P., Horacek, J., Imrisek, M., Jaulmes, F., Kovarik, K., **Krbec, J.**, et al. (2019), Constraints on conceptual design of diagnostics for the high magnetic field COMPASS-U tokamak with hot walls, *Fusion Engineering and Design*, 146: 1703-1707.
- [13] Panek, R., Adámek, J., Aftanas, M., Bílková, P., Böhm, P., Brochard, F., Cahyna, P., Cavalier, J., Dejarnac, R., Dimitrova, M., Grover, O., Harrison, J., Háček, P., Havlíček, J., Havránek, A., Horáček, J., Hron, M., Imříšek, M., Janky, F., Kirk, A., Komm, M., Kovařík, K., **Krbec, J.**, et al. (2015), Status of the COMPASS tokamak and characterization of the first H-mode, *Plasma Physics and Controlled Fusion* 58(1):014015
- [14] Podolnik, A., Komm, M., Adamek, J., Hacek, P., **Krbec, J.**, Dejarnac, R., Gunn, J., Panek, R. (2018), 3D particle-in-cell modeling of Langmuir probe effective collecting area in magnetized plasma, *Plasma Physics and Controlled Fusion*, 60.8: 085008.
- [15] Meyer, H., et al. (2017), Overview of progress in European medium sized tokamaks towards an integrated plasma-edge/wall solution, *Nuclear Fusion* 57(10):102014

- [16] Panek, R., Markovic, T., Cahyna, P., Dejarnac, R., Havlicek, J., Horacek, J., Hron, M., Imrisek, M., Junek, P., Komm, M., Sestak, D., Urban, J., Varju, J., Weinzettl, V., Adamek, J., Bilkova, P., Bohm, P., Dimitrova, M., Hacek, P., Kovarik, K., **Krbec, J.**, et al. (2017), Conceptual design of the COMPASS upgrade tokamak, *Fusion Engineering and Design* 123:11-16
- [17] Svoboda, V., Kocman, J., Grover, O., **Krbec, J.**, Stöckel, J. (2017), Remote operation of the vertical plasma stabilization@ the GOLEM tokamak for the plasma physics education, *Fusion Engineering and Design* 96:974-979
- [18] Hacek, P., Berta, M., Anda, G., Aradi, M., Bencze, A., Dunai, D., **Krbec, J.**, Panek, R., Refy, D., Stockel, J., et al. (2018), Development of an ion beam detector for the atomic beam probe diagnostic, *Review of Scientific Instruments* 89(11):113506

■ C.3 Conference proceedings

- [19] Yanovskiy, V.V., Pustovitov, V.D., Matveeva, E., Havlicek, J., Havranek, A., Hromadka, J., Hron, M., Isernia, N., Komm, M., Kovanda, O., Kovarik, K., **Krbec, J.**, et al. (2019), Poloidal currents in COMPASS vacuum vessel during symmetrical disruptions: diamagnetic measurements and comparison with analytics, *46th EPS Conference on Plasma Physics* Milan, Italy, ECA Vol. 43C, P4.1056
- [20] Hacek, P., Berta, M., Szutyanyi, M., Somers, R., Bencze, A., **Krbec, J.**, Hron, M., Panek, R., Weinzettl, V. (2019), Automatic ELM detection and study of statistical ELM properties by Li-BES on COMPASS, *46th EPS Conference on Plasma Physics* Milan, Italy, ECA Vol. 43C, P1.1020
- [21] Kripner, L., Tomes, M., Urban, J., Grover, O., Ficker, O., Macusova, E., Peterka, M., **Krbec, J.**, Jaulmes, F., Cerovsky, J., Fridrich, D. (2019), Towards the integrated analysis of tokamak plasma equilibria: Pleque, *46th EPS Conference on Plasma Physics* Milan, Italy, ECA Vol. 43C, P4.1033
- [22] Istokskaia, V., Shkut, M., Cerovsky, J., Farnik, M., Grover, O., Hudec, L., Macha, P., **Krbec, J.**, Svoboda, V., Stockel, J., et al. (2018), Tokamak GOLEM for fusion education - chapter 9, *45th EPS Conference on Plasma Physics* Prague, Czech republic, ECA Vol. 42A, P1.1034
- [23] Buzás, A., Bencze, A., **Krbec, J.**, Háček, P., Berta, M., Seidl, J., Pánek, R. (2018), Statistical analysis of SOL fluctuations on COMPASS tokamak as measured by the Li-BES diagnostic, *45th EPS Conference on Plasma Physics* Prague, Czech republic, ECA Vol. 42A, P2.1091
- [24] Réfy, D., Hacek, P., Zoletnik, S., Dunai, D., Anda, G., Lampert, M., Aradi, M., Bencze, A., Berta, M., **Krbec, J.**, et al. (2018), Atomic Beam

- Probe diagnostic for plasma edge current measurements at COMPASS, *45th EPS Conference on Plasma Physics* Prague, Czech republic, ECA Vol. 42A, P4.1019
- [25] Komm, M., Cavalier, J., Seidl, J., Adamek, J., Bilkova, P., Bohm, P., Devitre, A., Dimitrova, M., Elmore, S., Faitsch, M., Hacek, P., Havlicek, J., Imrisek, M., **Krbec, J.** et al. (2017), First detachment studies on COMPASS tokamak using nitrogen seeding, *44th EPS Conference on Plasma Physics* Belfast, Northern Ireland (UK), ECA Vol. 41F, P1.118
- [26] Dimitrova, M., Popov, T., Dejarnac, R., Komm, M., Cavalier, J., Seidl, J., **Krbec, J.**, Stockel, J., Weinzettl, V., Hacek, P., Panek, R. (2017), EEDF in the COMPASS open divertor during a detachment experiment, *44th EPS Conference on Plasma Physics* Belfast, Northern Ireland (UK), ECA Vol. 41F, P2.105
- [27] Réfy, D., Zoletnik, S., Grover, O., Seidl, J., Hron, M., Dunai, D., Anda, G., Bencze, A., Hacek, P., **Krbec, J.**, Weinzettl, V. (2017), Characterization of the electron density profile dynamic and flow velocity modulation during oscillations close to the L-H threshold at COMPASS, *44th EPS Conference on Plasma Physics* Belfast, Northern Ireland (UK), ECA Vol. 41F, P4.178
- [28] Elfimov, A., de Souza, F., Galvão, R., **Krbec, J.**, Seidl, J., Stöckel, J., Hron, M., Havlicek, J., Mitošinkova, K. (2016), Geodesic mode instability driven by electron and ion fluxes in tokamaks, *43th EPS Conference on Plasma Physics* Leuven, Belgium, ECA Vol. 40A, P2.038
- [29] Dimitrova, M., Ficker, O., Grover, O., Kocman, J., **Krbec, J.**, Loffelmann, V., Matena, L., Stockel, J., Svoboda V., Vondrasek, G. (2015), Tokamak GOLEM for fusion education - chapter 6, *42th EPS Conference on Plasma Physics* Lisbon, Portugal, ECA Vol. 39E, P2.164
- [30] Ficker, O., Grover, O., Kocman, J., **Krbec, J.**, Loffelmann, V., Markovic, T., Matusu, M., Stockel, J., Svoboda, V., Veverka, J., Vondrasek, G. (2014), Tokamak GOLEM for fusion education - chapter 5, *41th EPS Conference on Plasma Physics* Berlin, Germany, ECA Vol. 38F, P4.141
- [31] Hron, M., Havlicek, J., Mikulin, O., Janky, F., Stockel, J., Batista, A., Imrisek, M., Weinzettl, V., **Krbec, J.**, Panek, R. and the COMPASS team (2014), ELM control using vertical kicks on the COMPASS tokamak, *41th EPS Conference on Plasma Physics* Berlin, Germany, ECA Vol. 38F, P5.027

■ C.4 Conference posters

- [32] **Krbec, J.**, Berta, M., Háček, P., Hron, M., Seidl, J. (2015), Comparison of beam light and electron density fluctuations using Li-BES, *FuseNet PhD Event 2015* Prague, Czech republic
- [33] Ficker, O., Grover, O., Kocman, J., **Krbec, J.**, Loffelmann, V., Markovic, T., Matusu, M., Stockel, J., Svoboda, V., Veverka, J., Vondrasek, G. (2014), Tokamak GOLEM for fusion education - chapter 5, *41th EPS Conference on Plasma Physics* Berlin, Germany, ECA Vol. 38F, P4.141